8-2021

Modified electrode surfaces with hydrogen evolution reaction catalysts derived from electropolymerized complexes with redox active ligands.

Amanda Mae Arts
University of Louisville

MODIFIED ELECTRODE SURFACES WITH HYDROGEN EVOLUTION REACTION CATALYSTS DERIVED FROM ELECTROPOLYMERIZED COMPLEXES WITH REDOX ACTIVE LIGANDS

By:

Amanda Mae Arts

B.S., University of Louisville, 2020

A Thesis

Submitted to the Faculty of the

University of Louisville

J. B. Speed School of Engineering

As Partial Fulfillment of the Requirements

For the Professional Degree

MASTER OF ENGINEERING

Department of Chemical Engineering

August 9, 2021

APPROVAL PAGE

MODIFIED ELECTRODE SURFACES WITH HYDROGEN EVOLUTION REACTION CATALYSTS DERIVED FROM ELECTROPOLYMERIZED COMPLEXES WITH REDOX ACTIVE LIGANDS

Submitted By: Amanda Mae Arts

Amanda Mae Arts

A Thesis Approved On

8/9/2021

(Date)

By the Following Reading and Examination Committee:

Gautam Gupta

Gautam Gupta, Ph.D., Thesis Director

Mahyar Ghorbanian, Ph.D.

Robert M. Buchanan Digitally signed by Robert M. Buchanan Date: 2021.08.09 20:46:11 -04'00'

Robert Buchanan, Ph.D.

Craig Grapperhaus Digitally signed by Craig Grapperhaus DN: cn=Craig Grapperhaus, o=University of Louisville, ou=Department of Chemistry, email=cagrap01@louisville.edu, c=US Date: 2021.08.10 08:49:59 -04'00' Adobe Acrobat version: 2021.005.20060

Craig Grapperhaus, Ph.D.

ACKNOWLEDGEMENTS

I would like to thank the members of my thesis committee, Dr. Mahyar Ghorbanian, Dr. Robert Buchanan, Dr. Craig Grapperhaus, and Dr. Gautam Gupta for supporting me through my academic career. I would especially like to thank Dr. Gautam Gupta for taking the time to be my thesis director and for teaching me a great deal, not only about electrochemistry, but about life as well. I truly appreciate the countless hours that we have spent in the lab or virtually discussing this project. Without your expertise, guidance, trust, dedication, and flexibility, this project would have never been created. Thank you for taking me on as a student and for putting me on the path to success. Additionally, I would like to thank the members of the Chemistry Department, specifically Mohan Paudel for his collaboration in synthesizing sample complexes and conducting experiments for this endeavor. I would also like to thank the incredible Gupta Research Lab as a whole; it has been a pleasure working with you all, and there is no one I would rather have in my corner than the amazing group of past and present members we boast. Finally, I would also like to thank my mom for her undying love, support, and encouragement throughout my undergraduate, graduate, and professional careers. This research was supported by the National Science Foundation Grant number 057588857.

ABSTRACT

The demand for energy is growing exponentially, and to keep up with these demands new technologies for renewable energy have received increased attention. Hydrogen is one of the most promising energy sources for the future and plays a vital role in water electrolysis and fuel cells, as the hydrogen evolution reaction (HER) is the main step in the water splitting process. To increase the reaction rate and improve efficiency for the water electrolysis, catalysts are used to minimize the overpotential.

Most of the current electrocatalysts for HER are heterogeneous in nature and are dominated by platinum and other precious metals due to their high current density and small Tafel slope; however, they are extremely costly and have rare-earth abundance. For this reason, cost-effective catalysts must be developed. Previously, many have seen the best success by employing the use of earth-abundant transition metal chalcogenides to use as homogeneous molecular electrocatalysts, the most promising of which is molybdenum sulfide. These electrocatalysts do display low overpotentials and high HER activity; however, they contain a low number of active sites. Many have worked to address these issues.

The biggest challenge with heterogeneous catalysts as a whole is the inability to do detailed mechanism investigations. Homogeneous catalysts, alternatively, have attractive properties of activity and selectivity. The main issues with homogeneous catalysts are recycling and separation from product. To combine the benefits of both heterogeneous and homogeneous catalysts, immobilization of characterized catalysts onto the solid electrode surface to allow them to work under heterogeneous conditions is proposed. This heterogenization of a homogeneous catalyst onto the electrode surface is an ideal way to study a catalyst. The goal of this work was to develop and engineer new carbon materials, while heterogenizing new and existing

homogeneous thiomesicarbazone (TSC) compounds, supplied by the Grapperhaus/Buchanan Research Group, as electrocatalysis of HER. Thermodynamics, kinetics, and transport were the driving forces in the study.

A series of metal complexes based on inexpensive bis-thiomesicarbazone ligands including bis-thiophenepyrrolebutylamine(BTP4A), diacetyl-bis(N-4-methyl-3-thiosemicarbazide) (ATSM), and ATSM with pyrrole attached (ATSMpy) were synthesized and characterized by NMR, IR, cyclic voltammetry, and square wave voltammetry. Modified electrodes were prepared with films deposited on glassy carbon, standard pencils, and carbon paste electrodes, and evaluated as potential HER catalysts using cyclic voltammetry, linear sweep voltammetry, and electrochemical impedance spectroscopy.

HER studies in 0.5 M aqueous H_2SO_4 (10 mA cm^{-2}) revealed that modified electrode surfaces of glassy carbon, carbon paste, and standard pencils with TSCs gave promising electrochemical activity to be used for HER catalysis application. Pencil electrodes have shown to report improved activity due to increased surface interactions. Specifically, the blank pencil with C15 (Ni-ATSM) reported the lowest overpotential, Tafel slope, and charge transfer resistance of any sample, with overpotential values of 0.214-0.328 V. This sample combination will be further studied to prove its viability to be used as electrocatalysts with modified electrodes for HER.

TABLE OF CONTENTS

NOMENCLATURE

a= Activity of Hydrogen Ion (mM)

a= Tafel Equation Constant (V)

b= Tafel Equation Constant (V)

d= Resolution (length)

e= Charge (C)

f= Frequency (Hz)

h= Planck's Constant (erg sec)

i= Measured Current of Each Pulse (A)

iR= Ohmic Potential Drop (V)

j= Current Density (A/m^2)

j_0= Exchange Current Density (A/m^2)

k= Boltzmann Constant (J/K)

m= Index of Refraction of Medium Between Point Source and Lens, Relative to Free Space (dimensionless)

n= Number of Electrons Transferred (dimensionless)

p= Pressure at Which Electrolysis Takes Place (atm)

r= Distance of Separation (m)

t= Time (s)

t_p= Pulse Width Time (s)

v= Scan Rate (V/s)

v_s= Scan Rate of the Potential Sweep (V/s)

v_0= Frequency of the Laser (cm^{-1})

A= Effective Area of Electrode (cm^2)

B_o= Strength of Magnetic Field (Tesla)

C= Bulk Concentration of Reactant (mol/L)

C_{bulk}= Concentration of Bulk (mol/L)

C= Capacity of the Capacitor (F)

D= Reactant Diffusion Coefficient (cm^2/s)

D_A= Diffusion Coefficient (cm^2/s)

D_O= Diffusion Coefficient of Oxidant (cm^2/s)

D_R= Diffusion Coefficient of Reductant (cm^2/s)

E_{HER}= Equilibrium Potential Needed for Hydrogen Evolution Reaction (V)

E^0= Standard Potential (V)

E_i= Total Applied Potential (V)

E_p= Peak Potential (V)

$E_{p,a}$= Anodic Peak Potential (V)

$E_{p,c}$= Cathodic Peak Potential (V)

$E_{p/2}$= Half Peak Potential (V)

E^C= Charging Potential or Voltage (V)

ΔE= Difference in Energies of the Two Nuclear Spin Orientations (J)

ΔE_p= Step Width or Pulse Height (V)

ΔE_s= Amplitude or Staircase Height (V)

E= Electrode Potential (V)

E_0= Amplitude of the Signal (m)

E_l= Lower Limit Potential (V)

$E_{1/2}$= Half-Wave Potential (V)

F= Faraday Constant (C/mol)

I_p= Peak Current (A)

$I_{p,a}$= Anodic Peak Current (A)

$I_{p,c}$= Cathodic Peak Current (A)

I= Current (A)

I_0= Output Current (A)

I^0= Starting Current (A)

N_{upper}= Number of Nuclei in Upper Energy States (dimensionless)

N_{lower}= Number of Nuclei in Lower Energy States (dimensionless)

Q= Charge (C)

R= Universal Gas Constant (J/ mol K)

R= Resistance (Ω)

T= Temperature (K)

Z= Impedance (Ω)

α= Charge Transfer Coefficient (dimensionless)

β= Half the Angle of the Cone of Light from Specimen Plane Accepted by the Objective

(Half Aperture Angle in Radians)

γ= Magnetogyric Ratio (1/Tesla sec)

λ= Wavelength of Imaging Radiation (Å)

μ= Dipole Moment (Cm)

η= Overpotential (V)

φ= Phase Angle (degrees)

Ψ= Current Function (dimensionless)

ω= Radial Frequency (Hz)

$m \sin \beta$= Numerical Aperture

LIST OF TABLES

LIST OF FIGURES

I. INTRODUCTION

The demand for sustainable alternative energy and carbon neutrality has been rising exponentially over recent years [1, 2]. The energy sector desires a cheaper, cleaner, and abundant energy source alternative to traditional fossil fuels. In fact, by 2050, global annual greenhouse gas emissions will need to be reduced by 85%. This massive energy revolution to reduce greenhouse gas emissions and secure a sustainable energy supply will require renewable energy to be increasingly integrated [3]. Renewable energy sources include sunlight, biomass, wind, water, tidal, hydrogen, and geo-thermal and can be further explained in Figure 1 [4].

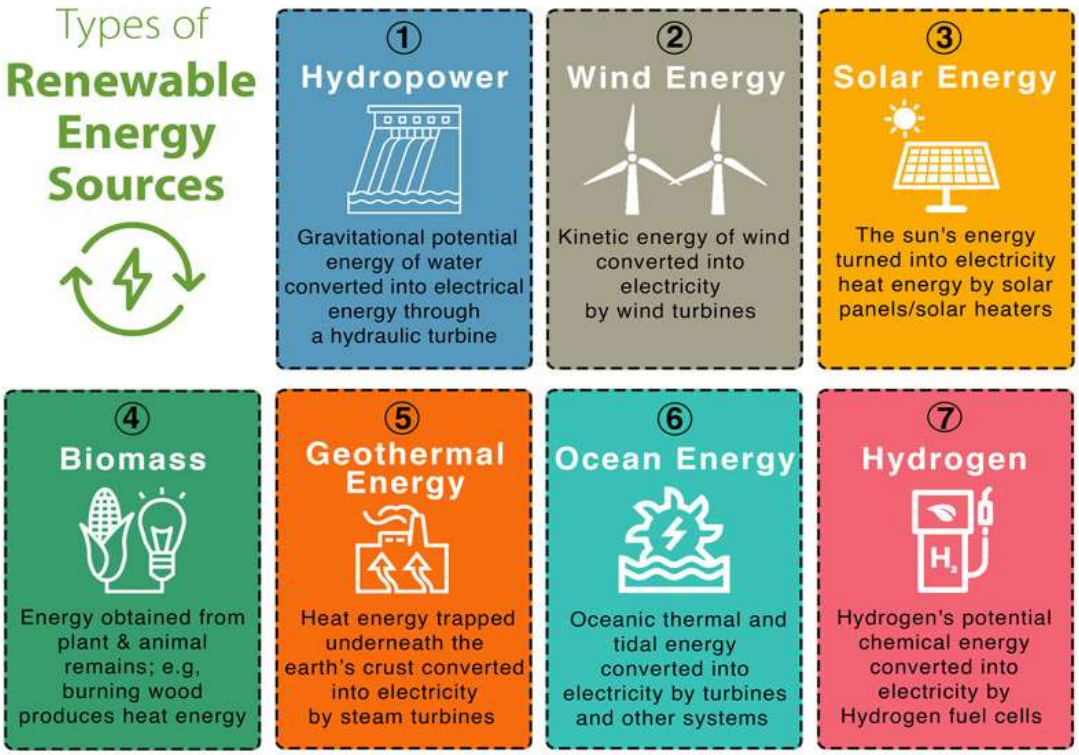

Figure 1. Types of renewable energy sources [4].

Of these, solar energy is by far the most promising renewable resource to meet these demands due to its enormous untapped availability from the sun [5], with 1000 times more

energy reaching the earth's surface from the sun than is emitted by all fossil fuels consumed [6]. However, its capture and conversion, storage, and release are needed to properly utilize solar power [2]. Advanced clean energy conversion technologies, such as electrochemical water splitting and fuel cells, which are key components in the utilization of renewable energies for the future, require hydrogen as their key energy carrier [7-9].

A. Hydrogen Production

Hydrogen, the simplest and most abundant element, in its elemental form is one of the most attractive energy carriers due to its high energy density and flexibility [3, 10]. Hydrogen is produced in many ways including via natural gas, coal, biomass, and water. Depending upon how the hydrogen is produced, it is commonly categorized in one of three ways, as either grey, blue, or green hydrogen. Grey hydrogen comes from coal or natural gas without the implementation of carbon capture and storage (CCUS), while blue hydrogen also comes from coal or natural gas but does use CCUS. On the other hand, green hydrogen is made by using renewable energy to split water. The different hydrogen types based on production method can be illustrated further in Figure 2 [11].

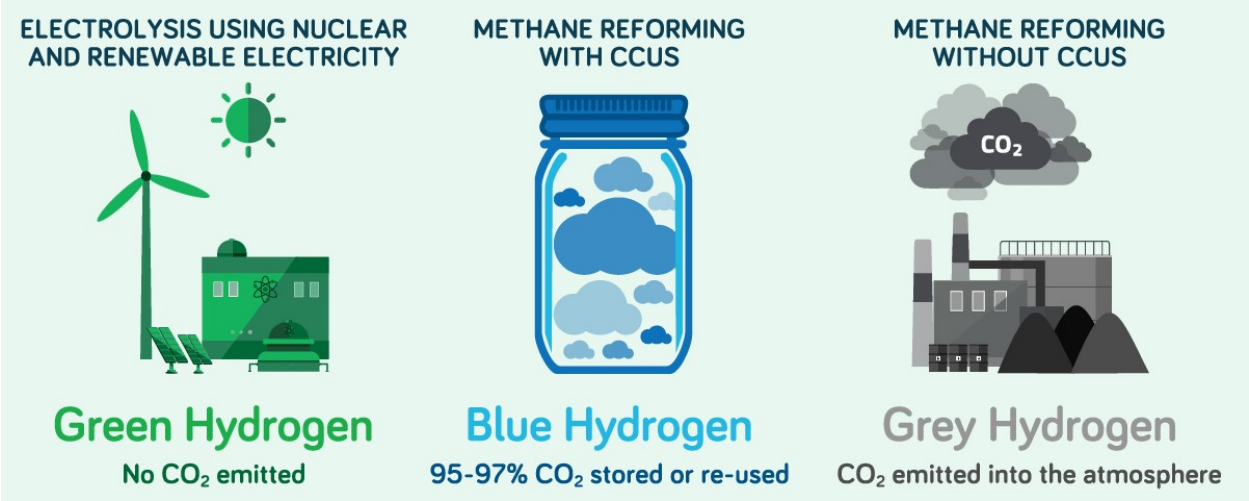

Figure 2. The three different hydrogen production methods [11].

The main production of hydrogen currently comes from natural gas, which utilizes steam reforming to convert a hydrocarbon-based fuel, such as methane, catalytically into hydrogen rich streams[12]. However, this technology is not sustainable due to its high air emissions. Coal gasification is low cost and can produce considerable amounts of hydrogen, but to reduce emissions to favorable levels would require too much reserve depletion to be sustainable. Although biomass is a sustainable energy source, it cannot supply the amount of hydrogen required long-term [13]. Conversely, splitting water to make hydrogen using solar energy could theoretically produce the required energy and cost savings necessary for solving the energy crisis. In Figure 3, it is projected that by 2050 the demand for hydrogen fuel will increase ten-fold [14]. Further, in Figure 4, it can be seen that over half of the hydrogen demand by 2050 will come from green hydrogen production by water splitting [15].

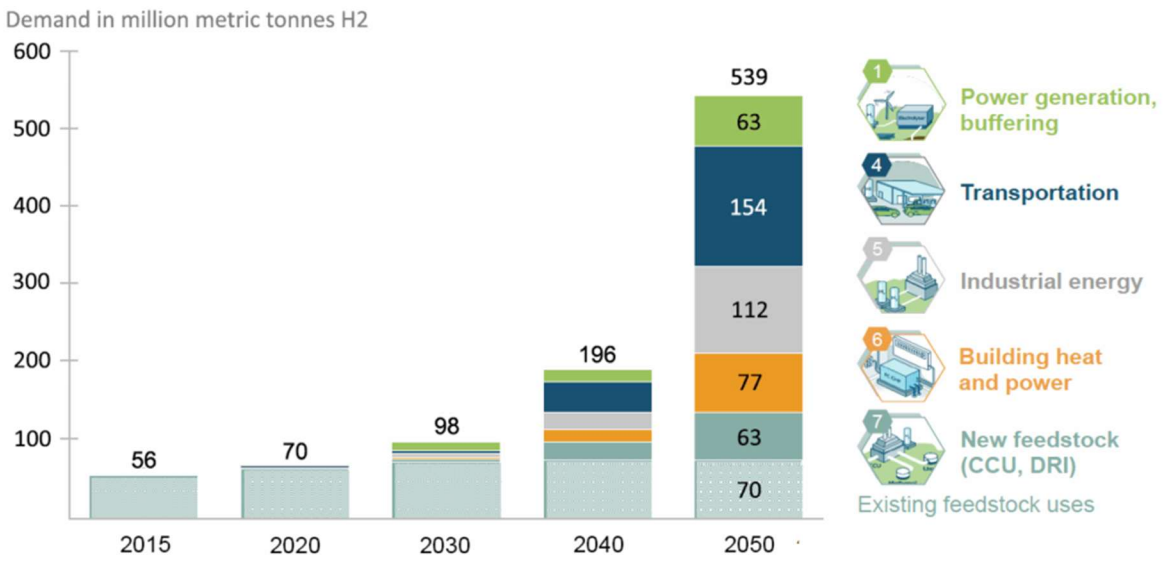

Figure 3. The global hydrogen fuel demand projection [14].

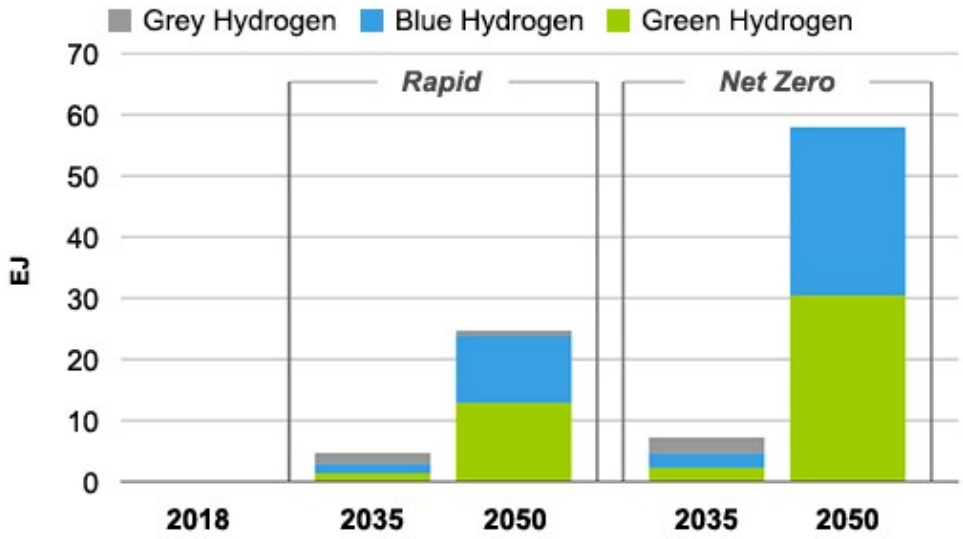

Figure 4. Hydrogen demand projection by type [15].

B. Solar Energy Capture and Conversion

The energy from the sun can produce the amounts of energy required to provide enough power for all of the world's energy needs, if harvested and stored efficiently. There are two main technologies in use to capture and convert sunlight, predominantly photovoltaic (PV) cells and

more recently photoelectrochemical (PEC) cells. PV cells are more commonly put in practice today and produce electricity from solar energy that must be instantly used or otherwise stored in a secondary device, such as a battery [16].

Conversely, in nature, sunlight is harvested by plants and converted into chemical fuel by photosynthesis [5, 12]. An artificial photosynthesis of sorts, called photoelectrolysis, has been proposed as a more practical method to store solar energy as fuel in comparison to PV-electrolysis. In photoelectrolysis, the light-harvesting and electrochemical processes are performed in a single, integrated device known as a photoelectrochemical (PEC) cell which splits water into elemental hydrogen and oxygen fuel [5, 17]. A diagram of the differences in the pathways of PV versus PEC cells can be shown in Figure 5. Even though water splitting is a hopeful means to the production of sustainable hydrogen fuel, its widespread adoption is hindered by high costs and inefficient mechanisms in comparison to fossil fuels [5, 12, 13, 17, 18].

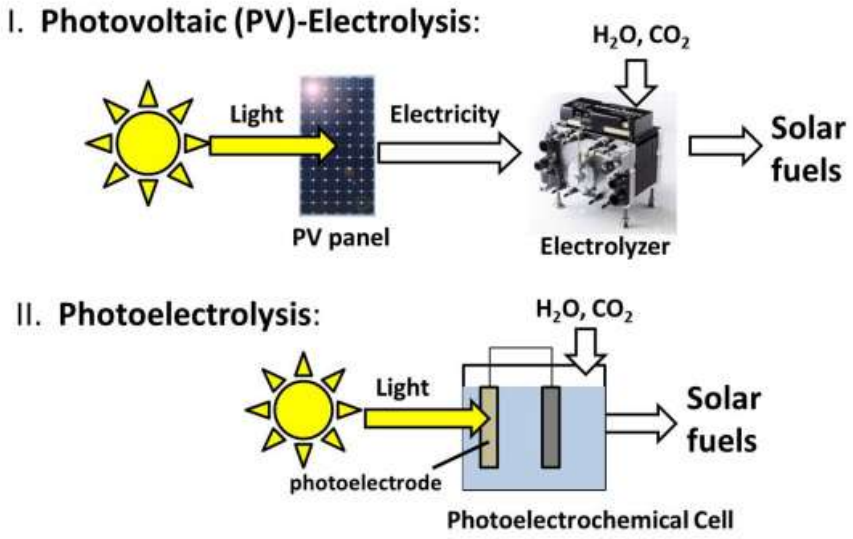

Figure 5. Two pathways for conversion of solar energy into solar fuels such as hydrogen [16].

C. Electrolysis of Water

The electrolysis of water involves the decomposition of water into hydrogen and oxygen gas by using an electric current that is being passed through the water. As shown in Figure 6, water is reduced to hydrogen at the cathode and oxidized to oxygen at the anode. In PEC cells, an aqueous electrolyte completes the current loop between the electrodes and an external circuit supplying the current [17].

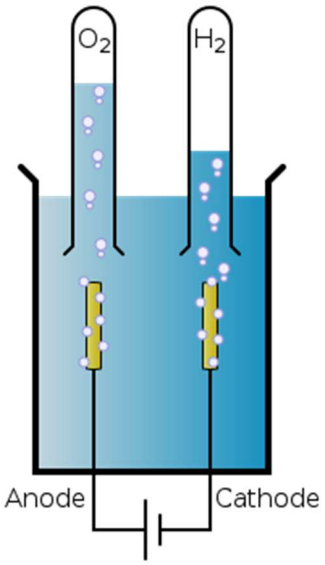

Figure 6. Simple schematic of the electrolysis of water [19].

The global electrolysis reaction taking place is [17, 20]:

$$H_2O(aq) \rightarrow H_2(g) + \frac{1}{2}O_2(g) \quad (1)$$

In the water electrolysis process, the electrons are either taken or released by the ions at the electrode surface. The electrons flow to the cathode from the outside circuit to negatively polarize it, which attributes to the reduction half-reaction taking place there. The anode is where

the oxidation half-reaction occurs and is when the electrons leave the anode to go to the outside circuit to positively polarize it. Therefore, hydrogen is being generated at the cathode while oxygen is generated at the anode [17, 20].

The two half-step reactions occurring at the anode and cathode are shown in Equations 2 and 3, respectively [7, 8, 21]:

$$H_2O(aq) \rightarrow 2H^+(aq) + 2e^- + \frac{1}{2}O_2(g) \quad (2)$$

$$2H^+(aq) + 2e^- \rightarrow H_2(g) \quad (3)$$

Equation 2 is referred to as the anodic oxygen evolution reaction (OER). The electrocatalytic hydrogen-evolution reaction (HER), Equation 3, is the main cathodic reaction step of the water splitting process ($2H^+ + 2e^- \rightarrow H_2$) [9, 21].

D. Current HER Catalysts

Catalysts can be used to increases the rate of a reaction without being consumed itself. The development of an effective artificial water-splitting catalyst has been a focus, as well as a challenge, for many engineers and scientists alike [17, 22]. The hydrogen adsorption and desorption on the electrode surface are not only successive steps, but also competitive. An affective HER catalyst should not form too weak of a bond with the adsorbed H* to ensure proton-electron transfer, and at the same time not form too strong of a bond that the hydrogen gas may still be released after breakage, as outlined by the Sabatier principle [9, 23].

Exchange current density is a background current caused by the electron transfer at the electrode/electrolyte interface and is used to normalize net current. The maximum exchange current density when hydrogen adsorption takes place is close to ΔG_H=0, which is thermoneutral

[24, 25]. Measured exchange current density of an HER electrocatalyst can be plotted as a function of calculated hydrogen adsorption Gibbs free energy (calculated using density function theory) in what is known as a volcano plot. Figure 7 shows a volcano plot for various metals and nanoparticulate MoS_2 [26]. Gibbs free energy can be a useful tool in selecting an HER electrocatalyst by describing its electroactivity [25].

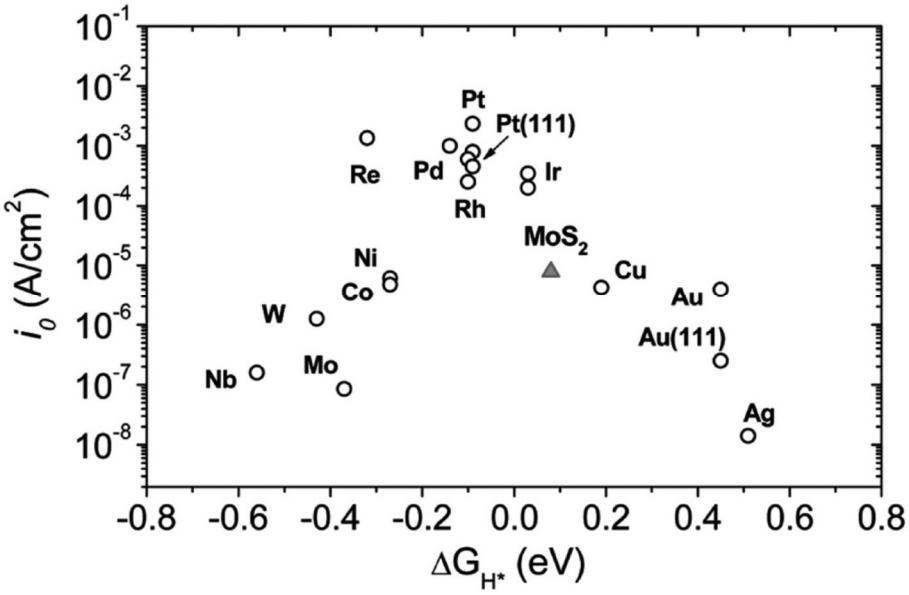

Figure 7. Volcano plot for nanoparticulate MoS_2 and pure metals [26].

It is true that Gibbs free energy is an important property for an HER electrocatalyst, but the activity of them is influenced by an array of factors such as crystallinity, conductivity, and roughness. Much research has been gathered in regard to structure and composition of electrocatalysts to help promote active site activity, which has proven electrochemically favorable as opposed to bulk materials [27]. Such nanostructured electrocatalysts will be outlined below.

Commonly studied catalysts are named for and derived from two basic groups, precious group metals and non-precious group metals. Precious group metal (PGM) catalysts, like the name implies, are derived from precious group metals. These PGM catalysts are unmatched in their catalytic activity and durability. Platinum, ruthenium, rhodium, palladium, and iridium are all members of this group [7, 8, 28, 29]. To date, the most efficient and popular PGM electrocatalyst for HER is by far platinum due to its low Tafel slope high current density, which makes it the benchmark for all other HER electrocatalysts. Platinum electrocatalysts studied in literature having near-zero potential ranges and Tafel slopes ranging anywhere from 30-150 mV/dec [30]. However, platinum and other precious metals' high cost and insufficient reserves greatly hinder their widespread use [7-9, 22, 31].

As an alternative, HER catalysts made from cost-effective alternatives with ample reserves must be developed without precious group metals. Such catalysts candidates have been highly fabricated and studied, are often called non-PGM or PGM-free electrocatalysts and are typically comprised of earth-abundant transition metals [9, 32]. These PGM-free catalysts offer respectable activity with the benefit of being much more reasonably priced for increased commercialization and distribution, despite drawbacks of having poor stability due to corrosion and oxidation in acidic media [8]. PGM-free catalysts development has included elements such as iron [33], molybdenum [34], cobalt [31], zinc [35], tungsten [35], copper [36], and nickel [37] as alloys [32, 35], metal complexes [38, 39], nitrides [40], carbides [41], sulfides [42], phosphides [43], borides [44], and selenides [22].

In addition to these, some carbon-based nanostructured materials without metals have also been proposed as a suitable replacement for platinum due to their unique properties. Carbon materials themselves are electrochemically inactive, so chemical modification must be done on

these materials. Some carbon-basted electrocatalysts include carbon nanotubes and graphene nanosheets [45-48].

Out of all non-PGM electrocatalysts, nanostructured molybdenum sulfides (of the transition metal chalcogenide family) are the current best alternative for platinum. MoS_2 has a unique layered structure with edges that contribute greatly to electrocatalytic activity, and it is highly stable in acidic media. Increasing these active sites has significantly improved the catalytic HER activity and much work has been done regarding this modification [34, 42, 49-51]. Prior research has reported MoS_2 catalysts on carbon paper [52], gold [26], graphite [53], and activated carbon [42] with a variety of overpotentials ranging from∼0.1 to∼0.4 V [54] and Tafel slopes of 55-60 [26] to >120 mV/dec [52].

E. Research Aims

There should be a distinction made between heterogeneous and homogeneous catalysts. Heterogeneous electrocatalysts for HER are insoluble species having a different phase as the substrate, such as metals, while homogeneous type electrocatalysts have the same phase as the substrate, like soluble, small molecular complexes [8]. Heterogeneous catalysts do degrade at a slower rate than homogeneous catalysts do, and they have a variety of active sites that are difficult to both quantify and define. Homogeneous catalysts, on the other hand, are more easily studied because of the ability to clearly quantify and identify their active centers. Even though the activity and selectivity of homogeneous catalysts is promising, they have the problem of easily separating the products from the catalysts themselves [26, 32].

To combine the benefits of both heterogeneous and homogeneous catalysts, immobilization of characterized homogeneous catalysts onto the solid electrode surface to allow

them to work under heterogeneous conditions is proposed. This heterogenization of a homogeneous catalyst onto the electrode surface is an ideal way to study a catalyst and has been studied to some degree [55-61]. By changing the electrocatalysts chemically or physically, the immobilization method can be successful. The catalyst and the surface can be bound by chemical methods, such as covalent bonding, or by physical methods, using weaker interactions such as van der waals.

As of late, thiomesicarbazone (TSC) ligands have become a new interest of study as possible homogeneous electrocatalysts to heterogenized onto electrode surfaces. TSC ligands are organosulfur compounds and can function as a reservoir for charge with hydrogen evolution at either the metal or ligand and operate, depending upon the metal, via ligand-assisted metal-centered [62], ligand-centered [63], or metal-assisted ligand-centered reactivity [64, 65]. These structures have the benefits of ease of synthesis, low molecular weight, stability under ambient conditions, low cost, stability in acidic solutions, and sustainability [22].

A major advantage of the ligand-centered and metal-assisted ligand-centered approach is that the organic framework functions as the active site allowing the development of catalysts that are metal-free or promoted by sustainable transition- (Cu) or non-transition metals (Zn). The ligand assisted metal-centered approach employs Ni and follows more traditional HER reactivity involving metal-hydride intermediates. This fundamental shift in mechanism provides the opportunity to explore materials based on this underrepresented class of HER catalysts, and the possibility of sustainable catalyst development with inexpensive materials containing first-row metals or no metals.

The Grapperhaus/Buchanan Research Group has developed and studied several ligand based catalysts for HER including rhenium-thiolate (ReL_3), zinc diacetyl-bis(N-4-methyl-3-thiosemicarbazide) (ZnL), diacetyl-bis(N-4-methyl-3-thiomesicarbazone) (H_2L), diacetyl-bis(N-4-methyl-3-thiosemicarbazonato) (CuL), and copper bis(thiomesicarbazone) complexes with pendent polyamines [63, 64, 66, 67]. Most recently, the Grapperhaus/Buchanan Research Group has worked in conjunction with the Gupta Research Laboratory to evaluate the effect of stacking interactions on the translation of a series of structurally related bis(thiosemicarbazonato) nickel(II) HER catalysts on glassy carbon electrode surfaces [22].

The goal of this work is to develop and engineer new carbon materials, heterogenizing new and existing homogeneous thiomesicarbazone (TSC) compounds, supplied by the Grapperhaus/Buchanan Research Group, as electrocatalysis of HER. It is hypothesized that the interplay between the TSC catalysts and their microenvironment on surfaces may control the activity of heterogenized molecular catalysts, and that modification of this microenvironment can be done to improve HER electrocatalytic activity. The driving factors for the work will be to mitigate current thermodynamics, kinetics, and transport limitations.

Using existing and new derivatives of TSCs, the thermodynamics of how these homogeneous TSC HER catalysts attach to electrodes to become heterogeneous will be studied by preparing stable surfaces of these electrocatalysts by non-covalent attachment using physisorption of the complexes on glassy carbon and evaluating their HER activity. Enhancing kinetic properties of electron transport via attachment onto surfaces will be done either by using covalent attachment via linkers and metalation, or by more robust non-covalent pi-bond attachment using pyrene as an anchoring piece. Transport will be increased by using high surface

area carbon systems with increased number of active sites, namely standard pencil and carbon paste electrodes.

Presently, glassy carbon electrodes (GCE) are the most widely used carbon support for electrochemical characterization of non-PGM catalysts due to its stability and inert nature [68, 69]. That being said, there are a lot of issues that glassy carbon can present, such as the requirement of extensive cleaning and polishing after each use, the fact that they are non-disposable, and their high cost. Taking all of this into account, it is desired to fabricate carbon derivatized materials that display high catalytic activity and excellent long-term stability, while being inexpensive and disposable [70].

One proposed solution to this problem is using disposable standard pencil electrodes for a replacement to glassy carbon to preliminarily characterize electrochemical catalysts [69-74]. Standard medium-hardness HB pencils are made up of 68% graphite, 26% clay, and 5% wax [75-77]. The pencils can have the fillers in them removed to better augment the kinetic properties of the pencils by providing a porous carbon material for catalysts to coat [75]. In addition, the fact that pencils are cheap, disposable, can be cleaved to regenerate the surface, are available over the counter, and more importantly are amenable for post characterization make them a viable support material for carbon to electrochemically characterize catalysts [69, 71, 72]. The Gupta Research Laboratory has studied pencil electrodes in depth and, therefore, they will be further studied for this work with TSCs [78].

Another proposed modified electrode material is carbon paste electrodes (CPEs), composed primarily of organic liquid and graphite powder to form a paste. CPEs are popular for several reasons including in instances in which compounds needing to be studied are barely

soluble, the materials are available at low costs, and they have the advantage of being easily prepared and modified when necessary [79-82]. CPEs have been modified and discussed in several papers as a suitable carbon surface to improve HER catalysis and will be tested for our TSC application [82-86].

II. BACKGROUND

First, an overview of electrochemistry will be presented. This will be followed by description of the fundamentals of HER. Next, common electrochemical techniques will be provided to give background to the experimental section. Finally, any other data analysis methods used will be presented and discussed.

A. Electrochemistry Defined

The branch of chemistry dealing with the relationship between both chemical and electrical effects is known as electrochemistry, specifically chemical changes caused by production of electrical energy and passing of electric current by chemical reactions. Electrochemistry is quite a broad branch of chemistry and includes a wide array of phenomena including fuel cells and batteries. Knowing this, the basic principles that drive electrochemistry apply to study all different kinds of chemical systems [87].

B. Electrochemical Cells and Reactions

In studying electrochemical systems, the primary concern is with the factors that affect the charge transfer across chemical interfaces, mainly between the electrical conductor, called the electrode, and the ionic conductor, called the electrolyte. This electrolyte/electrode interface is the focus of where potential is applied and current passes through by the movement of electrons through the electrode (in our case, carbon material) and through the electrolyte (acidic aqueous solution) via movement of ions. This system must be sufficiently conductive to promote useful data generation[87].

Electrochemical systems are most conveniently studied in electrochemical cells, which generally have at least two electrodes separated by an electrolyte phase. The difference in

electric potential is measured between the different electrodes in this electrochemical cell and will occur primarily at the interphase. The magnitude of the difference in electric potential will control the rate of charge transfer, as explained previously, which is why the makeup of the electrochemical cell is extremely important [87].

Since the overall reaction taking place in the cell consists of two half-reactions, each of them will correspond to the potential difference at its own electrode. Because we are only concerned with one of the half-reactions, we call this electrode the working electrode. The other electrode is standardized by fixing its potential and is called the by reference electrode. The reference electrode has a constant chemical makeup so that the working electrode's potential is observed with respect to it. In addition, it is necessary to add what is called a counter electrode for the current to pass between it and the working electrode to overcome ohmic drop required to drive the ionic current in solution. The counter electrode is chosen so that it does not produce any substances that interfere with the reactions happening at the working electrode surface and is placed in a separator [87]. The working electrode for these experiments will be either glassy carbon, standard pencil, or carbon paste. The reference electrode will always be silver-silver chloride (Ag/AgCl), and the electrolyte solution will be aqueous 0.5 M H_2SO_4. The counter electrode will always be a graphite rod.

C. Fundamentals of HER

The working electrode is driven to more negative potentials by connecting the negative power supply end to it. Once the energy level is high enough for transfer the electrons move from the electrode to the electrolyte solution; this movement is known as a reduction or cathodic flow. The HER is a reduction reaction so this is the pathway our experiments will take. The

reverse is also true for if you want to observe an oxidation or anodic flow, you simply impose a positive potential and the electrons in the electrolyte solution will transfer to the electrode [87].

The potentials at which reduction and oxidation occur are related to the standard reference potential of the specific chemical species present in the system itself. In the case of HER, as seen in Equation 4, the standard reduction potential for HER water electrolysis is pH-dependent referenced to the international standard hydrogen electrode (SHE) or normal hydrogen electrode (NHE), while in reference to the reversible hydrogen electrode (RHE) is much more straightforward and is always zero, no matter what electrolyte is being used [88]:

$$E_{HER} = E^{0}_{(\frac{H_2}{H^+})} - \frac{RT}{F} \times \ln\left(\frac{a_{H^+}}{p_{H_2}^{\frac{1}{2}}}\right) = -0.059 \times (pH)\ vs.\ NHE = 0\ V\ vs.\ RHE \quad (4)$$

Where:

E_{HER}= Standard Reduction Potential Needed for Hydrogen Evolution Reaction (V)

E^0= Standard Potential (V)

R= Universal Gas Constant (J/mol K)

T= Temperature (K)

F= Faraday's Constant (C/mol)

a= Activity of Hydrogen Ion (mM)

p= Pressure at Which Electrolysis Takes Place (atm)

The standard reduction potential represents the thermodynamic equilibrium potential at which the reaction will occur. Despite the standard reduction potential being 0 V, as with most

chemical reactions, the electrochemical reaction is not activated at this equilibrium potential, but also has to overcome the activation energy barrier to occur, which can be illustrated in Figure 8

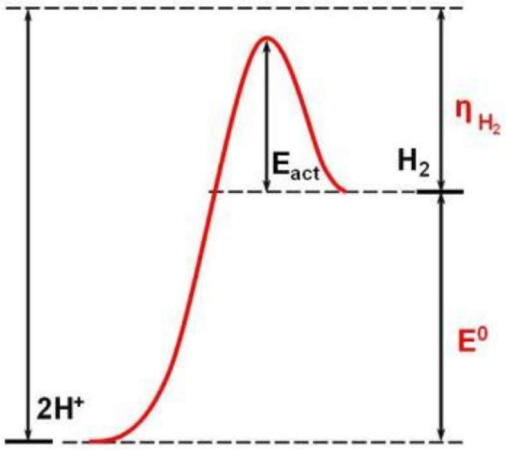

Figure 8. HER activation energy barrier example [27].

This barrier in electrochemistry is referred to as the overpotential, which is the difference between equilibrium potential and applied potential. HER will not begin unless sufficient cathodic potential is applied with overpotential, and depending upon the catalyst present, can be greater than 1 V (Figure 9). That being said, the potential to drive HER forward is expressed as [27]:

$$E_i = E_{HER} + iR + \eta \quad (5)$$

Where:

E_i= Total Applied Potential (V)

iR= Ohmic Potential Drop (V)

η= Overpotential (V)

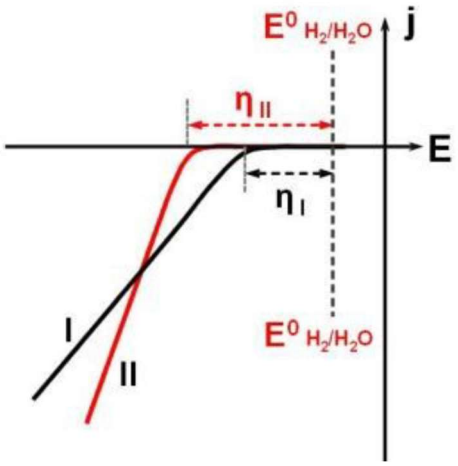

Figure 9. Onset overpotentials for two different HER electrocatalysts [27].

Overpotential is one of, if not the most, important parameter used to evaluate an electrode's performance in electrochemical applications. Higher overpotentials have lower energy efficiency, and lower overpotentials have greater energy efficiency. With the help of efficient electrocatalysts which are employed to activate intermediate chemical transformation, the overpotential can be lowered to promote reaction rate. Generally speaking, HER electrocatalysts should be able to catalyze the reaction within 100 mV overpotential or, ideally, less. [5, 27, 31].

Kinetics of HER is quite a complex subject. The resistance formed by the kinetically controlled electrochemical reaction is called the charge transfer resistance, and the reaction rate of the HER is called current density. The current density highly depends on the overpotential relationship called the Butler-Volmer equation [51]:

$$j = j_0[e^{(1-\alpha)\eta Fn/RT} - e^{-\alpha\eta Fn/RT}] \quad (6)$$

Where:

j= Current Density (A/m^2)

j_0= Exchange Current Density (A/m^2)

n= Number of Electrons Transferred, 1 (dimensionless)

α= Charge Transfer Coefficient (dimensionless)

The exchange current density is another important electrode parameter which describes the equilibrium reaction rate and is also useful to evaluate electrochemical activity. When overpotential is small, less than 0.005 V, the Butler-Volmer equation becomes [27]:

$$\eta = \left(\frac{RT}{nFj_0}\right) j \tag{7}$$

This shows a linear relationship between current density and overpotential near the equilibrium potential. When overpotential is above 0.005 V, the Butler-Volmer equation becomes the Tafel equation [27, 29]:

$$\eta = a + b\log j = -\frac{2.3RT}{\alpha nF}\log j_0 + \frac{2.3RT}{\alpha nF}\log j \tag{8}$$

Where:

a= Tafel Equation Constant (V)

b= Tafel Equation Constant (V)

The theoretical values for the Tafel equation constants depend upon the specific anodic or cathodic process. This Tafel equation shows a linear relationship between log j and overpotential with the constant $b = \frac{2.3RT}{\alpha nF}$, commonly called the Tafel slope. Determination of which step in a reaction is rate-controlling can be done in evaluation of the Tafel slope values experimentally by

analysis of Tafel plots, which plot overpotential versus the log of the current density [9]. The Tafel slope is used to give the necessary overpotential value required to raise current density ten-times. Therefore, a low Tafel slope value gives a large rise in current density, which should be characteristic of ideal electrocatalysts along with small overpotentials. Yet, these parameters are not always synonymous with one another, as in the case with HER electrocatalysts. These catalysts often have small current densities and small Tafel slopes, or vice versa, as shown in Figure 10. Given this, it is always best to choose the electrocatalyst for HER that has smaller overpotential at the required current density of 10 mA/cm^2, which is the value needed for solar fuel synthesis [89].

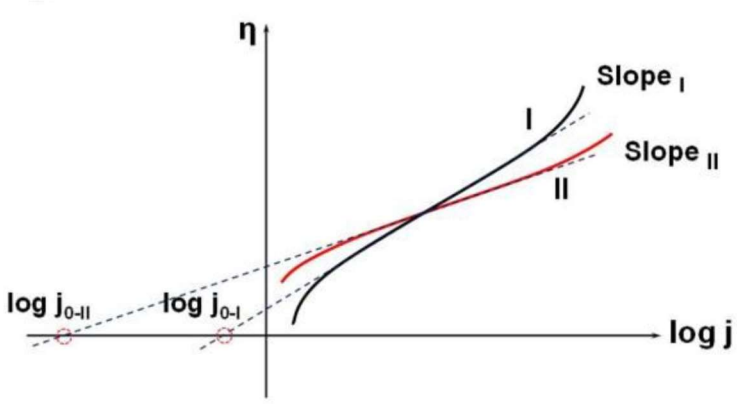

Figure 10. Tafel plots for two different electrocatalysts [27].

HER kinetics is influenced greatly by its reaction pathway, and it is a multi-step process which takes place at the surface of the cathode which generates gaseous hydrogen. The HER reaction pathway in acidic solution conditions is outlined in Equations 9-11 [7].

$$H^+(aq) + e^- + {}^* \rightarrow H^*\ (Volmer) \tag{9}$$

$$H^+(aq) + e^- + H^* \rightarrow H_2(g)\ (Heyrovsky) \tag{10}$$

$$or\ 2H^* \rightarrow H_2(g)\ (Tafel) \quad (11)$$

No matter the second step, the first step always follows the Volmer (Equation 9) pathway in which adsorption of H on the electrode surface is occurring by the transfer of a proton from the acid electrolyte which combines with an electron transferred from the electrode surface. The preceding step either occurs via the Heyrovsky (Equation 10) or Tafel (Equation 11) pathway. The Heyrovsky reaction involves the adsorbed hydrogen atom combining with the electron transferred from the electrode surface along with a proton from the electrolyte to form a single hydrogen molecule. The Tafel reaction involves two adjacent adsorbed hydrogen atoms combining to form one hydrogen molecule. The rate-determining step of HER changes in different potential ranges. At low potentials, hydrogen adsorption will be the rate-determining step, but the electron transfer is not as fast as desorption. At high potential, it the hydrogen adsorption rate will be higher than the desorption rate, and the desorption reaction will be the rate-determining step [7].

Which pathway will be taken is difficult to determine, but depends upon the inherent electronic and electrochemical properties of the electrode surface itself, and the Tafel slope is used to discern which step is rate determining, as aforementioned. Butler-Volmer kinetics has found that the Volmer step (also called discharge reaction) is rate-determining when the Tafel slope is 118 mV/decade; the Heyrovsky step (also called electrochemical desorption reaction) is rate-determining when the Tafel slope is 39 mV/decade, and the Tafel step (also called recombination reaction) is rate-determining when the Tafel slope is 29.5 mV/decade [27].

D. Electrochemical Measurement Techniques

Applying an electrical perturbation and observing the resulting characteristic changes of an electrochemical system is how information about that system is gained. Common electrochemical measurement techniques used include linear sweep voltammetry, cyclic voltammetry, electrochemical impedance spectroscopy, and square wave voltammetry. These techniques will be outlined below.

i. Linear Sweep Voltammetry

One common electrochemical measurement technique that will be used as a main metric of measuring is linear sweep voltammetry (LVS). In LSV, a fixed scan rate, v_s, is used to sweep the DC potential between a lower and upper limit, E_1 and E_2, to measure the current at the working electrode [90]. The signal output graph of the potential versus time is shown in Figure 11a, where it's linearity can be seen. The oxidation or reduction of the species shows up as a peak or trough in the current signal, as shown in Figure 11b:

$$E = E_1 - v_s t \tag{12}$$

Where:

t= Time (s)

v_s= Scan Rate of the Potential Sweep (V/s)

E= Electrode Potential (V)

E_1= Lower Limit Potential (V)

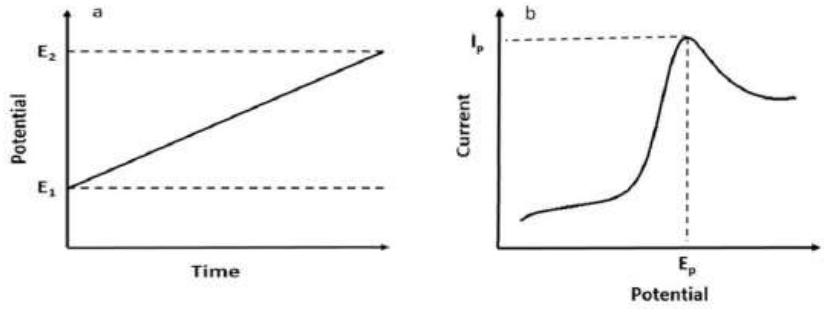

Figure 11. Signal output (a) and linear sweep voltammogram peak (b) example [91].

It is necessary to rationalize the behavior of voltage sweeping. The rate of equilibrium is established at the electrode surface by the influence of voltage [92]. The voltage sweep rate is slow in comparison to the rate of electron transfer, so the equilibrium at the electrode surface is established and peak potential, E_p, is reached, as predicted by the Nerst Equation [91]:

$$\left|E_p - E_{\frac{p}{2}}\right| = 2.2\frac{RT}{F} \tag{13}$$

Where:

E_p= Peak Potential (V)

$E_{p/2}$= Half Peak Potential (V)

F= Faraday Constant (C/mol)

R= Universal Gas Constant (J/K mol)

T= Temperature (K)

Peak current, I_p, is dependent upon the scan rate and concentration of reactant as explained by the commonly used Randles-Sevcik Equation [93]. Here, the value of peak current is linearly related to the square root of scan rate.

$$\left|I_p\right| = 0.4463nAFC_{bulk}\left(\frac{nFv_sD_A}{RT}\right)^{\frac{1}{2}} \quad (14)$$

Where:

n= Number of Electrons Transferred (dimensionless)

A= Effective Area of Electrode (cm^2)

C_{bulk}= Concentration of Bulk (mol/L)

D_A= Diffusion Coefficient (cm^2/s)

I_p= Peak Current (A)

ii. Cyclic Voltammetry

LSV is quite similar to another electrochemical technique called cyclic voltammetry (CV). In fact, CV is often referred to as an extension of LSV and also uses DC potential. For CV, a voltage is swept at a fixed rate between two different values and then it is reversed and swept back to the initial value [92]. A typical CV signal output and corresponding CV is shown below in Figure 12 [91].

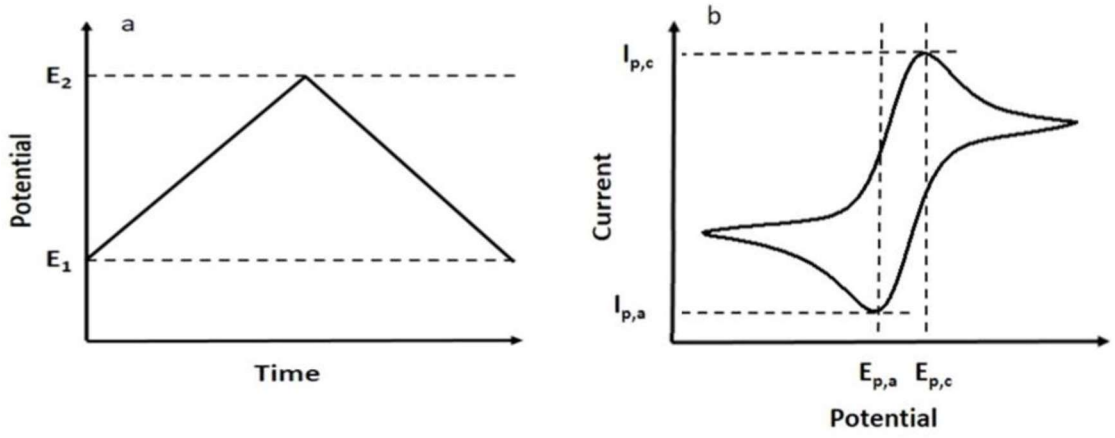

Figure 12. (a) The signal output of a CV and (b) corresponding CV [91].

For an ideal reversible reaction the peak current height for the oxidative ($I_{p,a}$) and reductive ($I_{p,c}$) processes should be the same [94]:

$$\frac{|I_{p,c}|}{|I_{p,a}|} = 1 \tag{15}$$

Where:

$I_{p,c}$= Cathodic Peak Current (A)

$I_{p,a}$= Anodic Peak Current (A)

The separation of the peak potential is only related to the number of electrons transferred in the reversible reaction and the temperature, as shown in Equation 16 [91]:

$$\left|E_{p,c} - E_{p,a}\right| = 2.218\frac{RT}{nF} \tag{16}$$

Where:

$E_{p,c}$= Cathodic Peak Potential (V)

$E_{p,a}$= Anodic Peak Potential (V)

Half-wave potential, $E_{1/2}$, is an important parameter when studying electrochemical systems and is related to the thermodynamic potential of the reaction [95, 96]:

$$E_{\frac{1}{2}} = \frac{E_{p,c}+E_{p,a}}{2} \tag{17}$$

$$E_{\frac{1}{2}} = E(t) + \frac{RT}{nF}\ln\left(\frac{D_R}{D_O}\right)^{\frac{1}{2}} \tag{18}$$

Where:

$E_{1/2}$= Half-Wave Potential (V)

D_R= Diffusion Coefficient of Reductant (cm^2/s)

D_O= Diffusion Coefficient of Oxidant (cm^2/s)

iii. Square-Wave Voltammetry

In some cases, CV cannot detect complicated electrochemical reactions accurately enough to determine potential. When this is the case, another technique can be deployed to have the input signal disturbed to enhance sensitivity of potential. This most common use of this technique is square-wave voltammetry [97]. Square-wave is a popular analysis approach due to its high sensitivity via background suppression and capability to directly analyze at a wide range of time scales [87, 98].

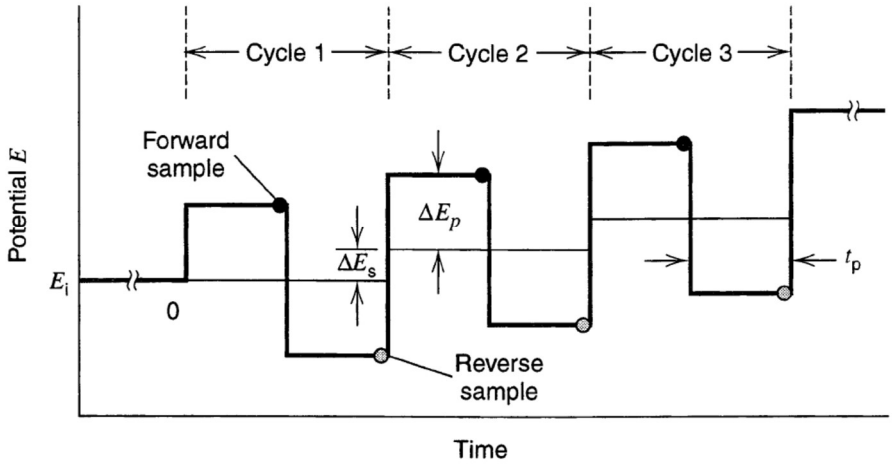

Figure 13. Waveform of square-wave voltammetry [87].

Figure 13 demonstrates a waveform of a square-wave potential on a staircase. The input signal has a step height, ΔE_s, an amplitude, ΔE_p, and step width for time, t_p. The scan rate, v, and the frequency, f, of the square wave model is described by:

$$f = 1/2t_p \tag{19}$$

$$v = \frac{\Delta E_s}{2t_p} = f\Delta E_s \tag{20}$$

Where:

f= Frequency (Hz)

t_p= Pulse Width Time (s)

v= Scan Rate (V/s)

ΔE_s= Amplitude or Staircase Height (V)

The potential step and magnitude of the time scale are separately determined during an experiment by t_p and ΔE_s. The current of each pulse is calculated using [99]:

$$i = \frac{nFAD^{\frac{1}{2}}C}{\sqrt{\pi t_p}} \Psi(\Delta E_s, \Delta E_p) \quad (21)$$

Where:

i= Measured Current of Each Pulse (A)

D= Reactant Diffusion Coefficient (cm^2/s)

C= Bulk Concentration of Reactant (mol/L)

Ψ= Current Function (dimensionless)

ΔE_p= Step Width or Pulse Height (V)

Figure 14 shows the forward, reverse, and difference of the current responses versus voltage. The potential when the current difference reaches its maximum is $E_{1/2}$, which is a key characterization parameter for the electrochemical reaction.

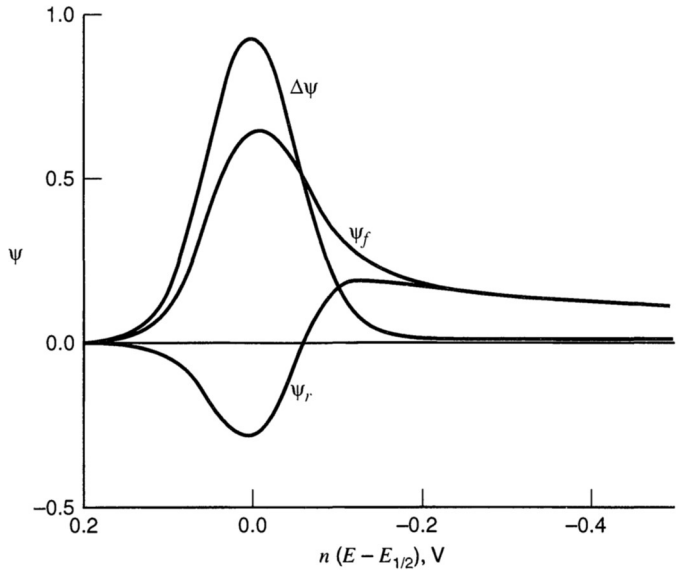

Figure 14. Normalized square-wave response [87].

iv. Electrochemical Impedance Spectroscopy

The study of the variation of impedance with the frequency of a small-amplitude AC disturbance for an electrochemical system is known as electrochemical impedance spectroscopy (EIS). Impedance is described as the ability to resist the flow of an electrical current without the restrictions of Ohm's law. Ohm's law is used to define the resistance, specifically, it is the complex resistance of current flowing through a circuit [100]:

$$R = \frac{E}{I} \tag{22}$$

Where:

I= Current (A)

R= Resistance (Ω)

This defined relationship is only valid for an ideal resistor. In actuality, circuit elements exhibit much more complicated behavior. Due to this, resistance is replaced with impedance. The small amplitude feature of the perturbation that flows through the system in EIS must be small enough to maintain linearity [101]. As shown in Figure 15, in linear systems, the current response to a sinusoidal potential is a sinusoidal shifted at the same frequency.

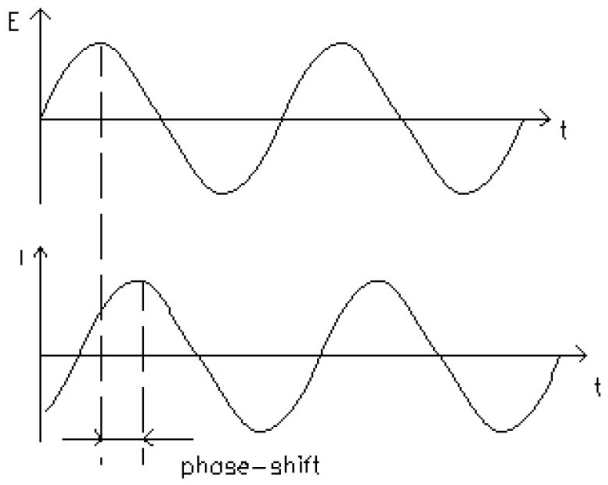

Figure 15. Linear relationship between the potential input and current output [100].

The impedance is measured by applying an AC potential excitation and measuring the current through the electrochemical cell. The excitation signal is expressed as [100]:

$$E = E_0 \cos(\omega t) \tag{23}$$

Where:

E_0= Amplitude of the Signal (m)

ω= Radial Frequency (Hz)

Alternatively, the output current can be expressed in terms of phase shift and radial frequency as follows [100]:

$$I = I_0 \cos(\omega t - \varphi) \tag{24}$$

Where:

I_0= Output Current (A)

φ= Phase Angle (degrees)

Knowing this, Ohm's law may be written to calculate impedance as [100]:

$$Z = \frac{E}{I} = \frac{E_0 \cos(\omega t)}{I_0 \cos(\omega t - \varphi)} = \frac{\cos(\omega t)}{\cos(\omega t - \varphi)} \quad (25)$$

Where:

Z= Impedance (Ω)

One of the most widespread figures related to impedance analysis is the Nyquist plot. In a Nyquist plot, the imaginary part of the impedance is plotted versus the real part at each respective frequency increasing from right to left. On the Nyquist plot the impedance can be represented as a vector of length |*Z*|. The angle between this vector and the X-axis, commonly called the phase angle, φ [102]. A typical Nyquist plot is shown below in Figure 16. Nyquist plots, however, do not have the frequency on them. Another common figure related to EIS is the Bode diagram shown in Figure 16. The Bode diagram can be shown separately or overlayed since it has two different y-axes. The first y-axis plots the log of impedance and the other one plots the phase angle, while the x-axis plots the log of frequency [100].

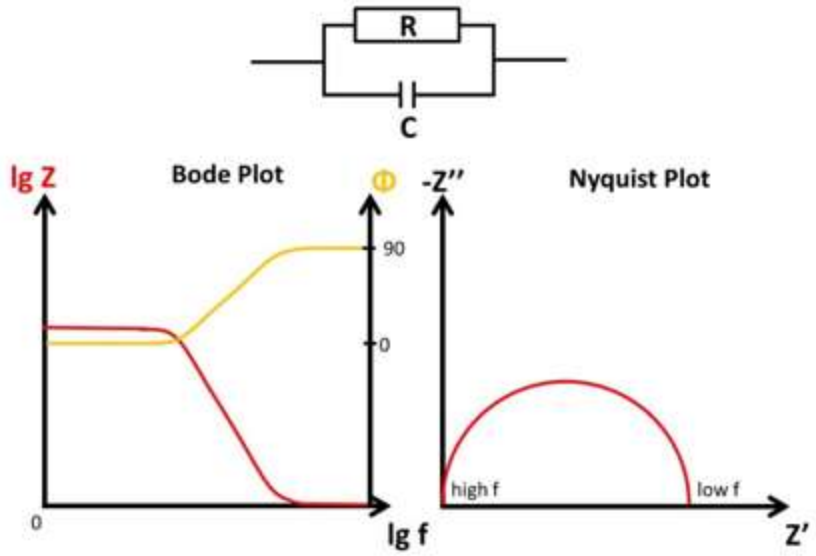

Figure 16. Sample figure of a parallel resistor and capacitor with its corresponding Bode plot and Nyquist plot [103].

EIS data are commonly analyzed by fitting to an equivalent electrical circuit model with elements that correspond to the electrochemical cell. The simplest and most common element is the resistor, which follows Ohm's law as described above. The resistor represents the charge transfer resistance for the electrochemical reaction, which is the most useful parameter obtained from EIS data to determine catalytic performance due to its inverse relationship with current density [103].

Another common element is the capacitor, which stores charge. A simple capacitor is called a plate capacitor, which has two conducting parallel plates in contact with each other. The power source is connected to the plates, and a current flows through the oppositely charged plates until they cannot store anymore charge, exponentially decaying. The current decay over time follows this equation [103]:

$$I = \frac{E^C}{R} e^{\frac{-t}{RC}} = I^0 e^{\frac{-t}{RC}} \quad (26)$$

Where:

E^C= Charging Potential or Voltage (V)

I^0= Starting Current (A)

C= Capacity of the Capacitor (F)

The capacity is the property of the capacitor described as [103]:

$$C = \frac{Q}{E} \quad (27)$$

Where:

Q= Charge (C)

The whole array of charged species and oriented dipoles existing at the electrode-solution interface of a cell is called the electrical double layer. The electrical double layer has been shown to behave as a plate capacitor, and at any given potential, the interface is characterized by a double-layer capacitance. A simple cell with a resistor and capacitor in parallel can be used as a good starting point for many other more complex models, shown in Figure 16. In a circuit with a resistor and capacitor in parallel, the current will always choose the path of lowest impedance, and since the impedance of the capacitor is frequency-dependent, it will change. At high frequencies the impedance of the capacitor will be very low, so the current will flow through it. When frequency is decreased, the impedance of the capacitor will increase causing the current to flow through the resistor. The Nyquist plot for this process is always a semicircle without deviation, as shown in Figure 16. The charge transfer resistance can easily be read from the

Nyquist plot as the real x-axis value (or diameter of the semicircle) at the lower frequency intercept [73, 103].

E. Introduction to Other Experimental Techniques

Characterization of the TSC complexes and post-test analysis of modified electrode surfaces was done using various experimental techniques. Characterization of TSCs employed the use of nuclear magnetic resonance and infrared spectroscopy. After running electrochemical experiments on the modified electrodes, scanning electron microscopy was used in some cases to visually characterize the surfaces. These techniques will be outlined below.

i. Nuclear Magnetic Resonance

Nuclear magnetic resonance (NMR) is a technique that allows observation and measurement of molecular structures of a material by analyzing the interaction of nuclear spins inside of a magnetic field. An NMR spectrum can only be observed for nuclei that possess a net spin. Therefore, hydrogen is well suited for NMR since its most abundant isotope has a spin of ½. However, nitrogen, oxygen, and carbon's most abundant isotopes are not easily visible [104]. Once the external magnetic field is applied to the nuclei then it is possible to have energy transfer between the base energy to a higher energy gap. This transfer corresponds to a radio frequency, that, when the spin returns to its base level is emitted at the same frequency. This signal helps to yield the NMR spectrum for the nuclei [105, 106].

The energy needed to start spinning and create an NMR signal is the difference in energy between the two nuclei orientations and is dependent of the strength of the magnetic field, B_o:

$$\Delta E = \gamma h B_o / 2\pi \tag{28}$$

Where:

ΔE= Difference in Energies of the Two Nuclear Spin Orientations (J)

γ= Magnetogyric Ratio (1/Tesla sec)

h= Planck's Constant (erg sec)

B_o= Strength of Magnetic Field (Tesla)

$\Delta E=h\nu$ and is called the Bohr condition, which enables the frequency of the nuclear transition to be written as the Larmor equation, with $\omega_o=2\pi\nu_o$ called the Larmor resonance frequency [106]:

$$\nu_o = \gamma B_o/2\pi \tag{29}$$

Where:

ν_o= Frequency of Nuclear Transition (MHz)

In practice, one does not put only a single nucleus into a magnetic field, but rather an extremely large one. The distribution of their different energy states is given by the Boltzmann equation [106]:

$$\frac{N_{upper}}{N_{lower}} = e^{-\Delta E/kT} = e^{-h\nu/kT} \tag{30}$$

Where:

N_{upper}= Number of Nuclei in Upper Energy States (dimensionless)

N_{lower}= Number of Nuclei in Lower Energy States (dimensionless)

k= Boltzmann Constant (J/K)

T= Temperature (K)

The actual position of where a peak will occur on a spectrum is different from where it should. This is referred to as chemical shift and is related to the Larmor resonance frequency. There are three main factors that affect chemical shifts and shielding of the nucleus- electronegativity, magnetic anisotropy, and hydrogen bonding [107].

Since the electrons surrounding the nucleus are in constant motion, they generate their own electromagnetic field, which opposes the applied magnetic field. This phenomenon imposes a sort of shield on the nucleus. This shield will define what the chemical shift will be since the magnetic field at the nucleus defines the energy difference between the spin states [107].

Magnetic anisotropy refers to the fact that the Π electrons present in a compound will move and create their own magnetic field when placed in a magnetic field. This field will affect the shielding of the atoms within it. This effect is common for any atoms near a bond with Π electrons [107].

Hydrogen bonding creates deshielding because the bonds are constantly breaking apart and reforming. This dynamic movement creates different strengths that attribute to deshielding. In addition, factors like concentration, temperature, and acidity can affect accurate prediction of chemical shifts for protons involved in hydrogen bonding.

All of these features have a role in the shielding of the nucleus. Depending upon the functional groups of the compound being analyzed, it will have various chemical shift ranges. Some typical ranges of chemical shift for the hydrogen isotope ^{1}H are reported in Figure 17 [107].

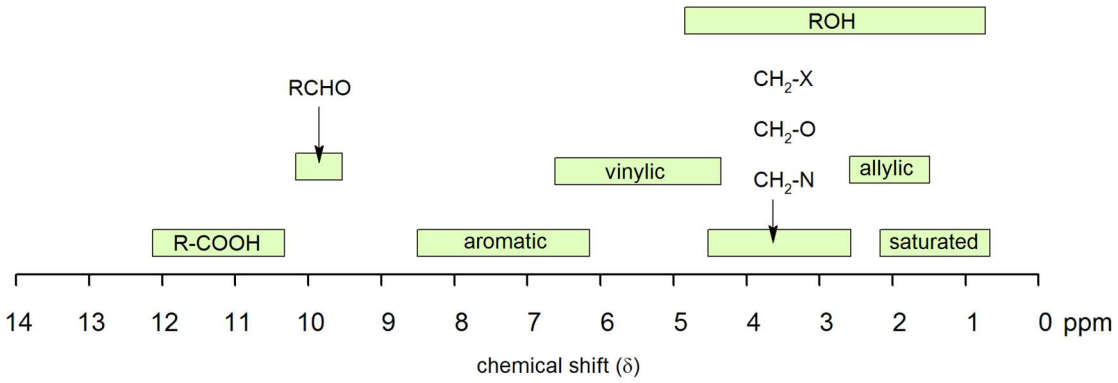

Figure 17. ^{1}H chemical shift ranges for organic compounds [107].

Other than chemical shift, neighboring nuclei can also affect the magnetic field. This effect, called spin-spin coupling or splitting, causes a signal to be split into two or more lines for each type of nucleus present. The size of the splitting is called the coupling constant, *J*, and is independent of the magnetic field and the number of splitting indicates number of chemically bonded nuclei. The various NMR spectral parameters are illustrated in Figure 18 on a basic one-dimensional spectrum [106].

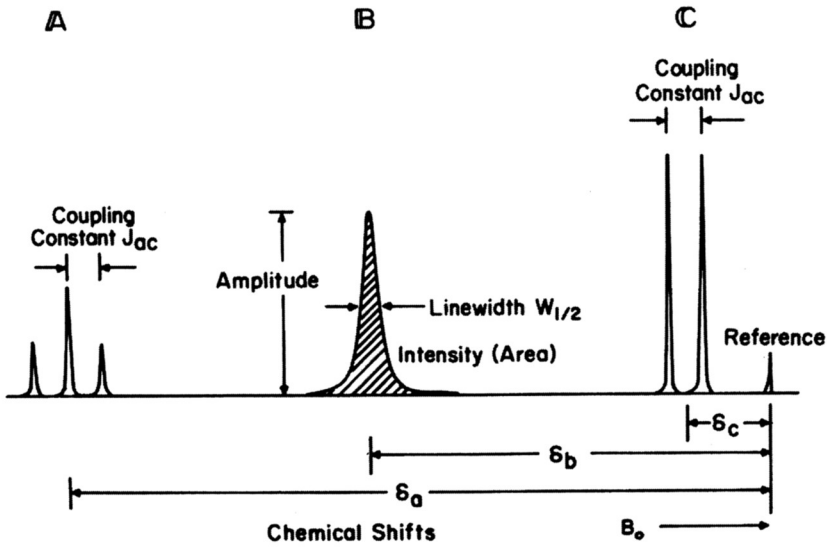

Figure 18. NMR spectral parameters [106].

The peak intensity, or area of an NMR signal, is directly proportional to the number of nuclei that are contributing to the signal. If a concentration on nuclei is known for a specific peak it can be used as a reference. This way, a comparison of peak intensities can be conducted to approximate the signal to noise (S/N) ratio [106].

ii. Infrared Spectroscopy

Infrared Spectroscopy (IR) is a commonly used technique to determine chemical structure of compounds that measures the absorption of infrared radiation by chemical bonds. Functional groups of chemical compounds absorb infrared radiation at known frequencies regardless of what structure the rest of the molecule may have. This correlation of molecules and their absorption frequencies allows the structure of unknown molecules to be identified or confirmed [108]. Molecular vibrational frequencies lie in the IR region of the electromagnetic spectrum, and they can be measured using the IR technique. In IR, light having different frequencies is passed through a sample and the intensity of the transmitted light is measured at each frequency [109].

For a molecule to be IR active it must have a change in dipole moment as a result of vibration upon IR radiation absorption. Dipole moment is a vector quantity that depends upon the photon electric vector and the orientation of the molecule and can be described as an uneven distribution of electron density between atoms. The dipole moment is directly proportional to the IR intensity and can be expressed as [109]:

$$\mu = er \tag{31}$$

Where:

μ= Dipole Moment (Cm)

e= Charge (C)

r= Distance of Separation (m)

It can be difficult to do quantitative analysis of IR; therefore, quantitative analysis is the most common method imposed in IR. To characterize a compound via IR, group frequencies are used to identify a particular functional group. Comparison of vibrational frequency is done with a known IR spectrum to determine the composition of the sample in question. Generally, it is convenient to split the IR spectrum into two regions: the functional group region (4000-1000 cm^{-1}) and the fingerprint region (<1000 cm^{-1}). Most of the useful information to interpret IR data comes from the functional group region due to the fingerprint region being extremely complex. An overview of the typical IR window 4000 to 500 cm^{-1} with various regions of interest highlighted on a spectrum is shown below in Figure 19 [108].

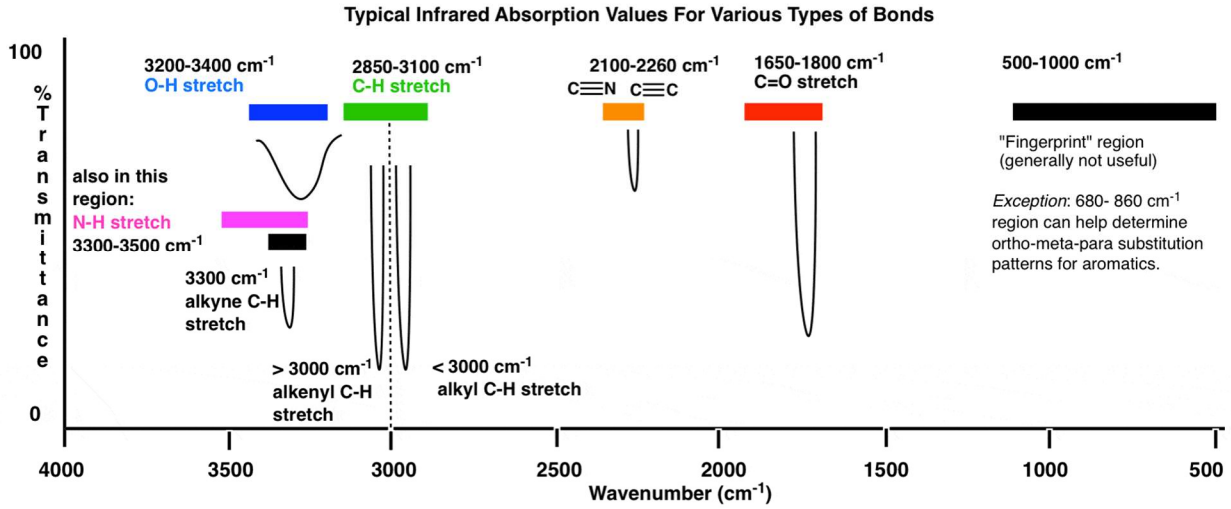

Figure 19. IR spectrum regions of interest [110].

iii. Scanning Electron Microscopy

Scanning electron microscopy (SEM) is one of the most versatile examination tools available to analyze the chemical composition characteristics of the microstructure of a sample by generating images of the surface. The basis of electron microscopy lies in the fundamental principle of light optics. The normal human eye can see a resolution of ~0.1mm, while the common optical microscope has a resolution of ~2,000 Å. The electron microscope, in contrast, has a much higher resolution due to the replacement of the light source with a high energy electron beam. Resolution in a perfect system is described by Abbe's equation [111]:

$$d = 0.612\lambda/m \sin\beta \tag{32}$$

Where:

d= Resolution (length)

λ= Wavelength of Imaging Radiation (Å)

m= Index of Refraction of Medium Between Point Source and Lens, Relative to Free Space (dimensionless)

β= Half the Angle of the Cone of Light from Specimen Plane Accepted by the Objective (Half Aperture Angle in Radians)

m sin β= Numerical Aperture

An optical column is used to focus the electronic beam to magnify the desired focus spot on the surface of a specimen to generate the desired detailed images. The image that an SEM forms depends upon the acquisition of signals produced from the electron beam and specimen

interactions. The images produced by the secondary electrons (SEs) create the topography of the sample and are known as inelastic. These SEs are generated when the original electrons created are ejected after impact with the beam and are detected by the secondary detector. SEs have low energies at less than 50 eV and are sensitive to topography and carry compositional information about the sample; however, they are often caused by backscattered electrons (BSEs) creating incident secondary electrons.

For this reason, elastic backscattered electron data is more beneficial to use for evaluating sample composition since BSE emissions are also affected by the angles of the specimen. BSEs have high energies at thousands of volts, have low energy loss, and great travel depths in comparison to SEs [112]. In addition to the BSEs and SEs that can be used to generate the sample image, other signals are produced when the electron beam strikes the specimen and include characteristic X-rays, X-ray continuum, and Auger electrons. Figure 20 shows the regions where these signals are detected.

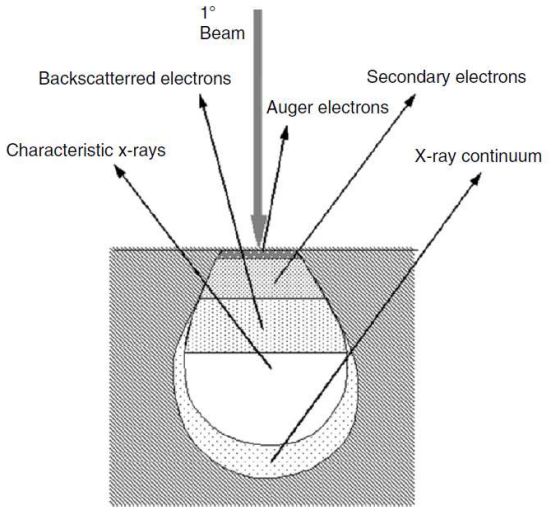

Figure 20. Signals generated by an electronic beam shot at a specimen [32].

III. EXPERIMENTAL

Details of the experiments will be presented below, which will include preparation of catalysts, creation of modified electrodes, electrochemical cell set-up, and electrochemical measurement methods.

A. Catalyst Preparation

The main catalysts used for this project were derived from the TSC ligands and complexes. Synthesis of the catalysts, as well as how to create catalyst inks, are outlined below.

i. TSC Ligand and Complex Synthesis

The chemicals used for all of the completed research came from commercial sources namely Quartzy, VWR International, and Sigma Aldrich. The TSC ligands and their metal derivatives were prepared as previously published in the literature methods by the Grapperhaus/Buchanan Research Group [8, 22, 63, 64, 66, 67, 113-117]. Table 1 shows the list of ligands and metal complexes studied along with abbreviations that will be used to refer to them going forward. Appendix A gives supplemental information provided from the Grapperhaus/Buchanan Research Group about these compounds including chemical structure, IR spectra, NMR spectra, square-wave, and CV studies to confirm their synthesis and potential electrocatalytic capabilities.

Table 1. TSC ligands and complexes compound names with abbreviations.

Compound List	Abbreviation
BTP4A	C1
ATSMpy Single Arm	C2
Ni-ATSMpy Single Arm	C3
Zn-ATSMpy Single Arm	C4
ATSMpy Double Arm	C5
Ni-ATSMpy Double Arm	C6
Zn-ATSMpy Double Arm	C7

ATSM-BTP4A Single Arm	C8
Ni-ATSM BTP4A Double Arm	C9
ATSM-BTP4A Double Arm	C10
Ni-ATSM-BTP4A Single Arm	C11
Ni-ATSM/DMEDA	C12
Ni-ATSM Pyrene	C13
Cu-ATSM/DMEDA	C14
Ni-ATSM	C15

ii. Catalyst Ink Preparation

To create the ink to dropcast onto the electrodes from the catalysts, anywhere from 1-4 mg of TSC was weighed out and then added to 10-40 µL of 10 wt% Nafion solution dispersed in 0.25-1 mL 20% (by volume) ethanol solution. The solution was then vortexed to become properly mixed. Then, the solution was sonicated for at least 30 minutes until a homogenous ink is formed.

B. Electrode Preparation

Electrodes used for study included pencil electrodes, glassy carbon electrodes (GCEs), and carbon paste electrodes (CPEs). Each electrode type and their preparation will be described below. Graphite rod counter electrodes were obtained from Pine Research and Ag/AgCl reference electrodes were obtained from SYC Technologies Inc.

i. Pencil Electrode

Appendix B presents pencil work previously done by the Gupta Research Laboratory in regard to comparison of pencil grades to determine HB as the best choice. That being said, Standard HB grade pencils were obtained from Walmart for this study. To prepare the pencils as disposable electrodes, the unsharpened pencils were broken into smaller pieces, keeping the flat graphite surface on one end, and the other end was sharpened to be used as a connecting lead.

Some pencils were used as is with no cleaning procedure done to them, designated as "Blank". To clean the pencils, they were first sonicated in ethanol and DI water for 15 minutes each. Then, using a Metrohm Autolab PGSTAT 128N potentiostat/galvanostat operating in potentiostatic mode (used for all electrochemical experiments) with the counter electrode and reference electrode leads connected to a graphite rod and the pencil hooked to the working electrode lead, they were electrochemically cycled from -1.2 V to +1.2 V vs. RHE for 20 cycles at 50 mV/sec in 0.5 M H_2SO_4 then rinsed with DI water and dried with a Kimwipe and were designated as "Cleaned". To create a porous surface on the pencil electrodes, some of the pencils were chemically etched with acetone overnight with the goal of removing any soluble organic clays and oil binding materials from the surface and are designated as "Etched". The general etching process can be seen in Figure 21.

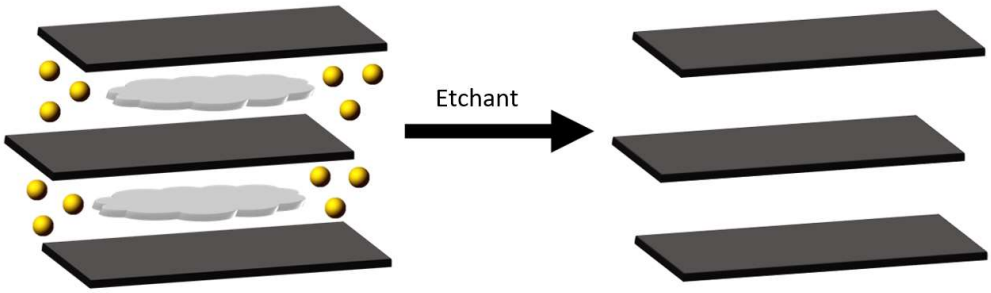

Figure 21. Vacancy generation on pencil electrode.

ii. Glassy Carbon Electrode

Glassy carbon disk electrodes were obtained from Pine Research and were made pristine by a three-step cleaning process. First, the GCEs were sonicated in ethanol and DI water for 15 minutes each. Secondly, they were electrochemically cycled, with the counter electrode and reference electrode leads connected to a graphite rod and the GCE hooked to the working

electrode lead, from 1.2 V to +1.2 V vs. RHE for 20 cycles at 50 mV/sec in 0.5 M H_2SO_4 then rinsed with DI water and dried with a Kimwipe. Finally, the GCE surface was polished using 0.05 μm alumina suspension on a fine-grit polishing pad in a figure-8 motion for at least 20-40 cycles and rinsed with DI water and dried with a Kimwipe.

At this point, the GCEs were checked for cleanliness in a ferricyanide electrochemical cell. They were checked by using 5 mM potassium ferricyanide with 0.1 M potassium nitrate aqueous electrolyte, the Ag/AgCl reference electrode, the graphite rod counter electrode, and the GCEs as the working electrode. Nitrogen was gently bubbled using a glass diffuser into the electrolyte. They were electrochemically cycled from -1.2 V to +1.2 V vs. RHE for 20 cycles at 50 mV/sec to ensure proper shape of curve and that there is not significantly more than ~120 mV separation between the cathodic and anodic peaks.

iii. Carbon Paste Electrode

Carbon paste electrodes (CPEs) were made as previously described in literature [81, 82, 84-86]. Holders were acquired from Bioanalytical systems inc. and cleaned with acetone and ethanol by sonicating for 15 minutes in each. Carbon paste was then made using graphite powder (90 mg), catalyst (10 mg), and paraffin oil (20 μL) as the binding agent in a mortar with pestle. The paste was then transferred to the cleaned holder with weight paper and 1.5 μL 5% Nafion solution was added, and it was left to air dry.

C. Ink Dropcast

Once prepared, the catalyst inks were applied over the pencil with a loading area density of 0.285 mg/cm^2 and left until the ink was dry. In the case of the GCEs, they were first set-up in the rotameter attachment of the potentiostat to rotate the disk and initially set to 50 rpm. Catalyst

inks were then loaded onto the GCEs with a loading area density of 0.285 mg/cm^2 and then the rotameter was ramped to 400 rpm until the ink was dry. Before characterization the rotameter was increased to 1000 rpm. Catalyst was already incorporated into the CPEs.

D. Potentiostat Cell Set-Up

The three-electrode electrochemical cell used for electrochemical characterization (ECC) consisted of the working electrode, the graphite rod counter electrode, and the Ag/AgCl reference electrode (in 3M KCl). A nitrogen purge stream is used to displace any oxygen within the cell, and the electrolyte used in the study is 0.5 M H_2SO_4 (pH of 0.3) electrolyte solution. The pencil electrodes, GCEs, and CPEs were used as the working electrode.

Reductive cycling was done to condition the modified electrodes. ECC methods included linear sweep voltammetry (LSV), cyclic voltammetry (CV), and electrochemical impedance spectroscopy (EIS) executed using Autolab NOVA software. Measured potentials were corrected versus RHE by adding the standard reference potential of Ag/AgCl (0.210 V) and using the Nernst equation. The ECC HER procedure used for analyzing the GCEs and CPEs consisted of a 100-cycle iteration that was repeated 10 times to accurately measure the activity of the electrodes. This cycle comprised of a CV potential sweep versus RHE from 0 V to -0.8 V at 50 mV/s, followed by an EIS carried out at -300 mV from 100,000 Hz to 0.02 Hz. A slow LSV was then run from 0 V to -0.8 V at 1 mV/s, after which a fast LSV from -0.8 V to 0 V at 50 mV/s was done. The pencil electrodes, up until the samples with C15, were ran using a short ECC HER procedure with an LSV potential sweep from 0 V to -1 V at 10 mV/s, followed by a CV from 0 V to -1 V at 50 mV/s, then a second LSV from 0 V to -0.8 V at 10 mV/s, and then an EIS was carried out at -600 mV from 100,000 Hz to 0.1 Hz. The pencils with C15 catalyst were ran using the same conditions as described above for GCEs and CPEs.

First, to determine which of the TSC ligands and complexes were the most electrochemically active, their HER performance was evaluated and compared on GCEs. Promising TSCs were then tested on CPEs, and their performance was analyzed. Finally, pencil electrodes were evaluated for how to best prepare them and then tested with a new TSC complex, as well as a known high-performing TSC previously studied by the Gupta Research Laboratory [22], whose summary of electrocatalytic activity can be found in Appendix C. Table 2 outlines the generated sample list including catalyst present and electrode type.

Table 2. Sample names with catalyst present and electrode type.

Sample Name	Catalyst	Electrode
GCE Blank	N/A	GCE
GCE-C1	C1	GCE
GCE-C2	C2	GCE
GCE-C3	C3	GCE
GCE-C4	C4	GCE
GCE-C5	C5	GCE
GCE-C6	C6	GCE
GCE-C7	C7	GCE
GCE-C8	C8	GCE
GCE-C9	C9	GCE
GCE-C10	C10	GCE
GCE-C11	C11	GCE
GCE-C12 Nafion	C12	GCE
GCE-C12 No Nafion	C12	GCE
GCE-C12 Nafion on Top	C12	GCE
GCE-C13	C13	GCE
GCE-C14	C14	GCE
CPE Blank	N/A	CPE
CPE-C3	C3	CPE
CPE-C6	C6	CPE
CPE-C12	C12	CPE
CPE-C13	C13	CPE
Blank Pencil 1	N/A	Pencil
Blank Pencil 2	N/A	Pencil
Cleaned Pencil 1	N/A	Pencil
Cleaned Pencil 2	N/A	Pencil
Etched Pencil 1	N/A	Pencil

Etched Pencil 2	N/A	Pencil
Etched Pencil 3	N/A	Pencil
Etched Pencil 1-C3	C3	Pencil
Etched Pencil 2-C3	C3	Pencil
Etched Pencil 3-C3	C3	Pencil
Blank Pencil-C15	C15	Pencil
Blank Pencil Redo-C15	C15	Pencil
Etched Pencil-C15	C15	Pencil
Etched Pencil Redo-C15	C15	Pencil

IV. RESULTS AND DISCUSSION

Results of the studies performed will be presented here, including polarization curves, Nyquist plots with charge transfer resistances, and Tafel slopes to help evaluate catalytic efficiency. The evaluation of which of the TSC ligands and complexes were the most electrochemically active, by comparison of their HER performance on GCEs, is presented first. Secondly, promising TSCs tested on CPEs are analyzed. Lastly, standard pencil electrodes were evaluated for best cleaning practices and then tested with one of the new TSC complexes, as well as with a known high-performing TSC previously studied by the group, namely C15. Discussion will then be presented to further analyze and interpret the data.

A. GCE TSC Results

The modified electrodes in the sample set were conditioned by reductive cycling as outlined above. For the GCE Blank, the overpotential at its peak of 300 cycles was 0.664 V. GCE-C1, GCE-C2, GCE-C4, GCE-C9, GCE-C10, and GCE-C11 did not reach to give potential values at 10 mA/cm^2. Additionally, the C7 complex was found not to be soluble in the ethanol solution to make the ink and was therefore not used in the study.

GCE-C3 before conditioning gave an overpotential value of 0.557 V, but at its peak at 400 cycles gave overpotential of 0.515 V, as shown in Figure 22, where it is compared to its polarization curve after extended reductive cycling to show stability (0.522 V at 1000 cycles). Figure 23 compares the GCE-C3 metal complex to its ligand parent GCE-C2, as well as to the GCE Blank. The GCE-C2 did not give potential at 10 mA/cm^2, and the metal GCE-C3 overpotential decreases compared to the GCE Blank from 0.664 V to 0.515 V. This shift in overpotential represents improvement in catalytic efficiency for the metal C3 complex showed promising result and was further analyzed using Tafel slope.

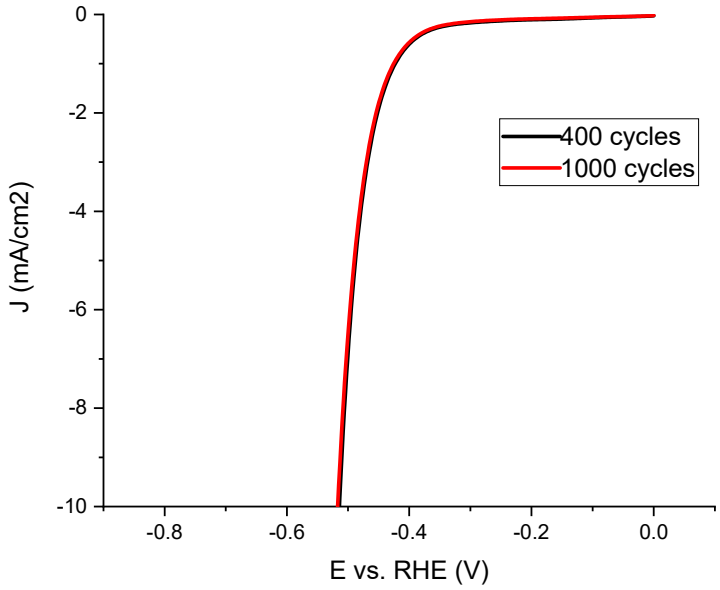

Figure 22. GCE-C3 catalyst polarization curves for peak and 1000 cycles.

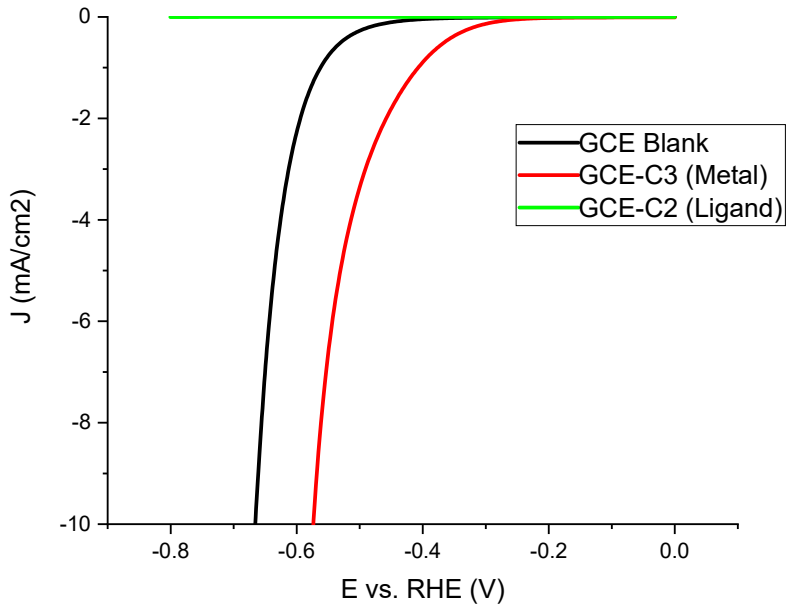

Figure 23. Comparison of GCE blank, GCE-3 metal, and GCE-2 ligand polarization curves at 400 cycles.

The Tafel slope for GCE-C3 initially was 45 mV/dec, and at its peak at 400 cycles was 139 mV/dec, and after extended conditioning was 125 mV/dec, shown in Figure 24. This is a drastic change in Tafel slope which does suggest change in HER mechanism, with the higher Tafel slopes having proton adsorption as the limiting step. Figure 25 reports the Nyquist plots for GCE-C3 at its peak at 400 cycles and after extensive reductive cycling. Charge transfer resistance for GCE-3 was ~9000 Ω initially, ~1500 Ω at peak, and ~3000 Ω after reductive cycling. The charge-transfer kinetics between the film and electrode attributed to a reorganization of the active sites show improved contact between the electrode and solution after cycling, although the resistance did increase after an extensive period.

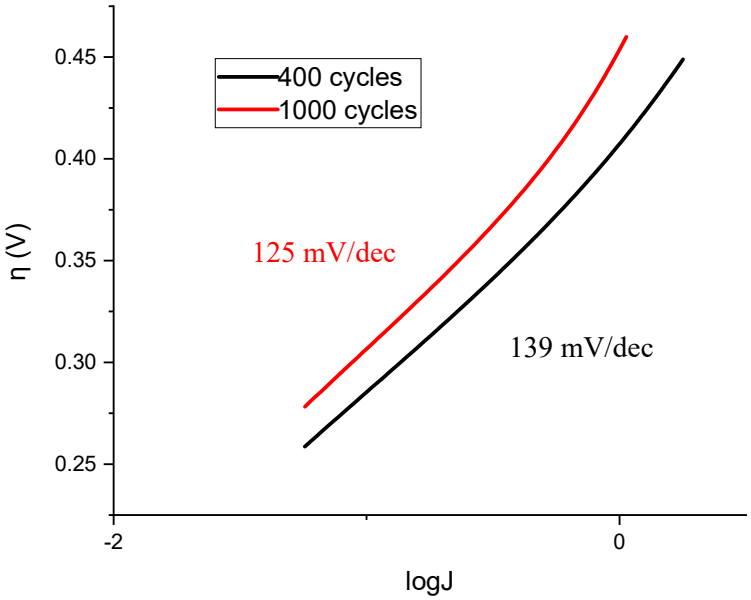

Figure 24. Tafel slopes for GCE-C3 at peak and after 1000 cycles.

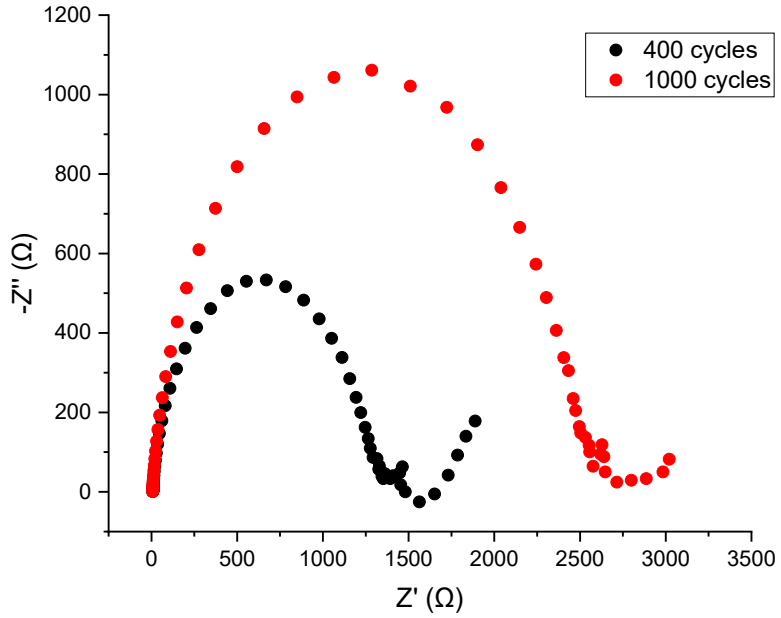

Figure 25. Nyquist plots for GCE-C3 at peak and after 1000 cycles.

GCE-C5 before conditioning gave an overpotential value at its peak at 700 cycles of 0.706 V, as shown in Figure 26, where it is compared to its polarization curve after extended reductive cycling to show stability (0.713 V at 1000 cycles). This GCE-C5 ligand has a higher overpotential compared to the GCE Blank at peak of 0.664 V. The metal complex of this ligand, GCE-C6, gave overpotential of 0.706 V initially and decreased significantly to 0.519 V at its peak at 300 cycles. Figure 27 shows polarization curves for GCE-C6 at its peak and after extended reductive cycling to show stability (0.550 V at 1000 cycles). Figure 28 compares the GCE-C6 metal complex to its ligand parent GCE-C5, as well as to the GCE Blank. The GCE-C5 gave overpotential of 0.706 V, and the metal GCE-C6 overpotential decreases compared to the GCE Blank from 0.664 V to 0.519 V. This shift in overpotential represents improvement in catalytic efficiency for the metal C6 complex showed promising result and was further analyzed using Tafel slope.

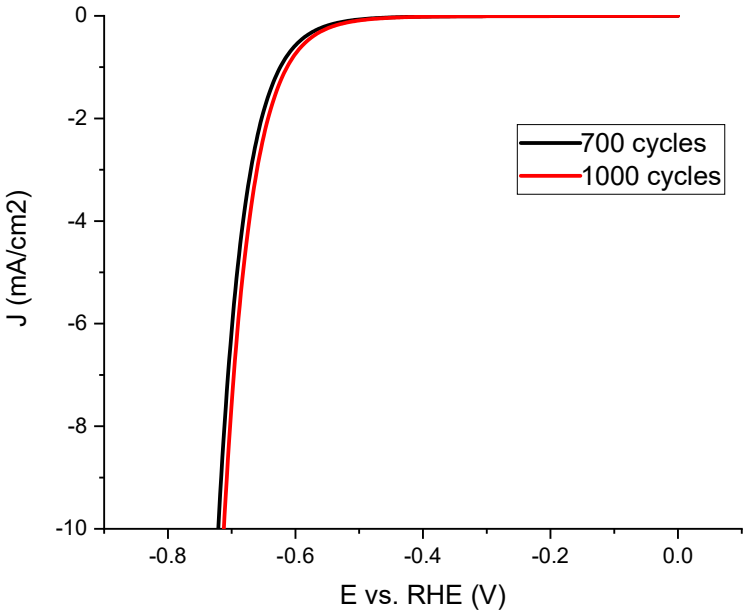

Figure 26. GCE-C5 catalyst polarization curves for peak and 1000 cycles.

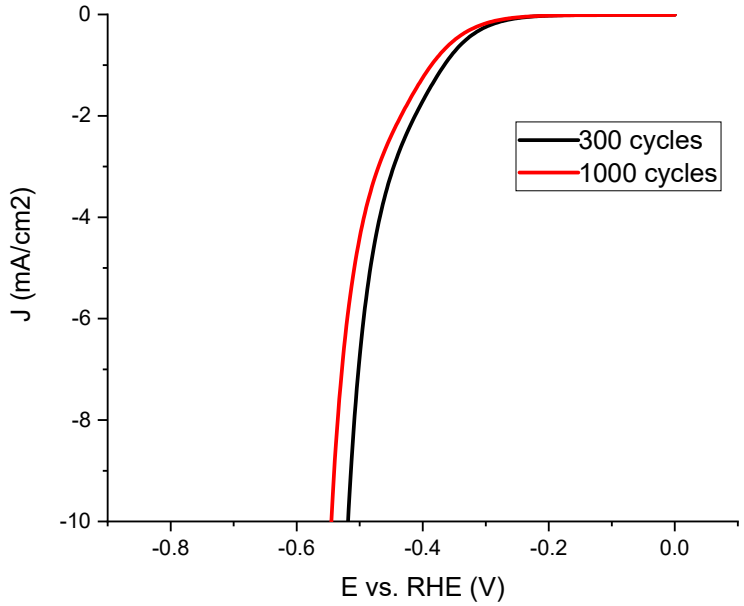

Figure 27. GCE-C6 catalyst polarization curves for peak and 1000 cycles.

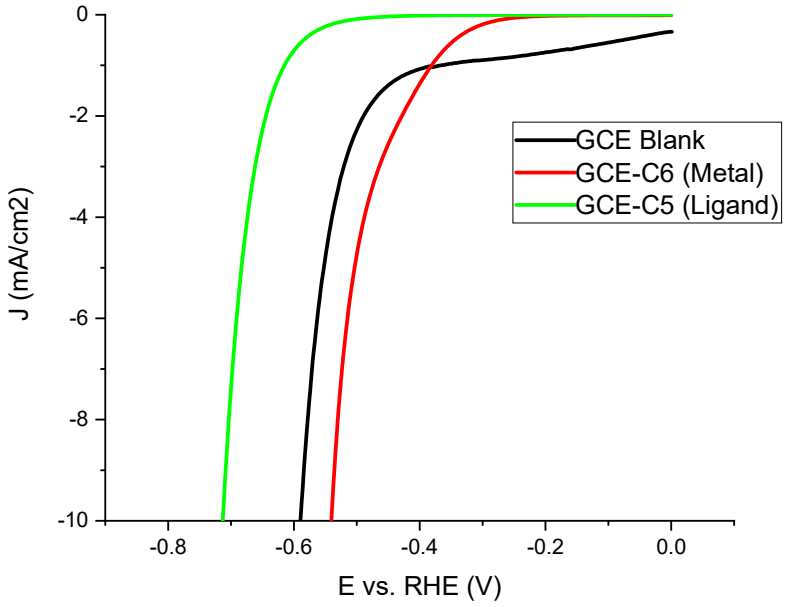

Figure 28. Comparison of GCE blank, GCE-6 metal, and GCE-5 ligand polarization curves at 400 cycles.

The Tafel slope for GCE-C6 initially was 59 mV/dec, and at its peak at 300 cycles was 116 mV/dec, and after extended conditioning was 117 mV/dec, shown in Figure 29. This is a drastic change in Tafel slope which does suggest change in HER mechanism, with the higher Tafel slopes having proton adsorption as the limiting step. Lower Tafel slopes indicate improved electron transfer. Figure 30 reports the Nyquist plots for GCE-C6 at its peak at 300 cycles and after extensive reductive cycling. Charge transfer resistance for GCE-6 was ~21000 Ω initially, ~550 Ω at peak, and ~1000 Ω after reductive cycling. The charge-transfer kinetics between the film and electrode attributed to a reorganization of the active sites show improved contact between the electrode and solution after cycling, although the resistance did increase after an extensive period.

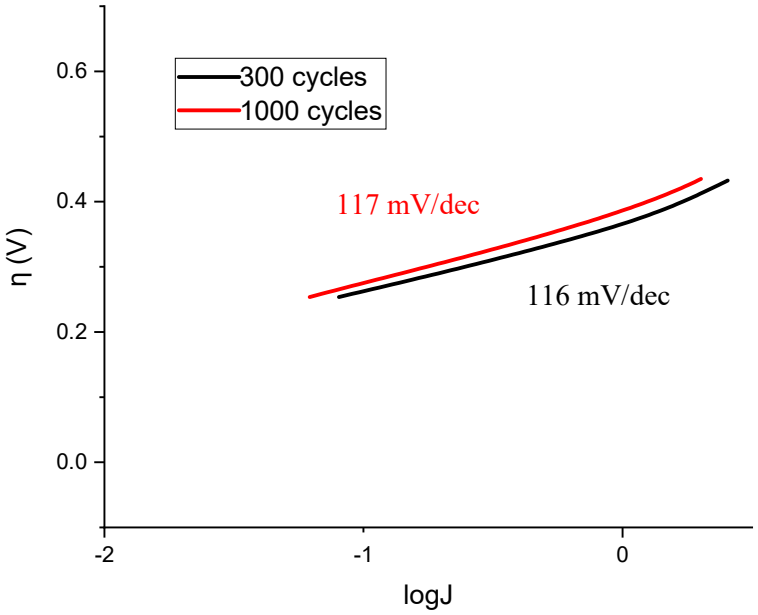

Figure 29. Tafel slopes for GCE-C6 at peak and after 1000 cycles.

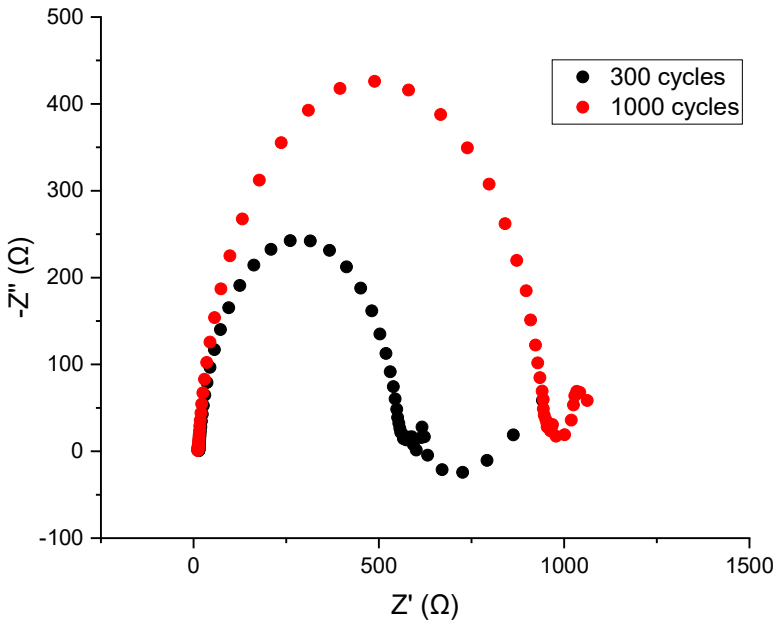

Figure 30. Nyquist plots for GCE-C6 at peak and after 1000 cycles.

GCE-C8 gave an overpotential value at its peak at 700 cycles of 0.788 V, as shown in Figure 31, where it is compared to its polarization curve after extended reductive cycling to show stability. This GCE-C8 ligand has a higher overpotential compared to the GCE Blank at peak of 0.664 V. The metal complex of this ligand, GCE-C9, gave potential at 10 mA/cm^2, as mentioned above.

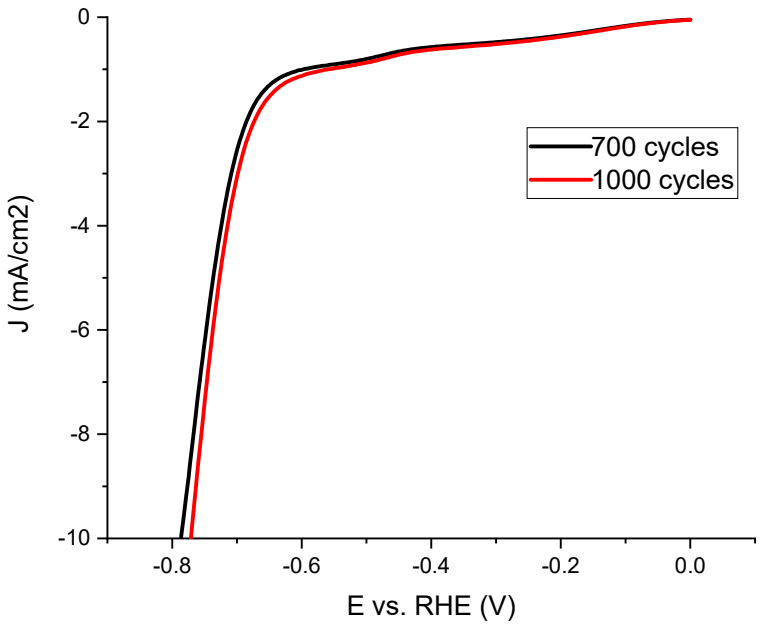

Figure 31. GCE-C8 catalyst polarization curves for peak and 1000 cycles.

GCE-C12 was first prepared in the traditional way with Nafion inside of the catalyst ink; however, this gave only initial overpotential of 0.740 V that did not give any voltage signal after 100 cycles. It was then proposed to try the catalyst without Nafion included, which again gave similar overpotential of 0.731 V that did not give any voltage signal after 100 cycles. Then, the catalyst was prepared using Nafion dropped on top of the ink instead of inside of it, which gave a drastic overpotential decrease from initially 0.736 V to, at its peak of 300 cycles, 0.470 V. After extended reductive cycling (in this case only ran until 500 cycles) the sample gave the same overpotential of 0.470 V, which shows stability. The fact that the C12 performed best with the Nafion on top, rather than inside of it, was believed to be due to the fact that the complex was dissociating into solution when the Nafion was include. Nafion in general is needed for the ink because it is a proton conductor with excellent thermal and mechanical stability. Figure 32 shows

GCE-C12 at its peak compared to the polarization curve of the GCE blank. This shift in overpotential represents great improvement in catalytic efficiency for the metal C12 complex showed promising result and was further analyzed using Tafel slope.

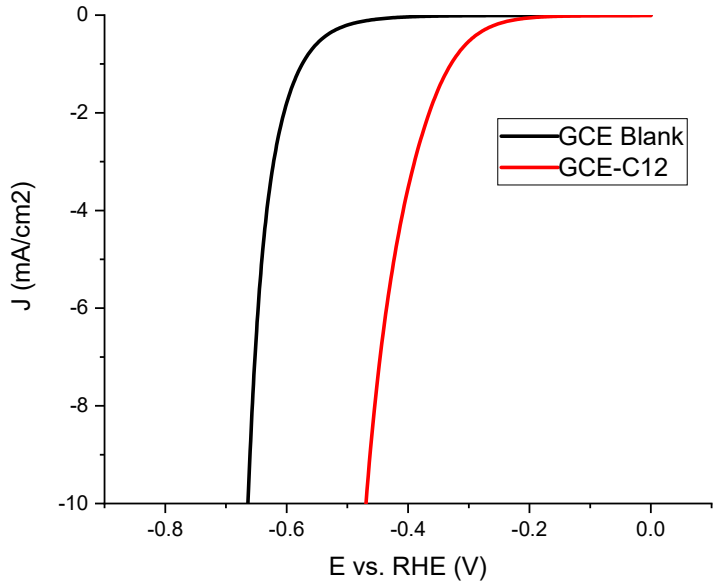

Figure 32. GCE Blank compared to GCE-C12 catalyst with Nafion on top polarization curves at peak.

The Tafel slope for GCE-C12 initially was 87 mV/dec, and at its peak at 300 cycles was 108 mV/dec, and after extended conditioning was 105 mV/dec, as shown in Figure 33. This is not a drastic change in Tafel slope, which suggests that the HER mechanism remained in the mixed mechanism region, with the higher Tafel slopes having proton adsorption as the limiting step. Lower Tafel slopes indicate improved electron transfer. Figure 34 reports the Nyquist plots for GCE-C12 at its peak at 300 cycles and after extensive reductive cycling. In this case, there is a decrease in the magnitude of both imaginary and real component in the EIS which were low to

begin with, suggesting increased catalytic activity, unlike the previous samples. Charge transfer resistance for GCE-12 was ~4500 Ω initially, ~350 Ω at peak, and ~250 Ω after reductive cycling. This decrease indicates charge-transfer kinetics between the film and electrode attributed to a reorganization of the active sites to improve contact between the electrode and solution.

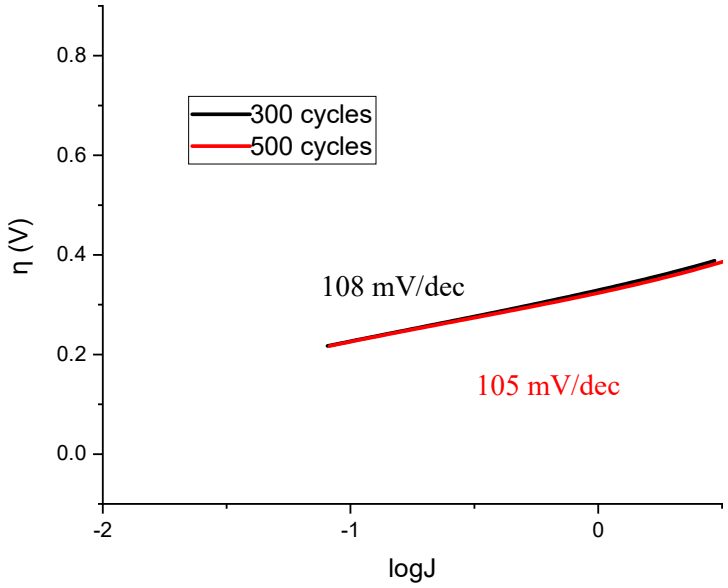

Figure 33. Tafel slopes for GCE-C12 with Nafion on top at peak and after 500 cycles.

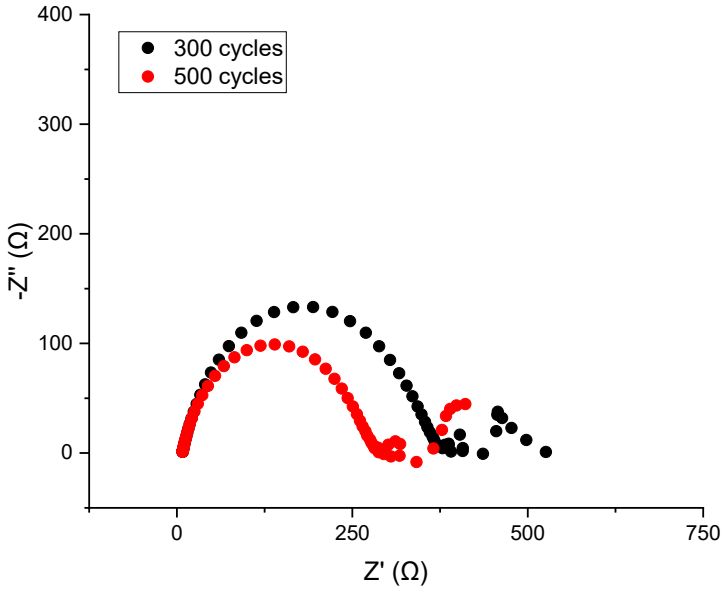

Figure 34. Nyquist plots for GCE-C12 at peak and after 500 cycles.

GCE-C13 was tried in the same manner as GCE-C12 with Nafion, without Nafion, and with Nafion on top. The run with Nafion did not give any potential at 10 mA/cm^2, without Nafion gave an overpotential value at its peak at 400 cycles of 0.736 V, and with Nafion on top gave an overpotential value at its peak at 200 cycles of 0.763 V. As shown in Figure 35, none of the GCE-C13s gave lower overpotentials compared to the GCE Blank at 0.664 V.

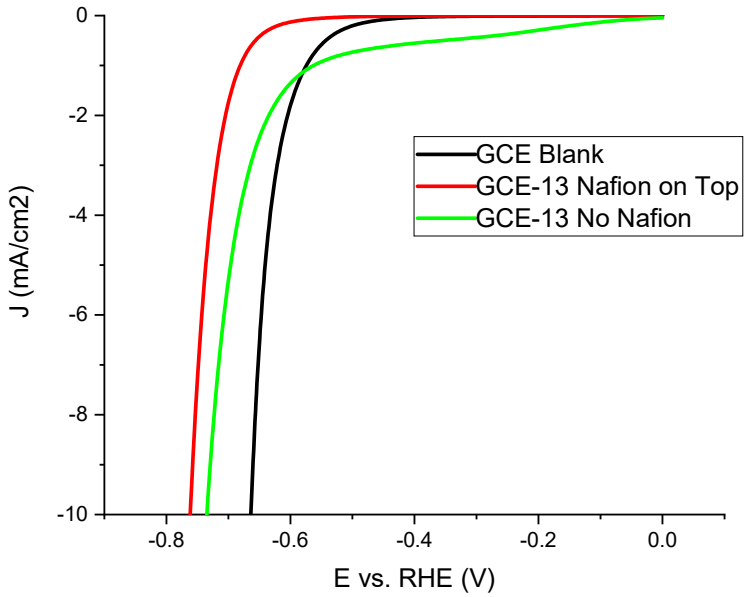

Figure 35. GCE-C13 catalyst with Nafion on top and without compared to GCE blank polarization curves for peak cycles.

Overall, on the GCEs the promising TSC metal complexes were C3, C6, and C12 with Nafion on top, which all reported low overpotentials and high stability. Their overpotentials at peak activity are reported in Table 3, along with their Tafel slopes. GCE-C12 with Nafion on top was the only complex to show decreased resistance with increased cycling. These complexes were then transitioned to be tested with the carbon paste electrodes to increase surface area, and the results of those tests are outlined below.

Table 3. Overpotentials and Tafel slopes for promising TSC complexes on glassy carbon electrodes.

Sample Name	**Overpotential Prior to Cycling (V)**	**Overpotential at Peak (V)**	**Overpotential after Extensive Cycling (V)**	**Tafel Slope (mV/dec)**
GCE-C3	0.557	0.515	0.522	139
GCE-C6	0.706	0.519	0.550	116
GCE-C12 Nafion on Top	0.736	0.470	0.470	108

B. CPE TSC Results

The C3, C6, and C12 complexes were transitioned to be reductively cycled with the CPEs to increase surface area, and the results of those tests are outlined below. A blank CPE was run first for reference, and its overpotential at its peak at 500 cycles was 0.629 V.

CPE-C3 before conditioning gave an overpotential value of 0.719 V, but at its peak at 1000 cycles gave overpotential of 0.454 V. Figure 36 shows a comparison between the CPE and the GCE for this catalyst and their blanks, with CPE-C3's overpotential being smaller compared to the GCE-C3, 0.454 V versus 0.515 V. This dramatic shift in overpotential represents improvement in catalytic efficiency for the metal C3 complex showed promising result and was further analyzed using Tafel slope.

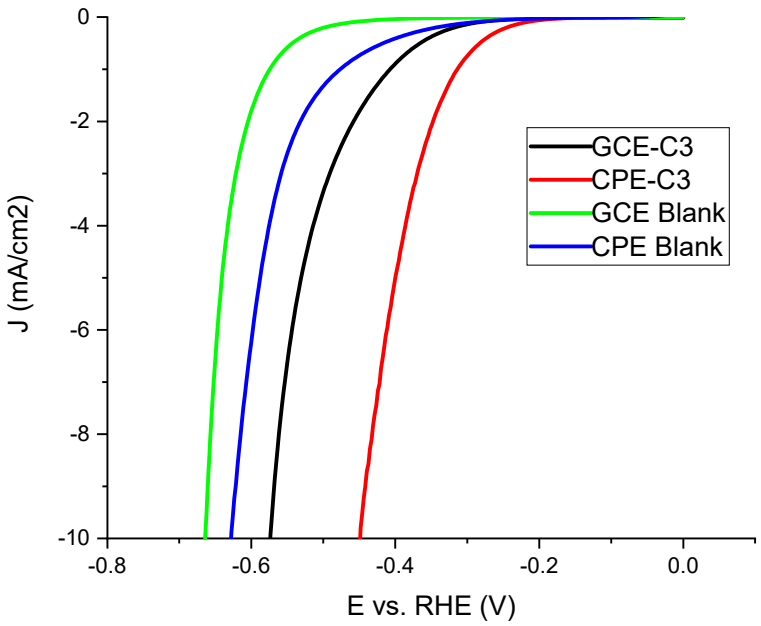

Figure 36. GCE-C3, CPE-C3, GCE blank, and CPE blank polarization curves compared at their cycling point of peak activity.

The Tafel slope for CPE-C3 initially was 211 mV/dec, and at its peak at 1000 cycles was 133 mV/dec. Figure 37 shows CPE-C3 at its peak at 1000 cycles compared to GCE-C3 (125 mV/dec), GCE Blank (113 mV/dec), and CPE Blank (125 mV/dec). This is change in Tafel slope which does suggest change in HER mechanism, with the higher Tafel slopes having proton adsorption as the limiting step. Figure 38 reports the Nyquist plots for CPE-C3 at its peak at 1000 cycles compared to GCE-C3, GCE Blank, and CPE Blank. For the electrodes with catalyst, the resistance values are much lower in magnitude of both imaginary and real component in the EIS than blanks, suggesting increased catalytic activity. Charge transfer resistance for GCE-C3 was ~9000 Ω initially, ~1500 Ω at peak, and ~2000 Ω after reductive cycling. Charge transfer resistance for CPE-C3 was ~35000 Ω initially, ~2750 Ω at peak after reductive cycling. Charge

transfer resistance for GCE Blank was ~13000 Ω initially, ~20000 Ω at peak, and ~40000 Ω after reductive cycling. Charge transfer resistance for CPE Blank was ~220000 Ω initially, ~25000 Ω at peak, and ~14000 Ω after reductive cycling. This decrease indicates charge-transfer kinetics between the film and electrode attributed to a reorganization of the active sites to improve contact between the electrode and solution.

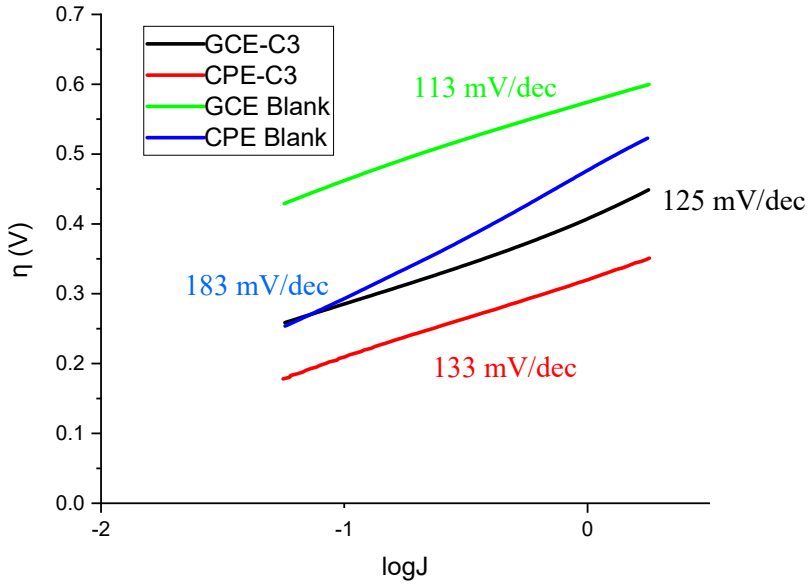

Figure 37. Tafel slopes for GCE-C3, CPE-C3, GCE blank, and CPE blanks compared at their point of peak activity.

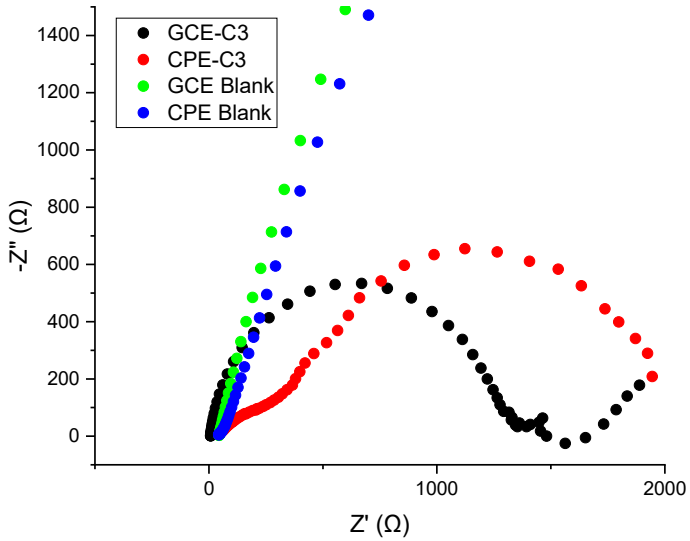

Figure 38. Nyquist plots for GCE-C3, CPE-C3, GCE blank, and CPE blanks compared at their point of peak activity.

CPE-C6 gave an overpotential value at its peak at 300 cycles of 0.678 V, as shown in Figure 39, where it is compared to its polarization curve after extended reductive cycling to show stability. This CPE-C6 has similar overpotential compared to the CPE and GCE Blanks, with overpotentials at peak of 0.629 V and 0.664 V, respectively. Also, the GCE with this complex gave better overpotential at its peak, 0.519 V. These comparisons are outlined in Figure 40.

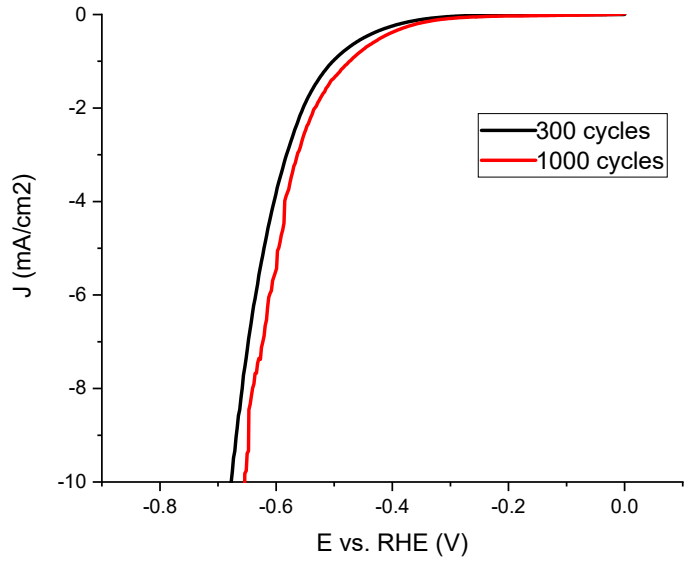

Figure 39. CPE-C6 catalyst polarization curves for peak and 1000 cycles.

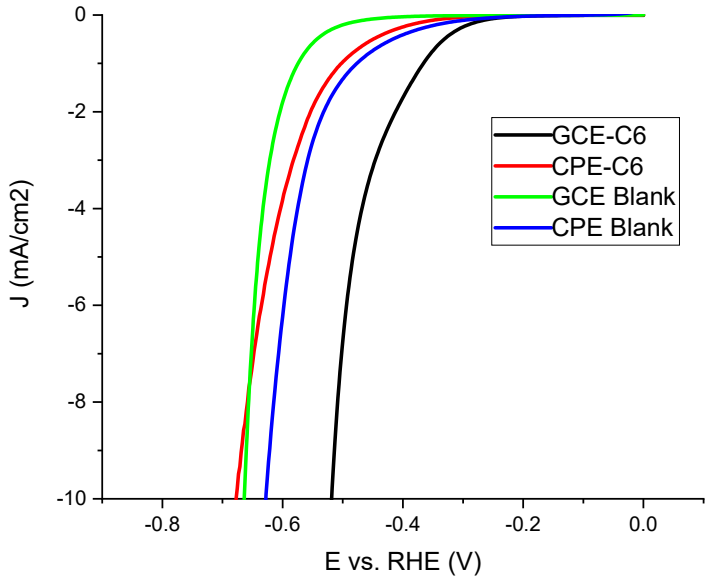

Figure 40. GCE-C6, CPE-6, GCE blank, and CPE blank polarization curves compared at their cycling point of peak activity.

CPE-C12 did not have any activity at 10 mA/cm^2, so the C13 complex was tested in its place to see if it could have improved activity with incorporation into the carbon paste. CPE-C13 gave an overpotential value at its peak at 200 cycles of 0.749 V, as shown in Figure 41, where it is compared to its polarization curve after extended reductive cycling to show stability. In addition, the GCE-C13 at its peak at 400 cycles gave overpotential of 0.736 V. Figure 42 shows that neither the CPE-C13 or the GCE-C13 had lower overpotential compared to the CPE and GCE Blanks, with overpotentials at peak of 0.629 V and 0.664 V, respectively.

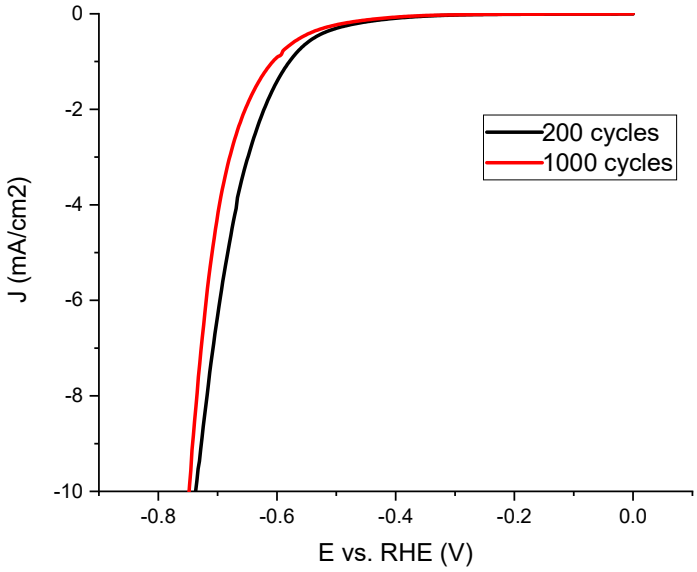

Figure 41. CPE-C13 catalyst polarization curves for peak and 1000 cycles.

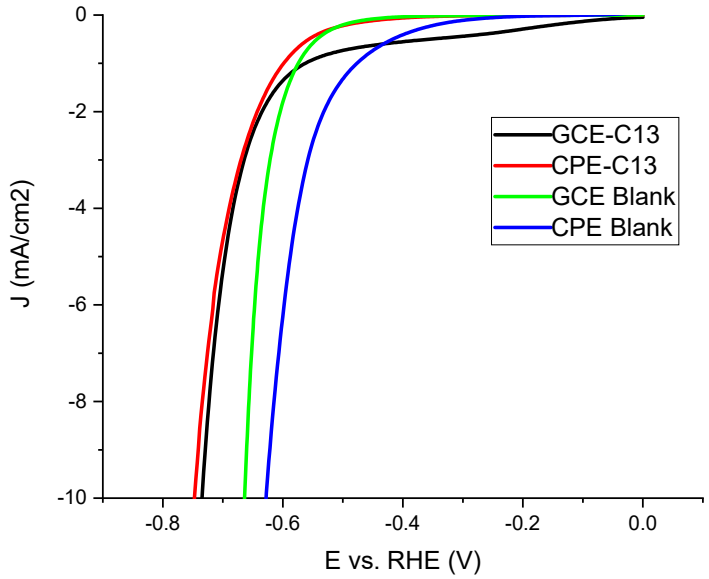

Figure 42. GCE-C13, CPE-13, GCE blank, and CPE blank polarization curves compared at their cycling point of peak activity.

Overall, on the CPE with the promising TSC metal complexes was C3, which reported low overpotentials and high stability. CPE-C3 overpotential and Tafel slope at peak activity are reported in Table 4, along with those of the three promising GCEs. Since the C3 complex best performed on the carbon paste electrode, it was transitioned to be tested with the standard pencil electrodes for another attempt to increase surface area, and the results of those tests are outlined below.

Table 4. Overpotentials and Tafel slopes for promising TSC complexes on carbon paste and glassy carbon electrodes.

Sample Name	Overpotential Prior to Cycling (V)	Overpotential at Peak (V)	Overpotential after Extensive Cycling (V)	Tafel Slope (mV/dec)
GCE-C3	0.557	0.515	0.522	139
GCE-C6	0.706	0.519	0.550	116
GCE-C12 Nafion on Top	0.736	0.470	0.470	108
CPE-C3	0.719	0.454	0.454	133

C. Pencil Electrode TSC Results

Pencil electrodes were evaluated for how to best prepare them and then were tested with a new TSC complex, C3, as well as a known high-performing TSC previously studied by the Gupta Research Laboratory, C15. The cleaning study and C3 catalyst were studied first using the short ECC HER procedure, followed by the C15 catalyst being studied using reductive cycling.

Pencils using three different preparation methods were compared for 2 different pencils. Some pencils were used as is with no cleaning procedure done to them, designated as “Blank”. Some pencils were sonicated and electrochemically cleaned and are designated as “Cleaned”. Some pencils were chemically etched with acetone overnight are designated as “Etched”. The polarization curves of the first pencil studied to compare the three cleaning methods are found in Figure 43. The polarization curves of the second pencil studied to compare the three cleaning

methods are found in Figure 44. In both cases, the blank pencil had the worst electrochemical activity, the etched pencil had the best activity, and the cleaned pencil fell in the middle. These results can be further confirmed visually through SEM images taken of an etched pencil and an unetched pencil shown in Figure 45. Knowing this, etched pencils were prepared with catalyst going forward.

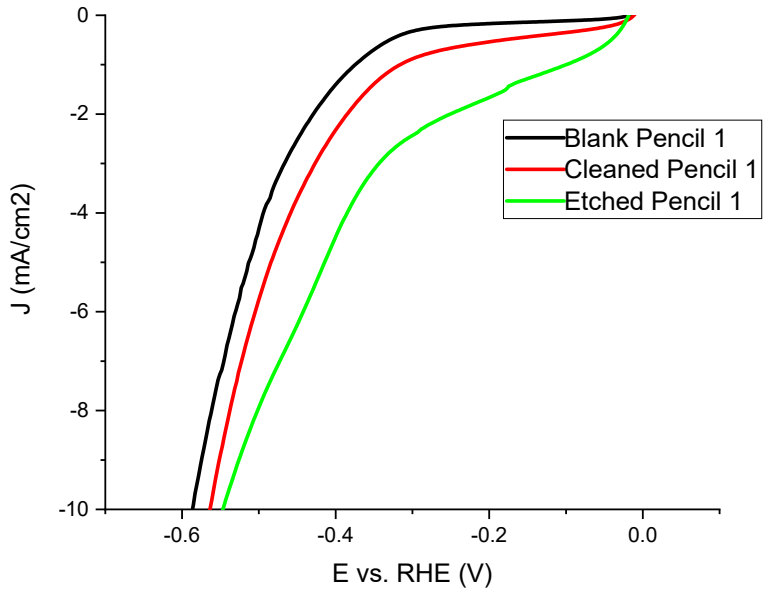

Figure 43. Blank, clean, and etched pencil 1 polarization curves compared.

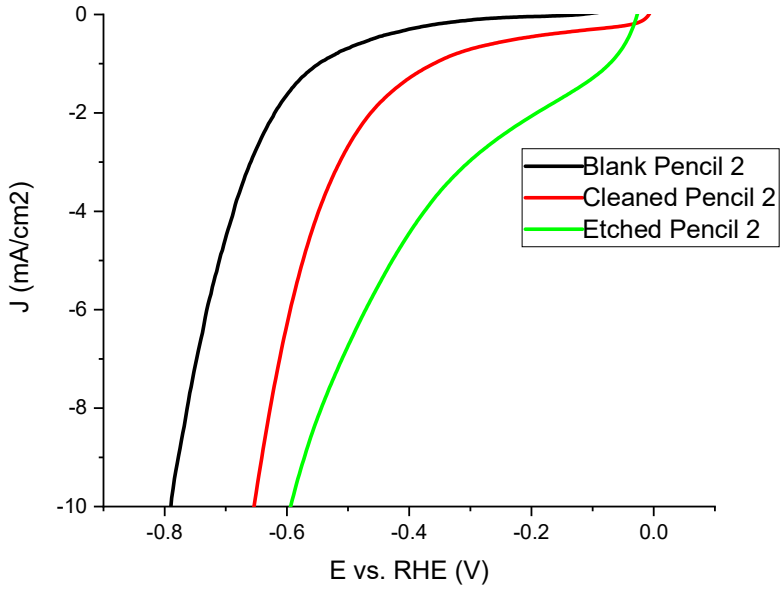

Figure 44. Blank, clean, and etched pencil 2 polarization curves compared.

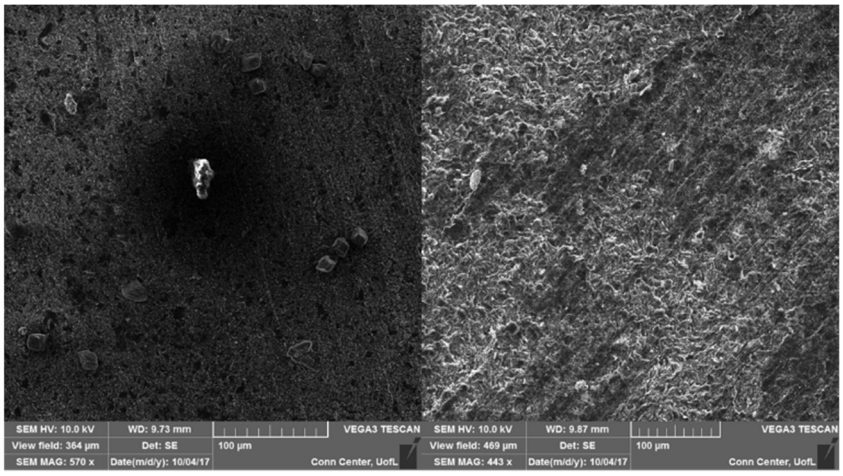

Figure 45. SEM images of an HB pencil before (left) and after (right) etching on a 100 µm scale.

Three etched pencils were prepared with and without the C3 catalyst and were analyzed for catalytic potential. Figure 46, 47, and 48 compares the polarization curves for the etched pencils to the etched pencils with the C3 catalyst added. The Etched Pencils gave overpotentials

of 0.548 V, 0.596 V, and 0.642 V, respectively. The Etched Pencils with C3 gave overpotentials of 0.530 V, 0.579 V, and 0.594 V, respectively. These potentials exhibit the variability from pencil to pencil, but in each case are very similar with the pencils with the catalyst having slightly smaller overpotential values. The overpotentials are higher than the GCE-C3 and CPE-C3 at peak activity, with CPE-C3 having overpotential of 0.482 V, and GCE-C3 having overpotential of 0.515 V as shown in Figure 49.

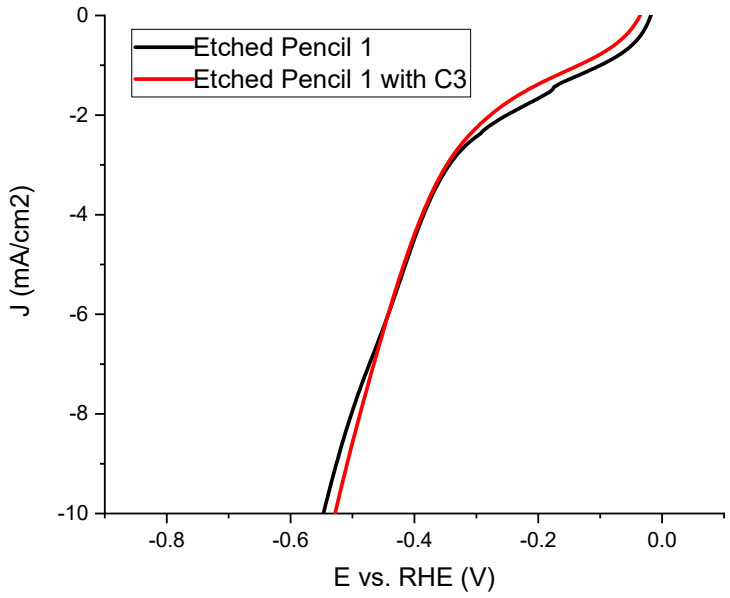

Figure 46. Etched pencil 1 with and without C3 catalyst polarization curves compared.

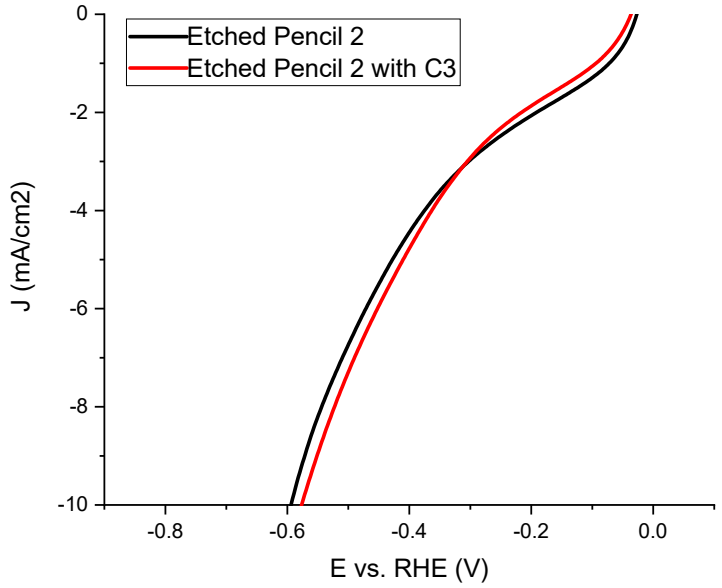

Figure 47. Etched pencil 2 with and without C3 catalyst polarization curves compared.

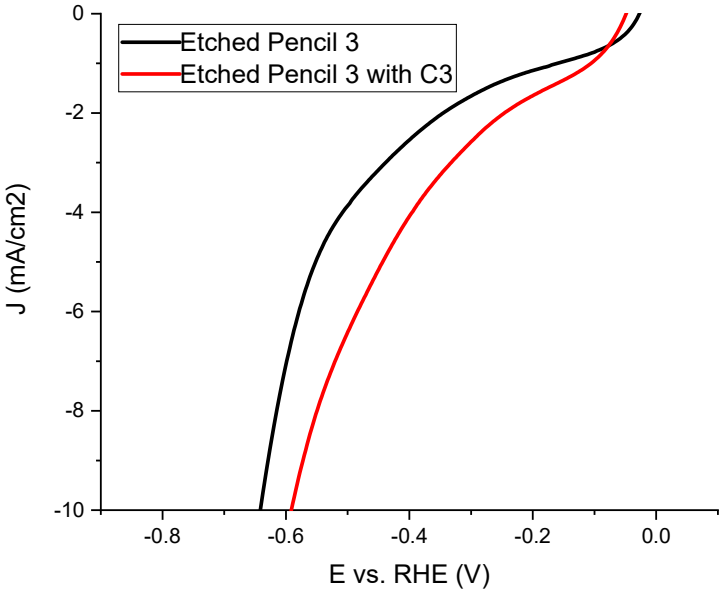

Figure 48. Etched pencil 3 with and without C3 catalyst polarization curves compared.

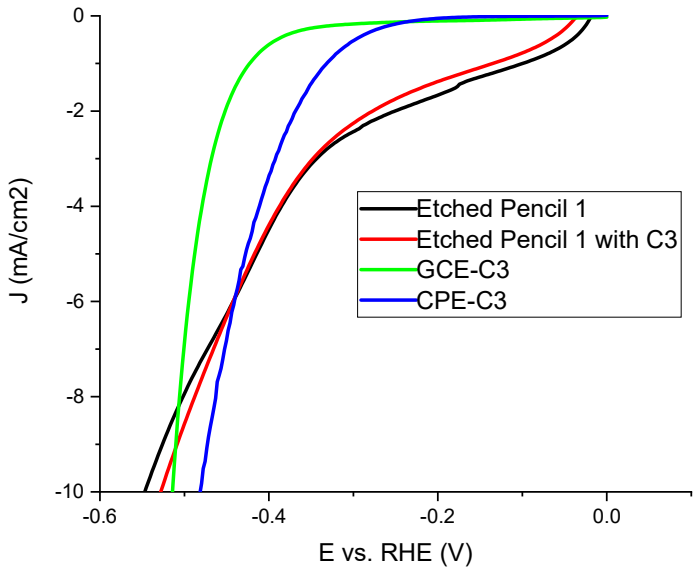

Figure 49. Etched pencil 1 with and without C3 compared to GCE-C3 and CPE-C3 polarization curves.

The Tafel slopes, however, as shown in Figure 50, are not comparable to the GCE or CPE with such high values, with GCE-C3 and CPE-C3 having values of 139 mV/dec and 105 mV/dec, while Etched Pencil and Etched Pencil with C3 had slopes of 453 mV/dec and 216 mV/dec.

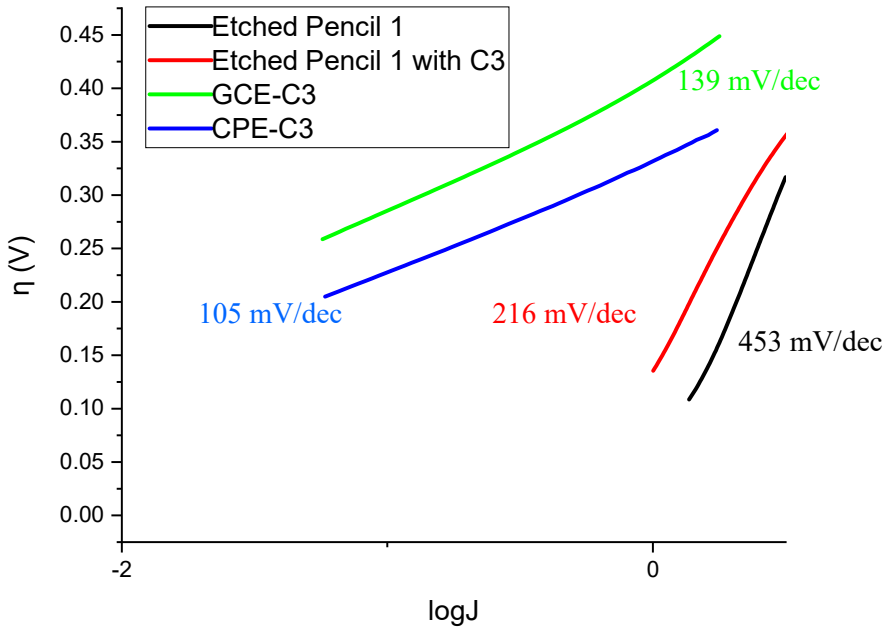

Figure 50. Etched pencil 1 with and without C3 compared to GCE-C3 and CPE-C3 Tafel slopes.

Figure 51 shows the Nyquist plots for GCE-C3, CPE-C3, Etched Pencil, and Etched Pencil with C3. Charge transfer resistance for GCE-C3 was ~1500 Ω at peak, ~2750 Ω for CPE-C3 at peak, ~3500 Ω for Etched Pencil 1, and ~2750 Ω for Etched Pencil with C3.

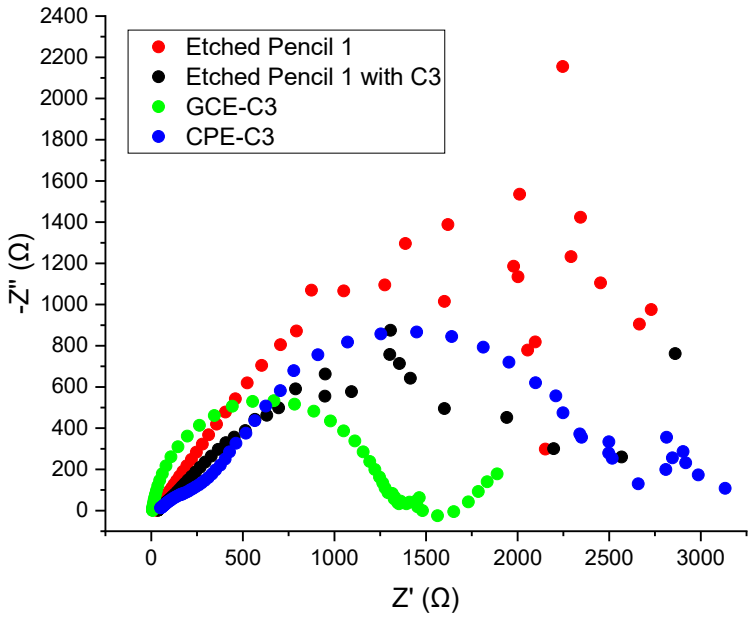

Figure 51. Etched pencil 1 with and without C3 compared to GCE-C3 and CPE-C3 Nyquist plot.

Since the pencils were only cycled once, they cannot accurately be compared to the glassy carbon and carbon paste electrodes. Therefore, it was desired to try and see if the pencils would hold up to reductive cycling. Reductive cycling on four different pencils was run for the best-known catalyst our group has produced, C15, on which glassy carbon have been the only electrodes previously studied with this TSC.

Two of the pencils were first run with etching preparation. The first etched pencil with C15 gave decrease in overpotential of 0.662 V to 0.475 V at peak 300 cycles, to 0.501 V after extensive reductive cycles, as shown in Figure 52. The Tafel slopes for the first etched pencil with C15 went from 187 mV/dec to 165 mV/dec at its peak of 300 cycles and after extensive reductive cycling was 193 mV/dec, as shown in Figure 53. Figure 54 is the Nyquist plot of the

first etched pencil with C15 at peak and after extensive cycling. Charge transfer resistance was ~6000 Ω initially, ~3000 Ω at peak, and still ~3000 Ω after reductive cycling.

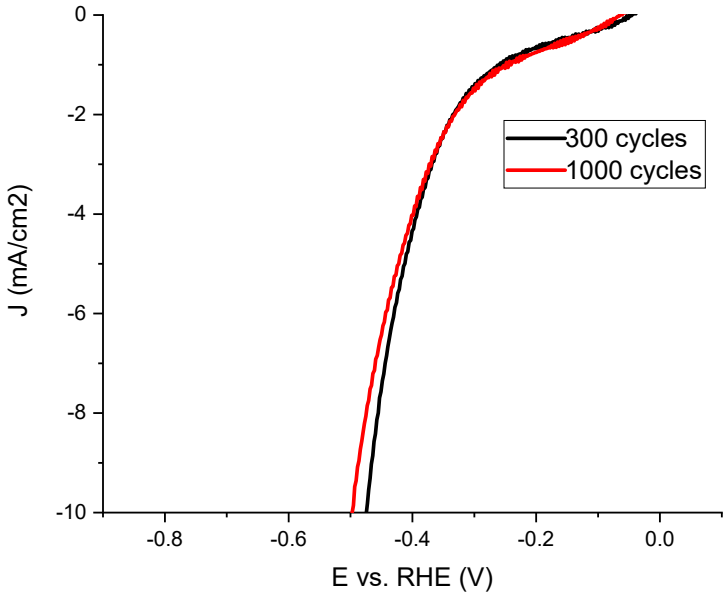

Figure 52. Etched pencil with C15 polarization curves at peak and after 1000 cycles.

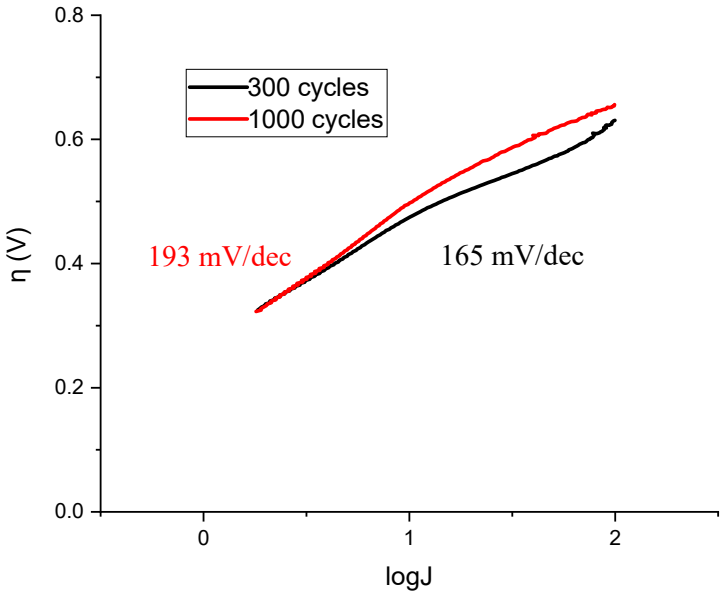

Figure 53. Etched pencil with C15 Tafel slopes at 300 and 1000 cycles.

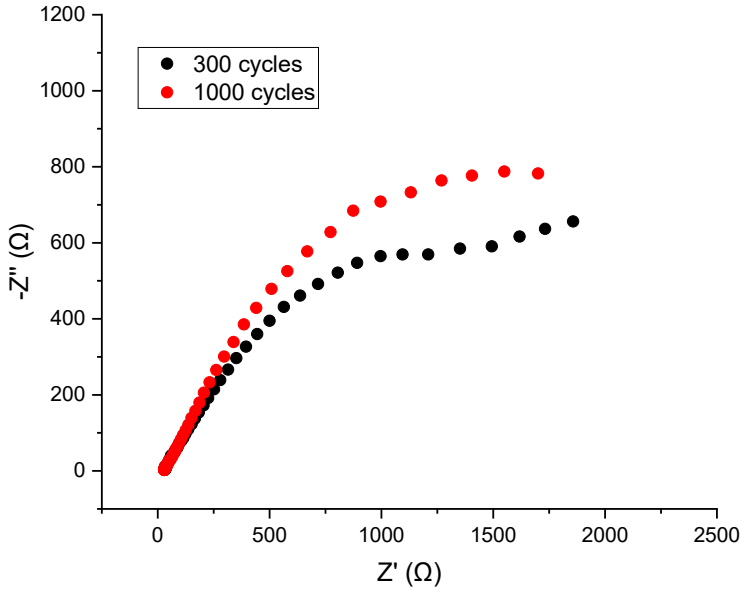

Figure 54. Nyquist plots of etched pencil with C15 polarization curves at peak and after 1000 cycles.

The second etched pencil with C15 gave decrease in overpotential of 0.597 V to 0.369 V at peak 400 cycles, to 0.401 V after extensive reductive cycles, as shown in Figure 55. This is a large drop in overpotential and suggests favorable catalytic activity. The Tafel slopes for the second etched pencil with C15 went from 273 mV/dec to 152 mV/dec at its peak of 400 cycles and after extensive reductive cycling was 178 mV/dec, as shown in Figure 56. Figure 57 is the Nyquist plot of the second etched pencil with C15 at peak and after extensive cycling. Charge transfer resistance was ~2000 Ω initially, ~1500 Ω at peak, and still ~1500 Ω after reductive cycling.

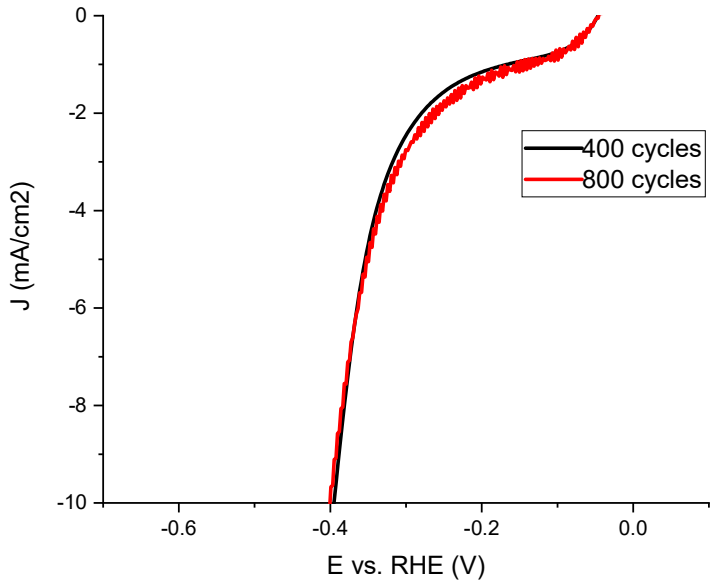

Figure 55. Etched pencil redo with C15 polarization curves at peak and after 800 cycles.

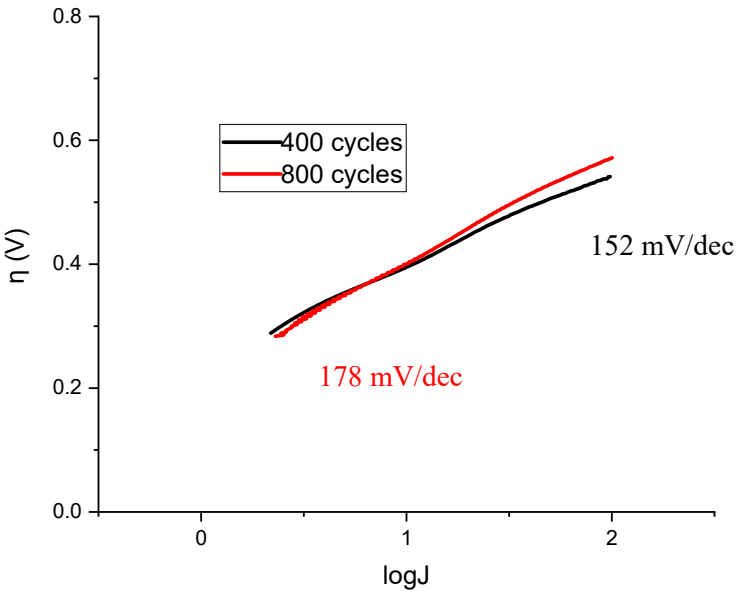

Figure 56. Etched pencil with C15 redo Tafel slope at 400 and 800 cycles.

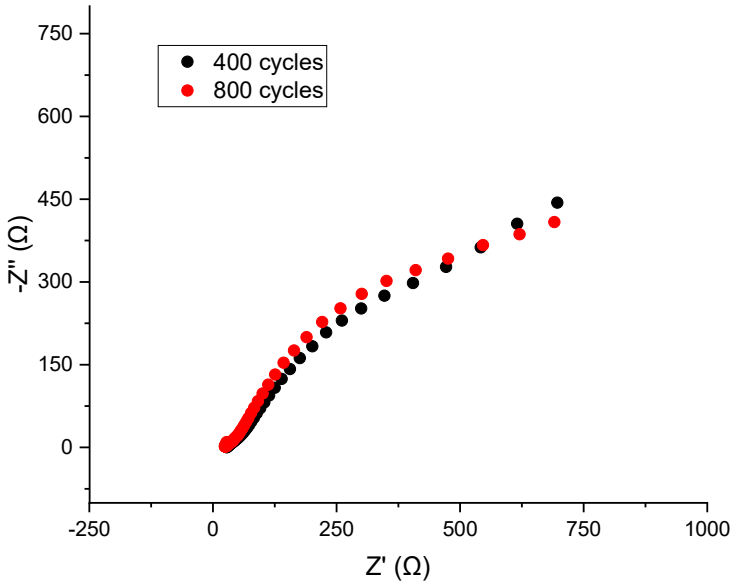

Figure 57. Etched pencil redo with C15 Nyquist plots at peak and after 800 cycles.

Two of the pencils were then run with no preparation, i.e., blank. It is important to note that because of the vast number of bubbles formed on the catalyst surface that stirring of the electrolyte solution was implemented for these tests, which can be seen in the fact that the data does look noisier compared to previous samples.

The first blank pencil with C15 decreased in overpotential from 0.699 V to 0.328 V at peak 300 cycles, to 0.329 V after extensive reductive cycles, as shown in Figure 58. The Tafel slopes for the first blank pencil with C15 went from 112 mV/dec to 114 mV/dec at its peak of 300 cycles and after extensive reductive cycling was 118 mV/dec, as shown in Figure 59. Figure 60 is the Nyquist plot of the first blank pencil with C15 at peak and after extensive cycling. Charge transfer resistance was ~70000 Ω initially, ~250 Ω at peak, and ~400 Ω after reductive cycling.

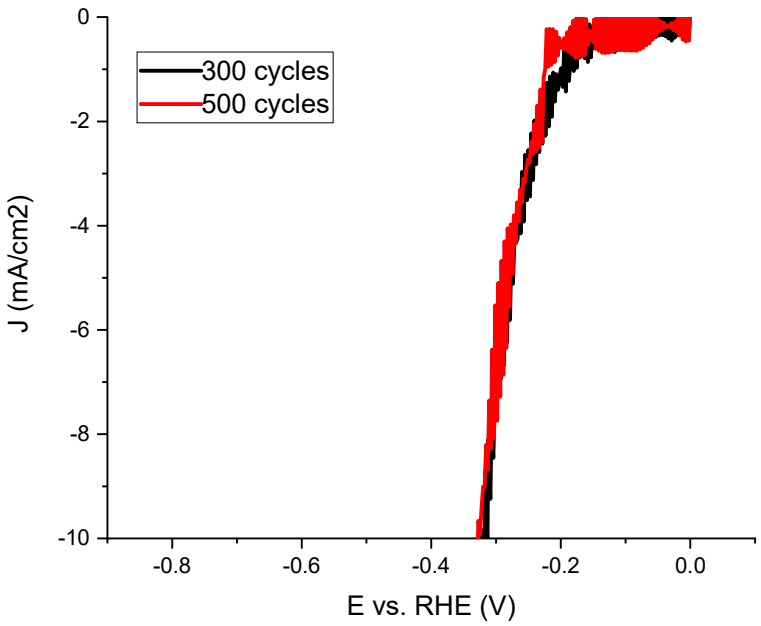

Figure 58. Blank pencil with C15 polarization curves at peak and after 500 cycles.

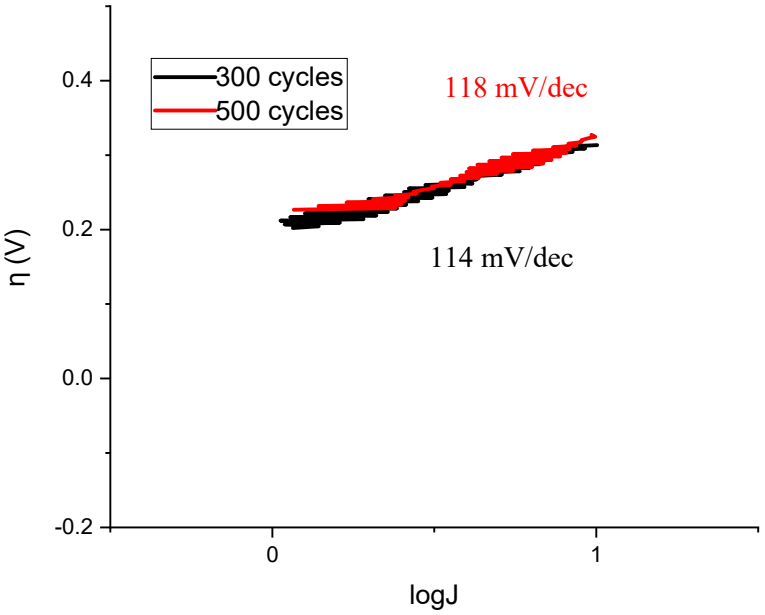

Figure 59. Blank pencil with C15 Tafel slope at peak and after 500 cycles.

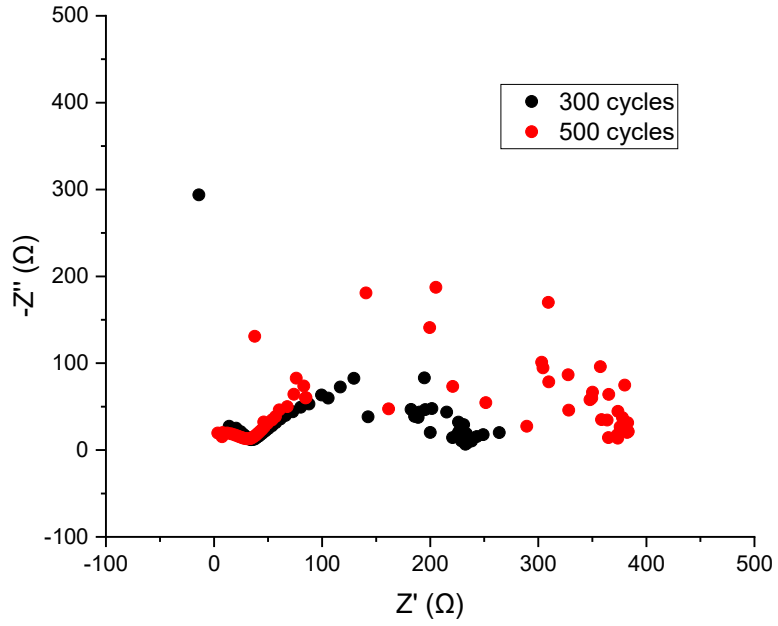

Figure 60. Blank pencil with C15 Nyquist plots at peak and after 500 cycles.

The second blank pencil with C15 decreased in overpotential from 0.394 V to 0.214 V at peak 300 cycles, to 0.234 V after extensive reductive cycles, as shown in Figure 61. The Tafel slopes for the second blank pencil with C15 went from 117 mV/dec to 96 mV/dec at its peak of 300 cycles and after extensive reductive cycling was 113 mV/dec, as shown in Figure 62. Figure 63 is the Nyquist plot of the first blank pencil with C15 at peak and after extensive cycling. Charge transfer resistance was ~1400 Ω initially, ~75 Ω at peak, and ~125 Ω after reductive cycling.

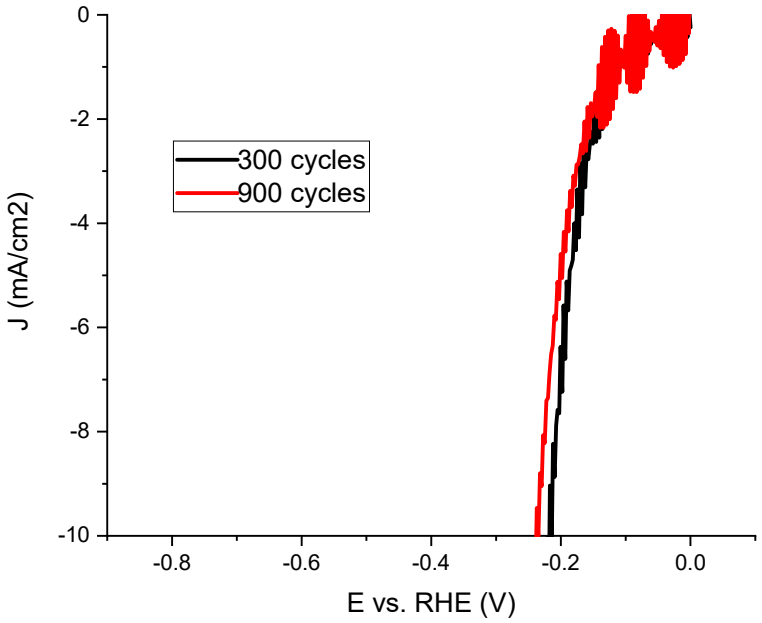

Figure 61. Blank pencil with C15 redo polarization curves at peak and after 900 cycles.

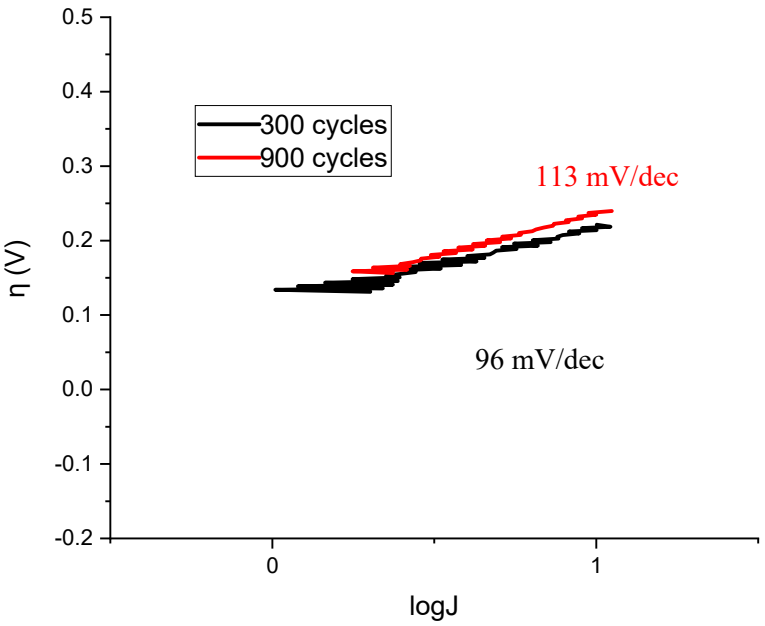

Figure 62. Blank pencil with C15 redo Tafel slopes at peak and after 900 cycles.

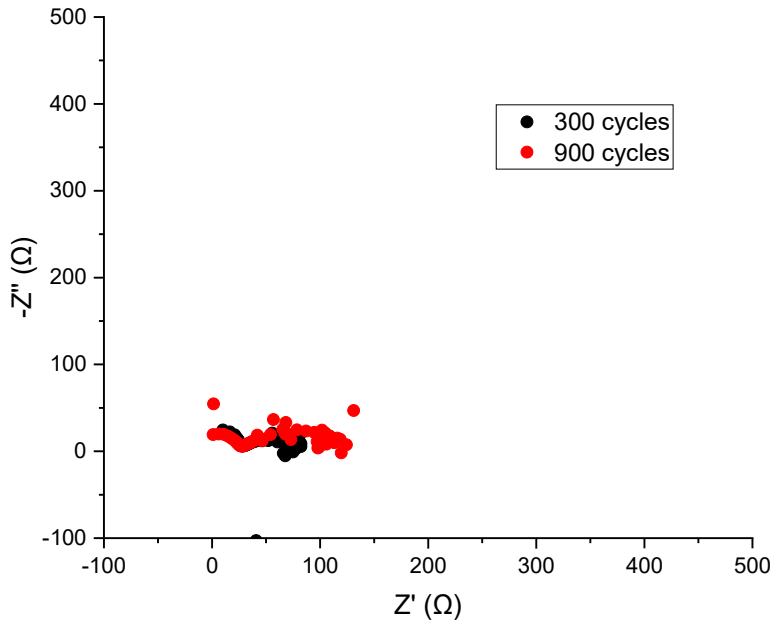

Figure 63. Blank pencil with C15 redo Nyquist plots at peak and after 900 cycles.

Overall, the pencil electrode proved to be promising with the C15 TSC metal complex, which reported low overpotentials and high stability. The overpotential and Tafel slope at peak activity of the promising pencil electrodes with TSCs are reported in Table 5, along with those of the promising CPE and GCEs. Table 6 reports a summary of the charge transfer resistances for the promising TSC complexes on pencil, carbon paste, and glassy carbon electrodes.

Table 5. Overpotentials and Tafel slopes for promising TSC complexes on pencil, carbon paste, and glassy carbon electrodes.

Sample Name	**Overpotential Prior to Cycling (V)**	**Overpotential at Peak (V)**	**Overpotential after Extensive Cycling (V)**	**Tafel Slope (mV/dec)**
GCE-C3	0.557	0.515	0.522	139

GCE-C6	0.706	0.519	0.550	116
GCE-C12 Nafion on Top	0.736	0.470	0.470	108
CPE-C3	0.719	0.454	0.454	133
Etched Pencil with C15	0.662	0.475	0.501	165
Etched Pencil with C15 Redo	0.597	0.369	0.401	152
Blank Pencil with C15	0.699	0.328	0.329	114
Blank Pencil with C15 Redo	0.394	0.214	0.234	96

Table 6. Charge transfer resistances for promising TSC complexes on pencil, carbon paste, and glassy carbon electrodes.

Sample Name	**Charge Transfer Prior to Cycling (Ω)**	**Charge Transfer at Peak (Ω)**	**Charge Transfer after Extensive Cycling (Ω)**
GCE-C3	~9000	~1500	~3000
GCE-C6	~21000	~550	~1000
GCE-C12 Nafion on Top	~4500	~350	~250

CPE-C3	~35000	~2750	~2750
Etched Pencil with C15	~6000	~3000	~3000
Etched Pencil with C15 Redo	~2000	~1500	~1500
Blank Pencil with C15	~70000	~250	~400
Blank Pencil with C15 Redo	~14000	~75	~125

V. CONCLUSIONS AND RECOMMENDATIONS

A. Conclusions

A series of modified electrodes to translate the nonaqueous, homogeneous HER activity of several TSCs to a solid support for heterogeneous applications in acidic aqueous environment were engineered and tested using electrochemical methods. Results of the electrochemical studies performed were presented, including polarization curves, Nyquist plots, and Tafel slopes to help evaluate catalytic efficiency. Glassy carbon electrodes were first used to examine electrochemically active TSC ligands and complexes. Modified standard pencil electrodes and carbon paste electrodes were then studied using TSCs as a means of increasing active sites and improving activity.

The evaluation of which of the TSC ligands and complexes were the most electrochemically active, by comparison of their HER performance on GCEs using reductive cycling, was presented first. The first catalyst with promising activity on GCE, C3, gave decrease in overpotential from 0.557 V to 0.515 V at its peak, a Tafel slope of 139 mV/dec, and charge transfer resistance of ~1500 Ω. The second catalyst with promising activity on GCE, C6, gave decrease in overpotential from 0.706 V to 0.519 V at its peak, a Tafel slope of 116 mV/dec, and charge transfer resistance of ~550 Ω. The third catalyst with promising activity on GCE, C12, gave decrease in overpotential from 0.736 V to 0.470 V at its peak, a Tafel slope of 108 mV/dec, and charge transfer resistance of ~350 Ω.

The GCE-C12 with Nafion on Top showed the most drastic decrease in overpotential after reductive cycling and also had the lowest Tafel slope, which translates to high exchange

current density. In addition, its resistance decreased over the course of the cycling indicating increased catalytic activity. These TSCs have the potential to be active electrocatalysts for HER.

Promising TSCs were then tested on CPEs, and their performance was analyzed using reductive cycling. The only catalyst to show increased HER performance with CPEs versus GCEs was C3. CPE-C3 showed a decrease in overpotential from 0.719 V to 0.454 V at its peak, a Tafel slope of 133 mV/dec, and charge transfer resistance of ~2750 Ω. This low overpotential along with the high stability of this sample make it a viable catalyst/electrode combination for HER.

Standard pencil electrodes were evaluated for best preparation practices and then tested with one of the new TSC complexes, C3, as well as with a known high-performing TSC previously studied by the group, namely C15. Pencils were prepared with no cleaning procedure (Blank), with sonicating and electrochemical cycling (Cleaned), and with acetone chemical etching (Etched). Two of these pencils with no catalyst were compared and it was found that of the three methods, etching resulted in the lowest overpotential in both cases.

Three etched pencils were then prepared with and without the C3 catalyst and were analyzed for HER catalytic potential. These potentials did vary from sample to sample, which showed the variability from pencil to pencil, but in each case, the pencils with the catalyst had slightly smaller overpotential values. Compared to the GCE and CPE with C3, the etched pencil with C3 reported the highest overpotential at 0.530-0.594 V for the three samples. In addition, the Tafel slope, 216 mV/dec, was much higher for the etched pencils with C3 than the GCE-C3 and CPE-C3. The charge transfer resistance was ~2750 Ω, and the etched pencils with catalyst

have comparable resistance with respect to the carbon paste (~3250 Ω), which is only slightly higher than that of glassy carbon (~1500 Ω).

Next, testing was done to see if the pencils would hold up to reductive cycling. Reductive cycling on four different pencils was run for the best-known catalyst our group has produced, C15, on which glassy carbon have been the only electrodes previously studied with this TSC. Two of the pencils were first run with etching preparation. The first etched pencil with C15 showed a decrease in overpotential from 0.662 V to 0.475 V at its peak, and the second showed a decrease in overpotential from 0.597 V to 0.369 V. The Tafel slopes for the two etched pencils with C15 at peak were a bit high, with values of 165 mV/dec and 152 mV/dec, respectively. The etched pencils with C15 had charge transfer resistances of ~1500 and ~3000 Ω.

Two of the pencils were then run with no preparation, i.e., blank. The first blank pencil with C15 gave decrease in overpotential from 0.699 V to 0.328 V at its peak, and the second showed decrease in overpotential from 0.394 V to 0.214 V at its peak. The Tafel slopes for the two etched pencils with C15 at peak were on the lower end, 114 mV/dec and 96 mV/dec, respectively. The blank pencils with C15 had charge transfer resistances of ~75 and ~250 Ω, which was the lowest of any sample.

Overall, the pencil electrode proved to be the most promising with the C15 TSC metal complex, which reported low overpotentials and high stability. Specifically, the blank pencil with C15 gave incredibly low overpotential values (0.214-0.328 V). Comparing these values to previously studied C15 on GCE, which reported overpotential of 0.450 V, it seems that this electrode/catalyst combination can be used as a cost-effective and efficient electrocatalyst for HER due to increased surface interactions.

B. Recommendations

There are several recommendations for future research that will be suggested. One recommendation is to try and engineer carbon paste electrode holders out of PVC pipe to save time and money in comparison to purchasing them. A major recommendation is for the lab to purchase a diamond blade saw to be able to test the same pencil multiple times to help with repeatability. Another recommendation is to test the C6 complex on pencil electrodes. Also, the C3 complex should be studied further using reductive cycling on pencil. In addition, C15 should be retested on glassy carbon to confirm the extremely low overpotential reported for the blank pencil with C15 is truly a much better electrode/catalyst combination. In addition, the blank pencil with C15 should be repeated more times to verify the results. The pencil electrodes should be characterized further using more surface analysis techniques. Also, quantitative equivalent circuit calculations should be done to model the exact charge transfer resistance for all samples. Further, a pencil electrode could be engineered to become a rotating disk electrode, the noise could be reduced for the C15 catalyst. All of these are recommended by the researcher to further this research with the ultimate goal of engineering the best possible modified electrode with TSC catalyst for HER.

C. Summary

The goal of this work was to develop and engineer new carbon materials while heterogenizing new and existing homogeneous thiomesicarbazone (TSC) compounds, supplied by the Grapperhaus/Buchanan Research Group, as electrocatalysis of HER. It was hypothesized that the interplay between the TSC catalysts and their microenvironment on surfaces may control the activity of heterogenized molecular catalysts, and that modification of this microenvironment can be done to improve HER electrocatalytic activity. The driving factors for the work were to

mitigate current thermodynamics, kinetics, and transport limitations. It was found that modified electrode surfaces of glassy carbon, carbon paste, and standard pencils with TSCs gave promising electrochemical activity to be used for HER catalysis application. Pencil electrodes have shown to report improved activity due to increased surface interactions. Specifically, the blank pencil with C15 (Ni-ATSM) reported the lowest overpotential of any sample, 0.214-0.328 V and will be further studied to prove its viability to be used as an electrocatalyst/electrode combination for HER.

VI. REFERENCES

1. Hoffert, M.I., et al., *Energy implications of future stabilization of atmospheric CO 2 content.* nature, 1998. **395**(6705): p. 881-884.
2. Lewis, N.S. and D.G. Nocera, *Powering the planet: Chemical challenges in solar energy utilization.* Proceedings of the National Academy of Sciences, 2006. **103**(43): p. 15729-15735.
3. Brandon, N. and Z. Kurban, *Clean energy and the hydrogen economy.* Philosophical Transactions of the Royal Society A: Mathematical, Physical and Engineering Sciences, 2017. **375**(2098): p. 20160400.
4. Facts, S. *Types of Renewable Energy*. 2020 12/22/2020 [cited 2021 7/7/2021]; Available from: https://www.sciencefacts.net/types-of-renewable-energy.html.
5. Luo, J., et al., *Water photolysis at 12.3% efficiency via perovskite photovoltaics and Earth-abundant catalysts.* Science, 2014. **345**(6204): p. 1593-1596.
6. Bull, S.R., *Renewable energy today and tomorrow.* Proceedings of the IEEE, 2001. **89**(8): p. 1216-1226.
7. Jiao, Y., et al., *Design of electrocatalysts for oxygen-and hydrogen-involving energy conversion reactions.* Chemical Society Reviews, 2015. **44**(8): p. 2060-2086.
8. Zhang, W., *Heterogenization of complexes with redox active ligands for hydrogen evolution reaction.* 2017.
9. Zheng, Y., et al., *Advancing the electrochemistry of the hydrogen-evolution reaction through combining experiment and theory.* Angewandte Chemie International Edition, 2015. **54**(1): p. 52-65.
10. Preuster, P., A. Alekseev, and P. Wasserscheid, *Hydrogen storage technologies for future energy systems.* Annual review of chemical and biomolecular engineering, 2017. **8**: p. 445-471.
11. Association, N.I., *Hydrogen Roadmap.* 2021: p. 12.
12. Holladay, J.D., et al., *An overview of hydrogen production technologies.* Catalysis today, 2009. **139**(4): p. 244-260.
13. Turner, J.A., *Sustainable hydrogen production.* Science, 2004. **305**(5686): p. 972-974.
14. Council, H., *Hydrogen scaling up: A sustainable pathway for the global energy transition.* 2017.
15. Plc, B. *Hydrogen*. 2021 [cited 2021 7/7/2021]; Available from: https://www.bp.com/en/global/corporate/energy-economics/energy-outlook/demand-by-fuel/hydrogen.html.
16. Group, E.R. *Solar Fuels Engineering Introduction*. 2021 [cited 2021 7/7/2021]; Available from: https://solarfuelsengineering.com/introduction/.
17. Sivula, K., F. Le Formal, and M. Grätzel, *Solar water splitting: progress using hematite (α-Fe2O3) photoelectrodes.* ChemSusChem, 2011. **4**(4): p. 432-449.
18. Khaselev, O. and J.A. Turner, *A monolithic photovoltaic-photoelectrochemical device for hydrogen production via water splitting.* Science, 1998. **280**(5362): p. 425-427.
19. Wikipedia, S.E. *Electrolysis of water*. 2020 2/19/2020 [cited 2021 7/7/2021]; Available from: https://simple.wikipedia.org/wiki/Electrolysis_of_water.
20. Ursua, A., L.M. Gandia, and P. Sanchis, *Hydrogen production from water electrolysis: current status and future trends.* Proceedings of the IEEE, 2011. **100**(2): p. 410-426.

21. Laursen, A.B., et al., *Electrochemical hydrogen evolution: Sabatier's principle and the volcano plot.* Journal of Chemical Education, 2012. **89**(12): p. 1595-1599.
22. Gupta, A.J., et al., *Effect of Stacking Interactions on the Translation of Structurally Related Bis (thiosemicarbazonato) nickel (II) HER Catalysts to Modified Electrode Surfaces.* Inorganic chemistry, 2019. **58**(18): p. 12025-12039.
23. Ooka, H., J. Huang, and K.S. Exner, *The Sabatier Principle in Electrocatalysis: Basics, Limitations, and Extensions.* Frontiers in Energy Research, 2021. **9**: p. 155.
24. Parsons, R., *The rate of electrolytic hydrogen evolution and the heat of adsorption of hydrogen.* Transactions of the Faraday Society, 1958. **54**: p. 1053-1063.
25. Nørskov, J.K., et al., *Trends in the exchange current for hydrogen evolution.* Journal of The Electrochemical Society, 2005. **152**(3): p. J23.
26. Jaramillo, T.F., et al., *Identification of active edge sites for electrochemical H2 evolution from MoS2 nanocatalysts.* science, 2007. **317**(5834): p. 100-102.
27. Zeng, M. and Y. Li, *Recent advances in heterogeneous electrocatalysts for the hydrogen evolution reaction.* Journal of Materials Chemistry A, 2015. **3**(29): p. 14942-14962.
28. Durst, J., et al., *New insights into the electrochemical hydrogen oxidation and evolution reaction mechanism.* Energy & Environmental Science, 2014. **7**(7): p. 2255-2260.
29. Conway, B. and B. Tilak, *Interfacial processes involving electrocatalytic evolution and oxidation of H2, and the role of chemisorbed H.* Electrochimica acta, 2002. **47**(22-23): p. 3571-3594.
30. Shinagawa, T., A.T. Garcia-Esparza, and K. Takanabe, *Insight on Tafel slopes from a microkinetic analysis of aqueous electrocatalysis for energy conversion.* Scientific reports, 2015. **5**(1): p. 1-21.
31. Zhang, C., et al., *Highly efficient and durable electrocatalyst based on nanowires of cobalt sulfide for overall water splitting.* ChemNanoMat, 2018. **4**(12): p. 1240-1246.
32. McKone, J.R., et al., *Earth-abundant hydrogen evolution electrocatalysts.* Chemical Science, 2014. **5**(3): p. 865-878.
33. Di Giovanni, C., et al., *Bioinspired iron sulfide nanoparticles for cheap and long-lived electrocatalytic molecular hydrogen evolution in neutral water.* Acs Catalysis, 2014. **4**(2): p. 681-687.
34. Zhang, J., et al., *Unveiling active sites for the hydrogen evolution reaction on monolayer MoS2.* Advanced Materials, 2017. **29**(42): p. 1701955.
35. Raj, I.A. and K. Vasu, *Transition metal-based cathodes for hydrogen evolution in alkaline solution: electrocatalysis on nickel-based ternary electrolytic codeposits.* Journal of applied electrochemistry, 1992. **22**(5): p. 471-477.
36. Kügler, M., et al., *Copper complexes as catalyst precursors in the electrochemical hydrogen evolution reaction.* Dalton Transactions, 2016. **45**(16): p. 6974-6982.
37. Tang, C., et al., *NiS2 nanosheets array grown on carbon cloth as an efficient 3D hydrogen evolution cathode.* Electrochimica Acta, 2015. **153**: p. 508-514.
38. Rountree, E.S. and J.L. Dempsey, *Reactivity of proton sources with a nickel hydride complex in acetonitrile: implications for the study of fuel-forming catalysts.* Inorganic chemistry, 2016. **55**(10): p. 5079-5087.
39. Dempsey, J.L., et al., *Hydrogen evolution catalyzed by cobaloximes.* Accounts of chemical research, 2009. **42**(12): p. 1995-2004.

40. Chen, W.-F., J.T. Muckerman, and E. Fujita, *Recent developments in transition metal carbides and nitrides as hydrogen evolution electrocatalysts.* Chemical communications, 2013. **49**(79): p. 8896-8909.
41. Chen, W.-F., et al., *Highly active and durable nanostructured molybdenum carbide electrocatalysts for hydrogen production.* Energy & Environmental Science, 2013. **6**(3): p. 943-951.
42. Hinnemann, B., et al., *Biomimetic hydrogen evolution: MoS2 nanoparticles as catalyst for hydrogen evolution.* Journal of the American Chemical Society, 2005. **127**(15): p. 5308-5309.
43. Popczun, E.J., et al., *Nanostructured nickel phosphide as an electrocatalyst for the hydrogen evolution reaction.* Journal of the American Chemical Society, 2013. **135**(25): p. 9267-9270.
44. Vrubel, H. and X. Hu, *Molybdenum boride and carbide catalyze hydrogen evolution in both acidic and basic solutions.* Angewandte Chemie International Edition, 2012. **51**(ARTICLE): p. 12703-12706.
45. Park, J.H., S. Kim, and A.J. Bard, *Novel carbon-doped TiO2 nanotube arrays with high aspect ratios for efficient solar water splitting.* Nano letters, 2006. **6**(1): p. 24-28.
46. Zheng, Y., et al., *Hydrogen evolution by a metal-free electrocatalyst.* Nature communications, 2014. **5**(1): p. 1-8.
47. Zheng, Y., et al., *Toward design of synergistically active carbon-based catalysts for electrocatalytic hydrogen evolution.* ACS nano, 2014. **8**(5): p. 5290-5296.
48. Zhou, X., et al. *MoS2 Decorated on Different Metal Oxide Nanotubular Structures with a High Density of Reactive Sites for HER Reactions*. in *ECS Meeting Abstracts*. 2018. IOP Publishing.
49. Li, Y., et al., *MoS2 nanoparticles grown on graphene: an advanced catalyst for the hydrogen evolution reaction.* Journal of the American Chemical Society, 2011. **133**(19): p. 7296-7299.
50. Falola, B.D., T. Wiltowski, and I.I. Suni, *Electrodeposition of MoS2 for charge storage in electrochemical supercapacitors.* Journal of The Electrochemical Society, 2016. **163**(9): p. D568.
51. Yan, Y., et al., *Recent development of molybdenum sulfides as advanced electrocatalysts for hydrogen evolution reaction.* Acs Catalysis, 2014. **4**(6): p. 1693-1705.
52. Bonde, J., et al., *Hydrogen evolution on nano-particulate transition metal sulfides.* Faraday discussions, 2009. **140**: p. 219-231.
53. Jaramillo, T.F., et al., *Hydrogen evolution on supported incomplete cubane-type [Mo3S4] 4+ electrocatalysts.* The Journal of Physical Chemistry C, 2008. **112**(45): p. 17492-17498.
54. Chen, Z., J. Kibsgaard, and T.F. Jaramillo. *Nanostructuring MoS [sub] 2 [/sub] for photoelectrochemical water splitting*. in *Solar Hydrogen and Nanotechnology V*. 2010. International Society for Optics and Photonics.
55. Dey, S., B. Mondal, and A. Dey, *An acetate bound cobalt oxide catalyst for water oxidation: role of monovalent anions and cations in lowering overpotential.* Physical Chemistry Chemical Physics, 2014. **16**(24): p. 12221-12227.
56. Pijpers, J.J., et al., *Light-induced water oxidation at silicon electrodes functionalized with a cobalt oxygen-evolving catalyst.* Proceedings of the National Academy of Sciences, 2011. **108**(25): p. 10056-10061.

57. Youngblood, W.J., et al., *Photoassisted overall water splitting in a visible light-absorbing dye-sensitized photoelectrochemical cell.* Journal of the American Chemical Society, 2009. **131**(3): p. 926-927.
58. Downes, C.A. and S.C. Marinescu, *Efficient electrochemical and photoelectrochemical H2 production from water by a cobalt dithiolene one-dimensional metal–organic surface.* Journal of the American Chemical Society, 2015. **137**(43): p. 13740-13743.
59. Kosower, E.M., et al., *N-Methyl-trimethylacetamide in Thin Films Displays Infrared Spectra of π-Helices, with Visible Static and Dynamic Growth Phases, and then a β-Sheet.* ChemPhysChem, 2014. **15**(16): p. 3592-3597.
60. Krassen, H., et al., *Immobilization of the [FeFe]-hydrogenase CrHydA1 on a gold electrode: design of a catalytic surface for the production of molecular hydrogen.* Journal of biotechnology, 2009. **142**(1): p. 3-9.
61. Tan, S.M. and M. Pumera, *Bottom-up electrosynthesis of highly active tungsten sulfide (WS3–x) films for hydrogen evolution.* ACS applied materials & interfaces, 2016. **8**(6): p. 3948-3957.
62. Jurss, J.W., et al., *Bioinspired design of redox-active ligands for multielectron catalysis: effects of positioning pyrazine reservoirs on cobalt for electro-and photocatalytic generation of hydrogen from water.* Chemical science, 2015. **6**(8): p. 4954-4972.
63. Haddad, A.Z., et al., *Beyond metal-hydrides: non-transition-metal and metal-free ligand-centered electrocatalytic hydrogen evolution and hydrogen oxidation.* Journal of the American Chemical Society, 2016. **138**(25): p. 7844-7847.
64. Haddad, A.Z., et al., *Metal-assisted ligand-centered electrocatalytic hydrogen evolution upon reduction of a bis (thiosemicarbazonato) Cu (II) complex.* Inorganic chemistry, 2017. **56**(18): p. 11254-11265.
65. Haddad, A.Z., et al., *Proposed ligand-centered electrocatalytic hydrogen evolution and hydrogen oxidation at a noninnocent mononuclear metal–thiolate.* Journal of the American Chemical Society, 2015. **137**(29): p. 9238-9241.
66. Zhang, W., et al., *Translation of ligand-centered hydrogen evolution reaction activity and mechanism of a rhenium-thiolate from solution to modified electrodes: A combined experimental and density functional theory study.* Inorganic chemistry, 2017. **56**(4): p. 2177-2187.
67. Calvary, C.A., et al., *Copper bis (thiomesicarbazone) Complexes with Pendent Polyamines: Effects of Proton Relays and Charged Moieties on Electrocatalytic HER.* European Journal of Inorganic Chemistry, 2021. **2021**(3): p. 267-275.
68. Zittel, H. and F. Miller, *A Glassy-Carbon Electrode for Voltammetry.* Analytical Chemistry, 1965. **37**(2): p. 200-203.
69. Tavares, P.H.C.P. and P.J.S. Barbeira, *Influence of pencil lead hardness on voltammetric response of graphite reinforcement carbon electrodes.* Journal of Applied Electrochemistry, 2008. **38**(6): p. 827-832.
70. Sharma, S., R. Jain, and A.N. Raja, *Pencil graphite electrode: an emerging sensing material.* Journal of The Electrochemical Society, 2019. **167**(3): p. 037501.
71. Gong, Z.Q., A.N.A. Sujari, and S. Ab Ghani, *Electrochemical fabrication, characterization and application of carboxylic multi-walled carbon nanotube modified composite pencil graphite electrodes.* Electrochimica Acta, 2012. **65**: p. 257-265.
72. Sağlam, Ö., et al., *Differential pulse voltammetric determination of eugenol at a pencil graphite electrode.* Materials Science and Engineering: C, 2016. **60**: p. 156-162.

73. Kayan, D.B., et al., *Electrocatalytic hydrogen production on a modified pencil graphite electrode.* International Journal of Hydrogen Energy, 2017. **42**(4): p. 2457-2463.
74. Bond, A.M., et al., *An inexpensive and renewable pencil electrode for use in field-based stripping voltammetry.* Analytica Chimica Acta, 1997. **345**(1-3): p. 67-74.
75. Bhowmik, R., *Ferromagnetism in lead graphite-pencils and magnetic composite with CoFe2O4 particles.* Composites Part B: Engineering, 2012. **43**(2): p. 503-509.
76. Handl, W., *Composition for the preparation of pencil lead*. 1992, Google Patents.
77. Sousa, M.C. and J.W. Buchanan. *Observational models of graphite pencil materials*. in *Computer Graphics Forum*. 2000. Wiley Online Library.
78. Paudel, M.K., Theodore; Zhao, Jianchao; Wilkerson, Eric; Arts, Amanda Mae; Grimm, Evan; Gupta, Alex; Gupta, Gautam, *Unravelling the Potential of Disposable Pencil Electrodes as Catalyst Support*. 2017-2021. p. 8.
79. Merz, A., *Chemically modified electrodes*, in *Electrochemistry IV*. 1990, Springer. p. 49-90.
80. Murray, R.W., A.G. Ewing, and R.A. Durst, *Chemically modified electrodes. Molecular design for electroanalysis.* Analytical Chemistry, 1987. **59**(5): p. 379A-390A.
81. Wang, J., et al., *Metal-dispersed carbon paste electrodes.* Analytical Chemistry, 1992. **64**(11): p. 1285-1288.
82. Abbaspour, A. and E. Mirahmadi, *Electrocatalytic hydrogen evolution reaction on carbon paste electrode modified with Ni ferrite nanoparticles.* Fuel, 2013. **104**: p. 575-582.
83. Ghiamaty, Z., et al., *Synthesis of palladium–carbon nanotube–metal organic framework composite and its application as electrocatalyst for hydrogen production.* Journal of Nanostructure in Chemistry, 2016. **6**(4): p. 299-308.
84. Abbaspour, A., F. Norouz-Sarvestani, and E. Mirahmadi, *Electrocatalytic behavior of carbon paste electrode modified with metal phthalocyanines nanoparticles toward the hydrogen evolution.* Electrochimica acta, 2012. **76**: p. 404-409.
85. Almeida, C. and B. Giannetti, *A new and practical carbon paste electrode for insoluble and ground samples.* Electrochemistry Communications, 2002. **4**(12): p. 985-988.
86. Remita, H., et al., *Activity evaluation of carbon paste electrodes loaded with pt nanoparticles prepared in different radiolytic conditions.* Journal of Solid State Electrochemistry, 2006. **10**(7): p. 506-511.
87. Bard, A.J. and L.R. Faulkner, *Fundamentals and applications.* Electrochemical methods, 2001. **2**(482): p. 580-632.
88. Lasia, A., *Hydrogen evolution reaction.* Handbook of fuel cells, 2010. **815**.
89. McCrory, C.C., et al., *Benchmarking heterogeneous electrocatalysts for the oxygen evolution reaction.* Journal of the American Chemical Society, 2013. **135**(45): p. 16977-16987.
90. Kenjo, T., Y. Yamakoshi, and K. Wada, *An Estimation of the Electrode-Electrolyte Contact Area by Linear Sweep Voltammetry in Pt/ZrO2 Oxygen Electrodes.* Journal of The Electrochemical Society, 1993. **140**(8): p. 2151.
91. Ma, H., *Mechanistic Electrochemistry: Investigations of Electrocatalytic Mechanisms for H2S Detection Applications*. 2017, University of Cambridge.
92. Andrienko, D., *Cyclic voltammetry.* John Wiely & Sons publication, New York, 2008: p. 3-12.
93. Lether, F. and P. Wenston, *An algorithm for the numerical evaluation of the reversible Randles-Sevcik function.* Computers & chemistry, 1987. **11**(3): p. 179-183.

94. Kissinger, P.T. and W.R. Heineman, *Cyclic voltammetry.* Journal of Chemical Education, 1983. **60**(9): p. 702.
95. Finklea, H.O., et al., *Characterization of octadecanethiol-coated gold electrodes as microarray electrodes by cyclic voltammetry and ac impedance spectroscopy.* Langmuir, 1993. **9**(12): p. 3660-3667.
96. Nicholson, R.S. and I. Shain, *Theory of stationary electrode polarography. Single scan and cyclic methods applied to reversible, irreversible, and kinetic systems.* Analytical chemistry, 1964. **36**(4): p. 706-723.
97. Mirceski, V., et al., *Square-wave voltammetry: A review on the recent progress.* Electroanalysis, 2013. **25**(11): p. 2411-2422.
98. Ramaley, L. and M.S. Krause, *Theory of square wave voltammetry.* Analytical Chemistry, 1969. **41**(11): p. 1362-1365.
99. Osteryoung, J.G. and R.A. Osteryoung, *Square wave voltammetry.* Analytical chemistry, 1985. **57**(1): p. 101-110.
100. Cepeda Arque, G.A., *Development and Implementation of Techniques to Characterize Solid Oxide Fuel Cells.* 2016.
101. Nahir, T.M., *Impedance Spectroscopy: Theory, Experiment, and Applications, Edited by Evgenij Barsoukov (Texas Instruments Inc.) and J. Ross Macdonald (University of North Carolina, Chapel Hill). John Wiley & Sons, Inc.: Hoboken, NJ. 2005. xvii+ 596 pp. $125.00. ISBN 0471-64749-7*. 2005, ACS Publications.
102. Wu, J., et al., *Diagnostic tools in PEM fuel cell research: Part I Electrochemical techniques.* International journal of hydrogen energy, 2008. **33**(6): p. 1735-1746.
103. Interfaces, P.C.E. *Bode and Nyquist Plot*. [cited 2021 8/4/2021]; Available from: https://www.palmsens.com/knowledgebase-article/bode-and-nyquist-plot/.
104. Marion, D., *An introduction to biological NMR spectroscopy.* Molecular & Cellular Proteomics, 2013. **12**(11): p. 3006-3025.
105. Keeler, J., *Understanding NMR spectroscopy*. 2011: John Wiley & Sons.
106. James, T.L., *Fundamentals of NMR.* Online Textbook: Department of Pharmaceutical Chemistry, University of California, San Francisco, 1998: p. 1-31.
107. Dietmar, K.F., Steven; Soderberg, Tim. *Chemical Shifts in ¹H NMR Spectroscopy*. 2021 [cited 2021 7/16/21]; Available from: https://chem.libretexts.org/Bookshelves/Organic_Chemistry/Map%3A_Organic_Chemistry_(McMurry)/13%3A_Structure_Determination_-_Nuclear_Magnetic_Resonance_Spectroscopy/13.03%3A_Chemical_Shifts_in_H_NMR__Spectroscopy.
108. Ng, L.M. and R. Simmons, *Infrared spectroscopy.* Analytical chemistry, 1999. **71**(12): p. 343-350.
109. Harris, D.C. and M.D. Bertolucci, *Symmetry and spectroscopy: an introduction to vibrational and electronic spectroscopy*. 1989: Courier Corporation.
110. Ashenhurst, J. *Infrared Spectroscopy: A Quick Primer On Interpreting Spectra*. 2020 2/19/20 [cited 2021 7/16/21]; Available from: https://www.masterorganicchemistry.com/2016/11/23/quick_analysis_of_ir_spectra/.
111. Zhou, W., et al., *Fundamentals of scanning electron microscopy (SEM)*, in *Scanning microscopy for nanotechnology*. 2006, Springer. p. 1-40.
112. Velasco, E., *Scanning Electron Microscope (SEM) as a means to determine dispersibility.* 2013.

113. Jain, R., et al., *Ligand-assisted metal-centered electrocatalytic hydrogen evolution upon reduction of a bis (thiosemicarbazonato) Ni (II) complex.* Inorganic chemistry, 2018. **57**(21): p. 13486-13493.
114. West, D.X., et al., *Copper (II) and nickel (II) complexes of 2, 3-butanedione bis (N (3)-substituted thiomesicarbazones).* Polyhedron, 1997. **16**(11): p. 1895-1905.
115. Block, E., et al., *o-Lithiothiophenol equivalents. Generation, reactions and applications in synthesis of hindered thiolate ligands.* Journal of the American Chemical Society, 1989. **111**(2): p. 658-665.
116. Betts, H.M., et al., *Controlled Axial Coordination: Solid-Phase Synthesis and Purification of Metallo-Radiopharmaceuticals.* Angewandte Chemie International Edition, 2008. **47**(44): p. 8416-8419.
117. Holland, J.P., et al., *Functionalized bis (thiosemicarbazonato) complexes of zinc and copper: synthetic platforms toward site-specific radiopharmaceuticals.* Inorganic chemistry, 2007. **46**(2): p. 465-485.

VII. APPENDICES

A. Appendix A: TSC Ligand and Metal Complex Synthesis and Characterization

i. C1: BTP4A

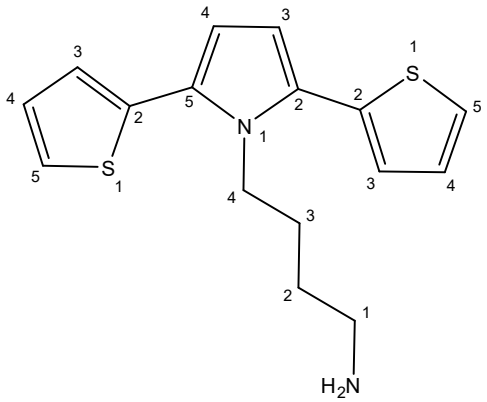

Molecular Weight: 302.45
m/z: 302.09 (100.0%), 303.09 (17.3%), 304.09 (9.0%), 303.09 (1.6%), 304.10 (1.4%)

Figure 64. Bis-thiophenepyrrolebutylamine (BTP4A) (1mM) 0.1M TBAHFP in DCM molecular structure with molecular weight.

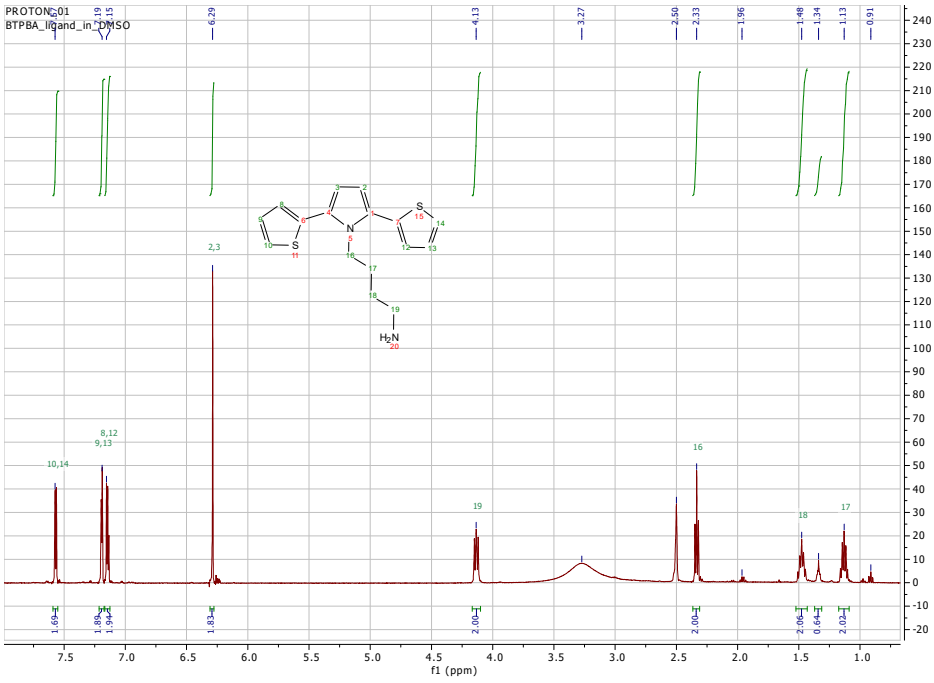

Figure 65. BTP4A NMR spectrum.

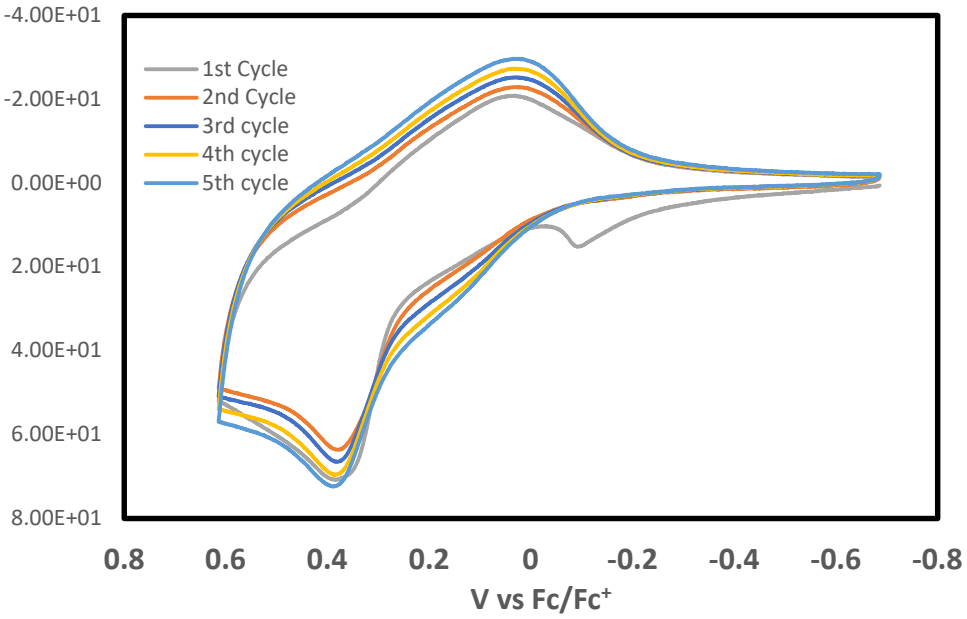

Figure 66. Five cycle polymerization of BTP4A on GC.

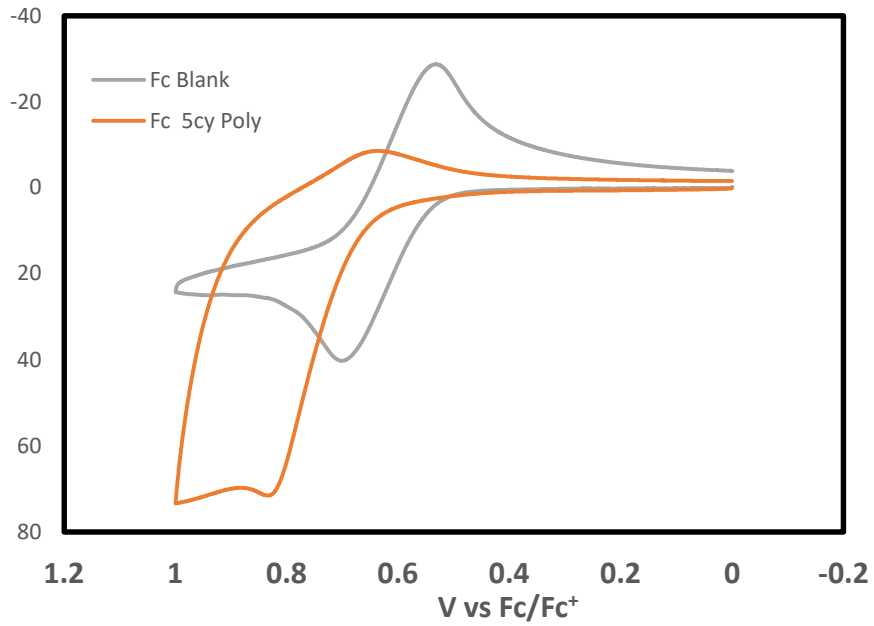

Figure 67. Ferrocene comparison blank and BTP4A polymer on GC.

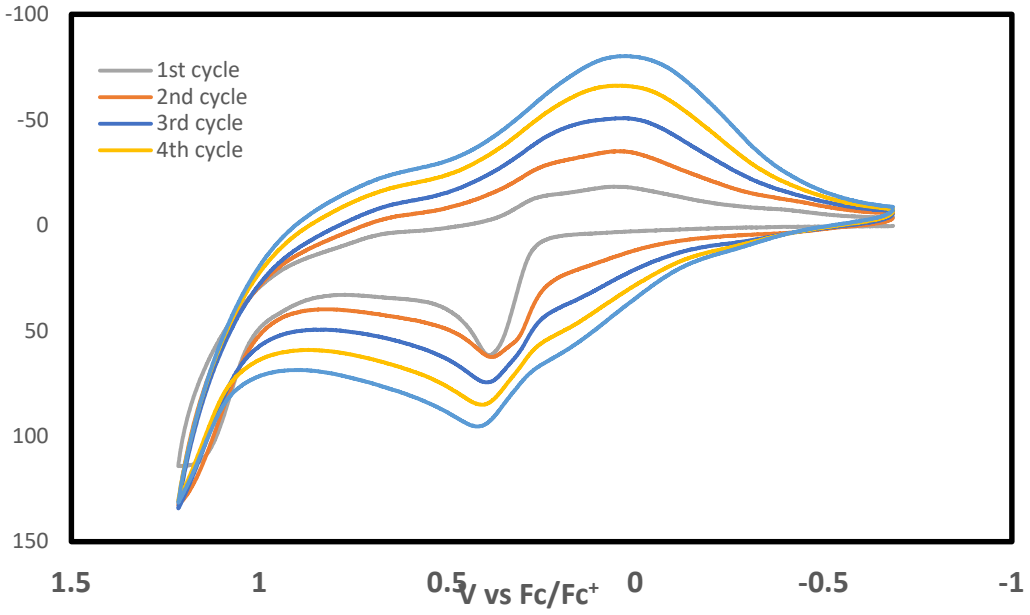

Figure 68. Five cycle polymerization of BTP4A+EDOT (high ox pot.) on GC.

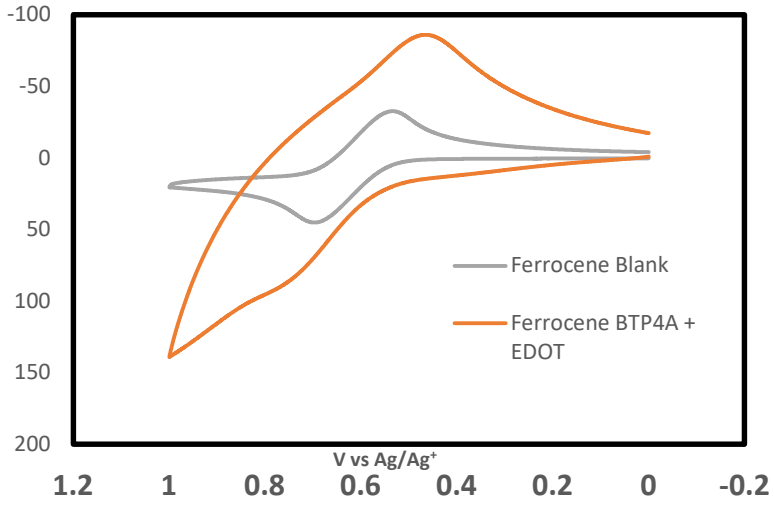

Figure 69. Ferrocene comparison blank vs BTP4A+EDOT on GC.

ii. C2: ATSMpy Single Arm

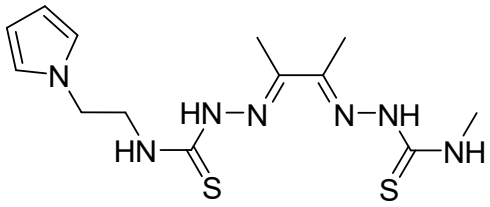

Figure 70. ATSMpy single arm molecular structure.

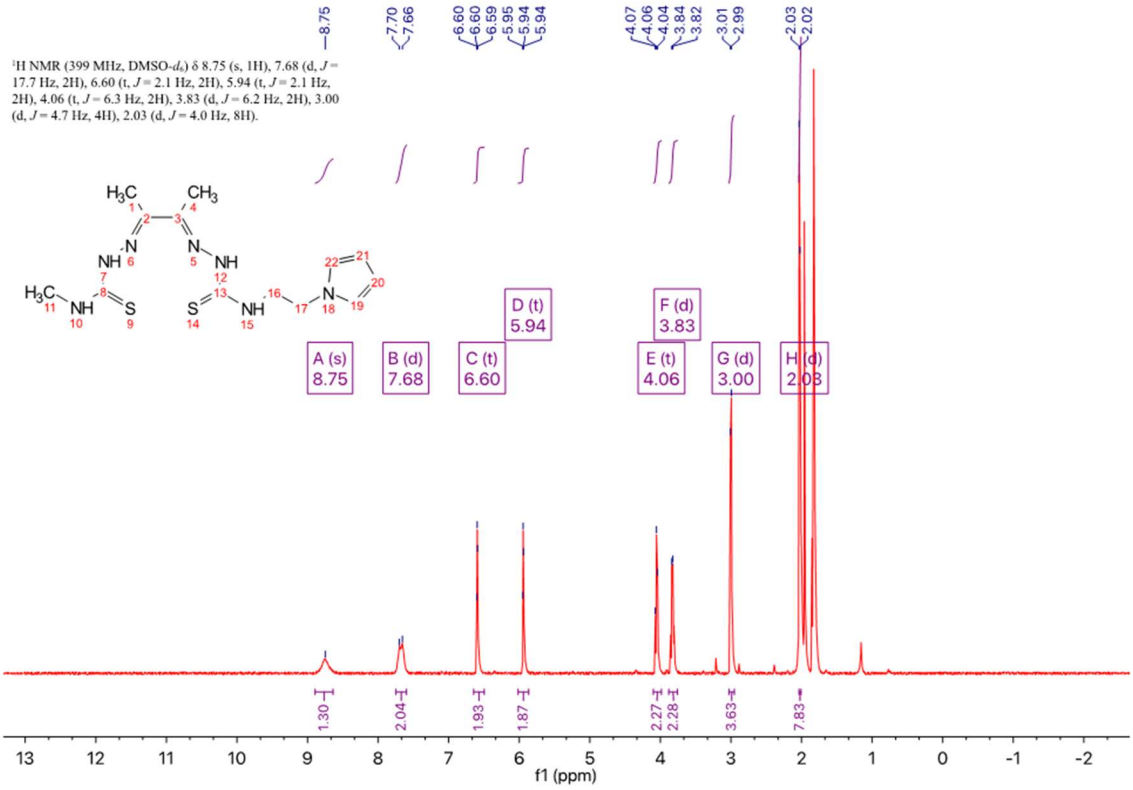

Figure 71. NMR spectrum for ATSMpy single arm.

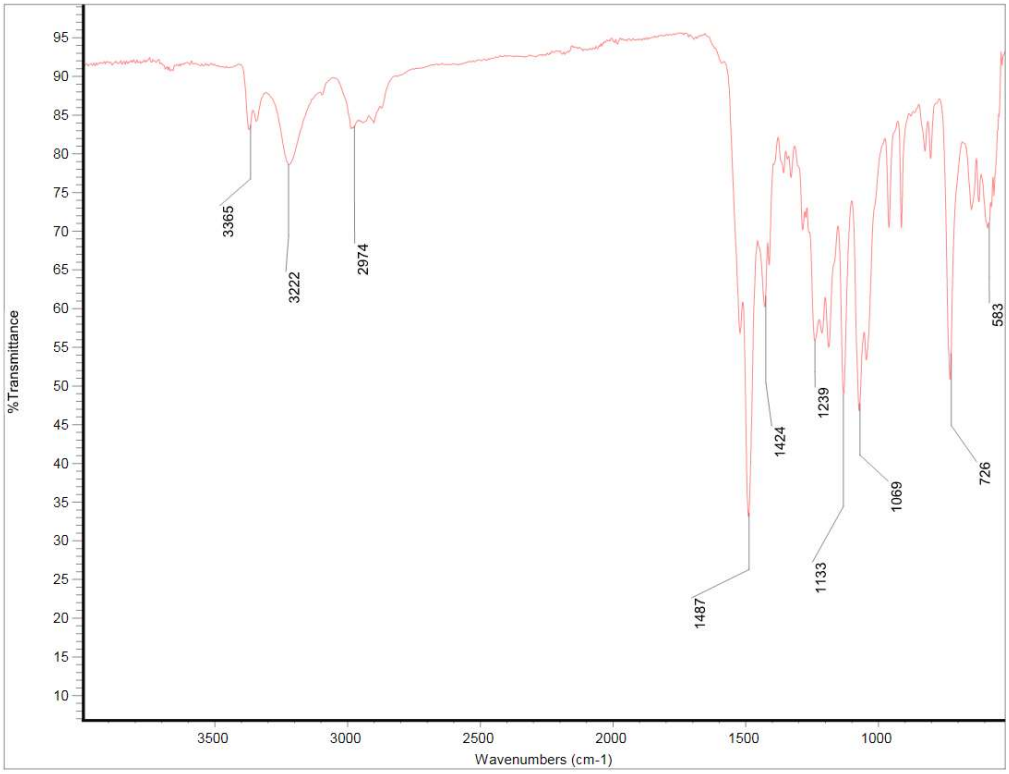

Figure 72. Infrared spectrum for ATSMpy single arm.

iii. C3: Ni-ATSMpy Single Arm

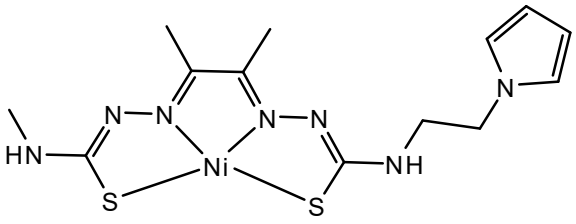

Figure 73. Ni-ATSMpy (0.6mM) single arm 0.1M TBAF in acetonitrile molecular structure.

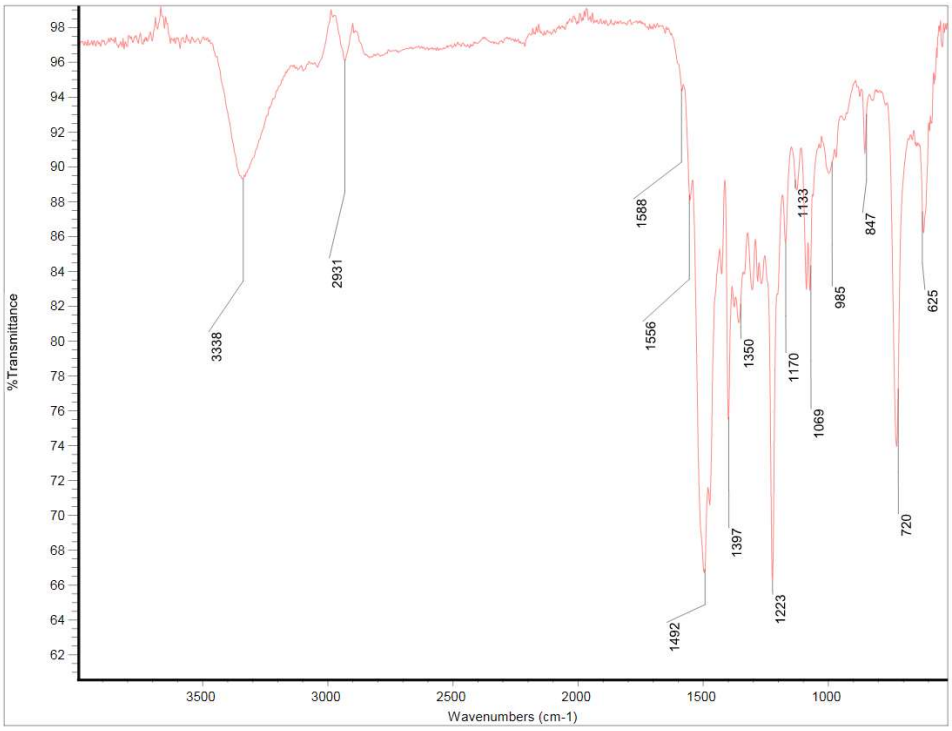

Figure 74. Infrared spectrum for Ni-ATSMpy single arm.

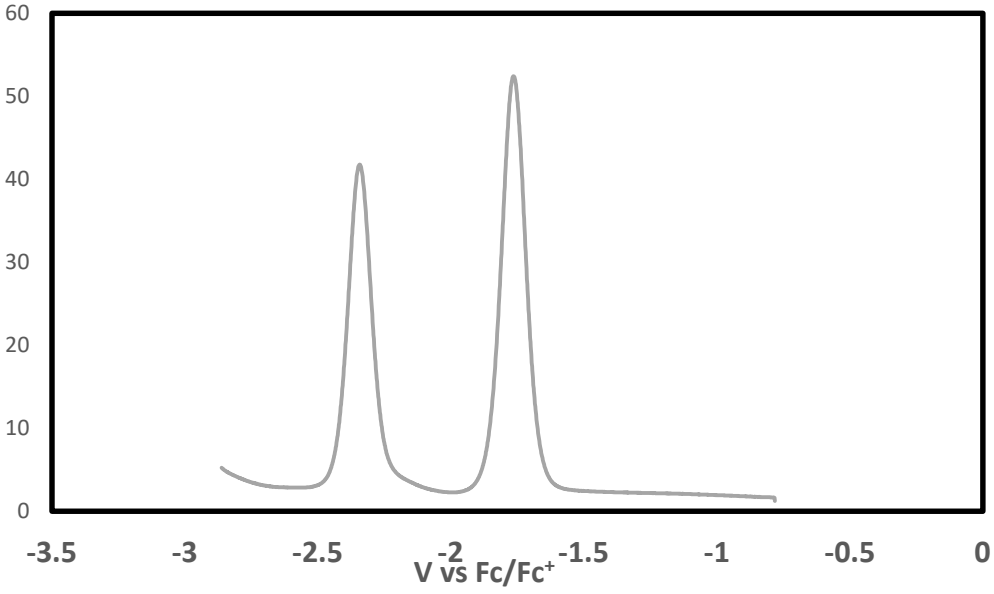

Figure 75. Square wave voltammetry for Ni-ATSMpy single arm.

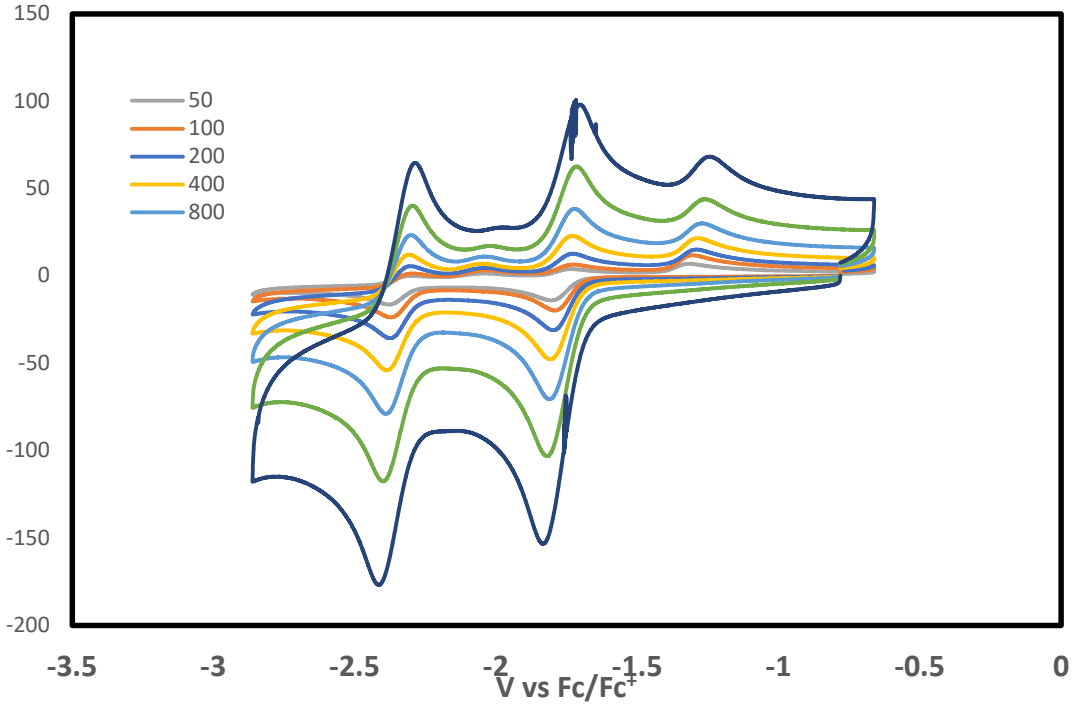

Figure 76. Scan rate dependence of Ni-ATSMpy single arm.

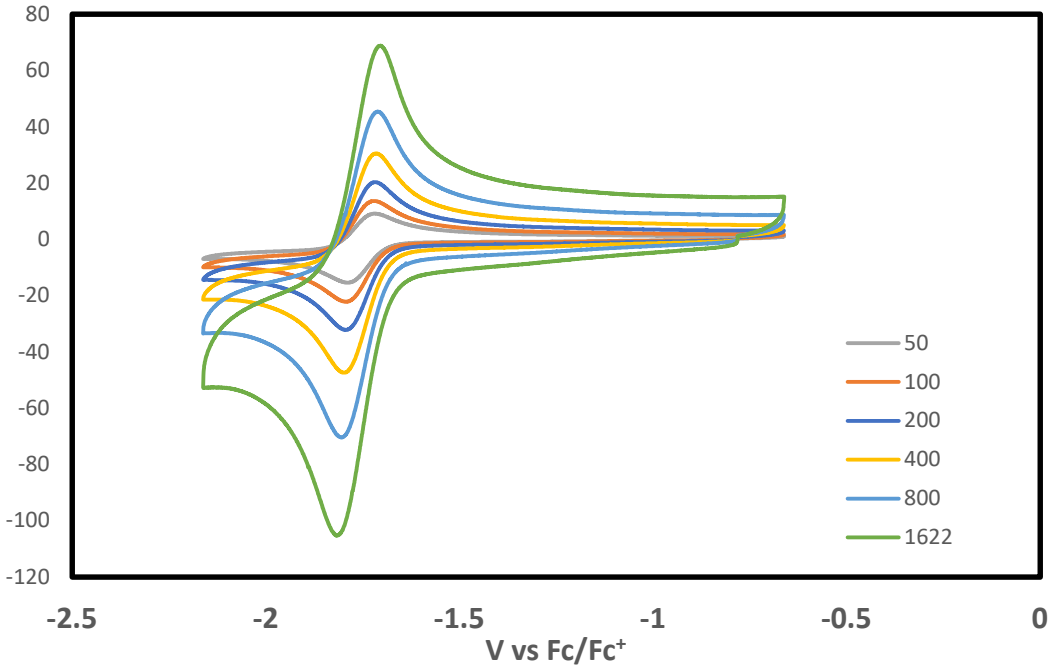

Figure 77. Scan rate dependence of first reduction peak. Ni-ATSMpy single arm.

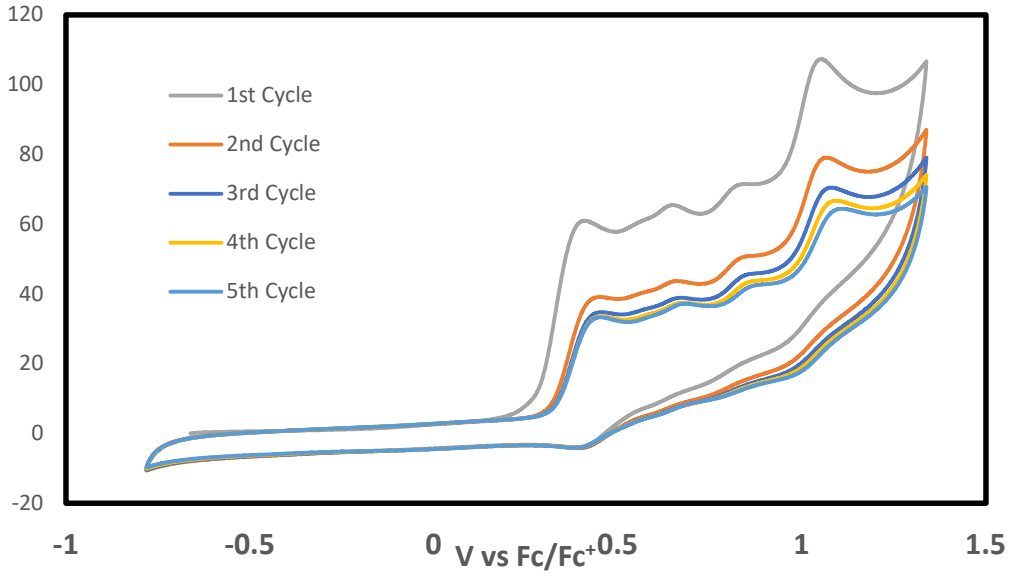

Figure 78. Five cycle of Ni-ATSMpy single arm in oxidative region at 200mV/s.

iv. C4: Zn-ATSMpy Single Arm

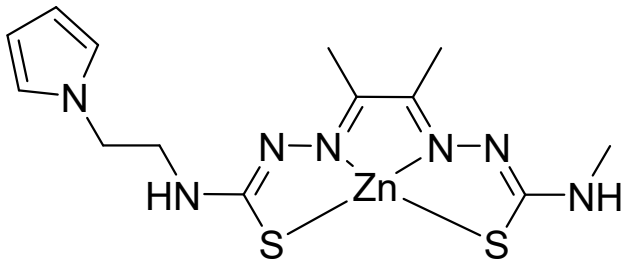

Figure 79. Zn-ATSMpy single arm molecular structure.

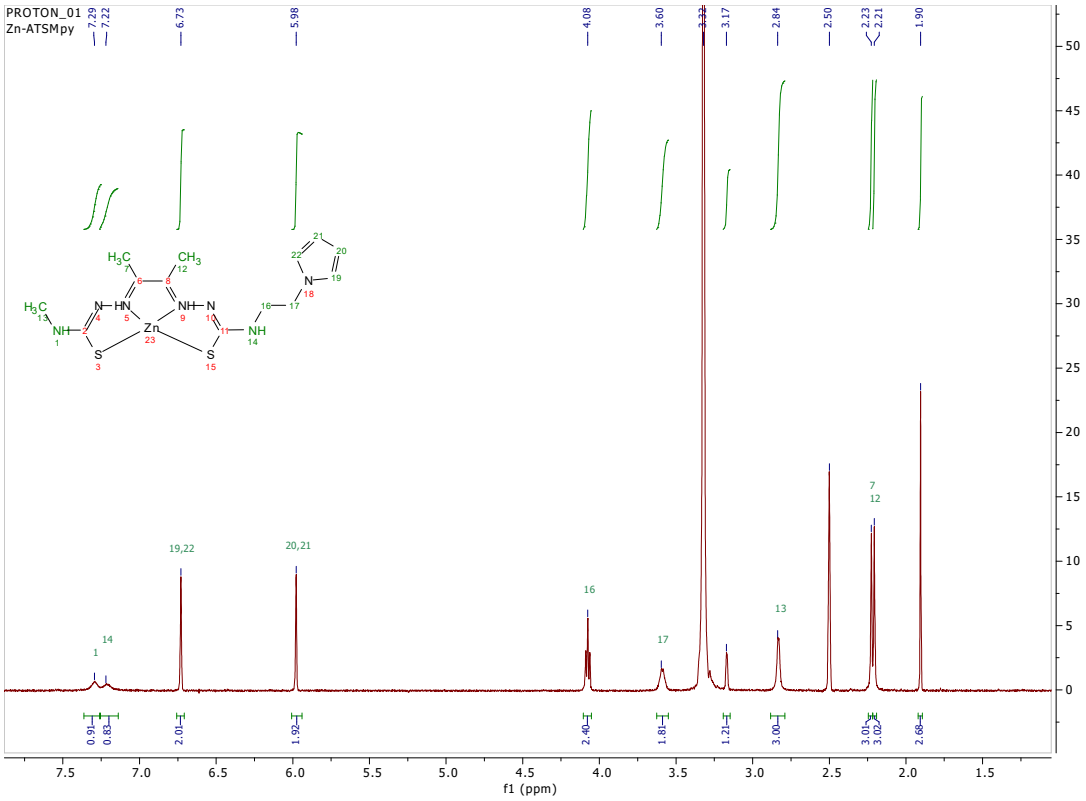

Figure 80. NMR spectrum Zn-ATSMpy single arm.

v. <u>C5: ATSMpy Double Arm</u>

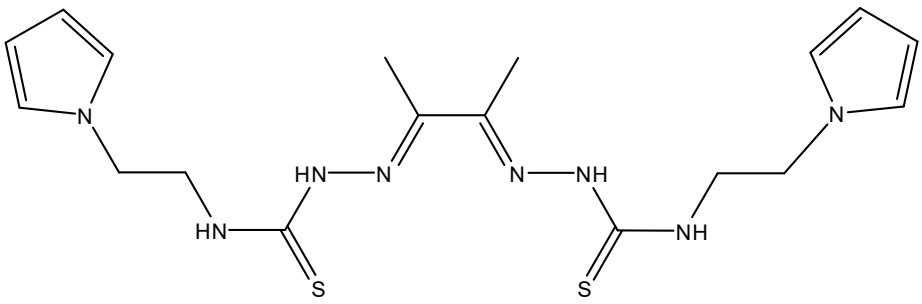

Figure 81. ATSMpy double arm (0.1mM) 0.1M $NaClO_4$ and 0.1M $KClO_4$ as electrolyte molecular structure.

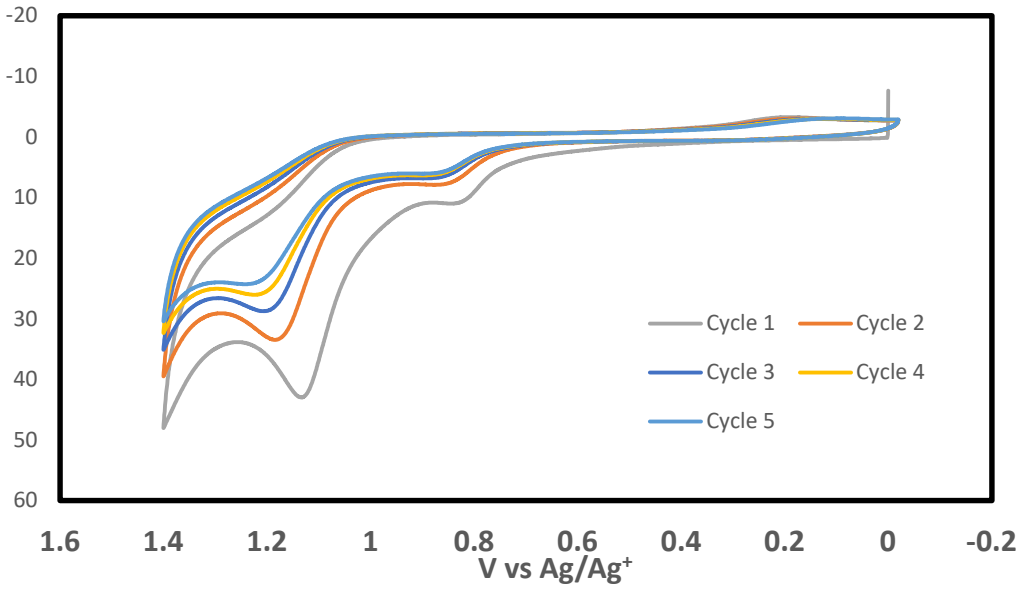

Figure 82. Five cycle oxidation on GC for ATSMpy double arm.

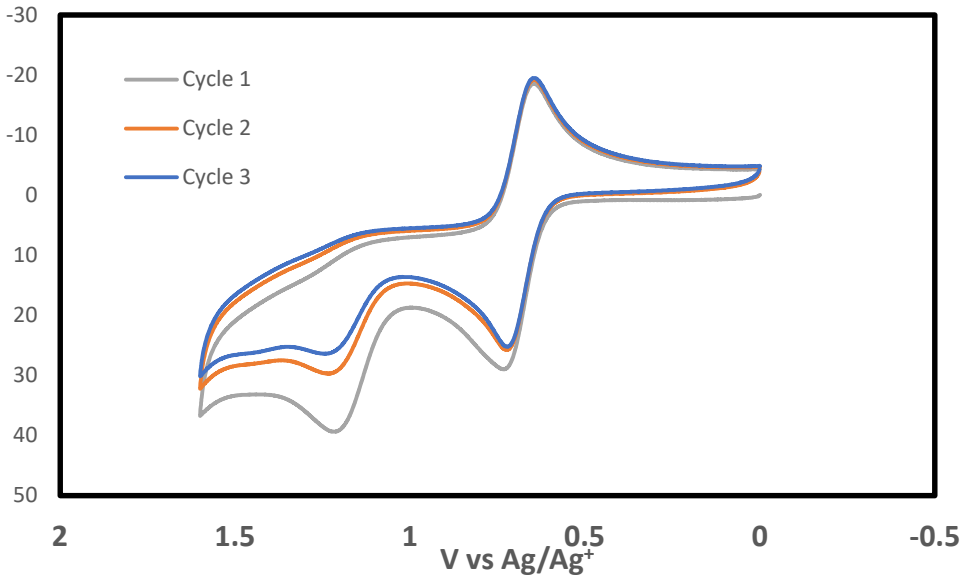

Figure 83. Three cycle oxidation in blank after five cycle polymerization on GC ATSMpy double arm.

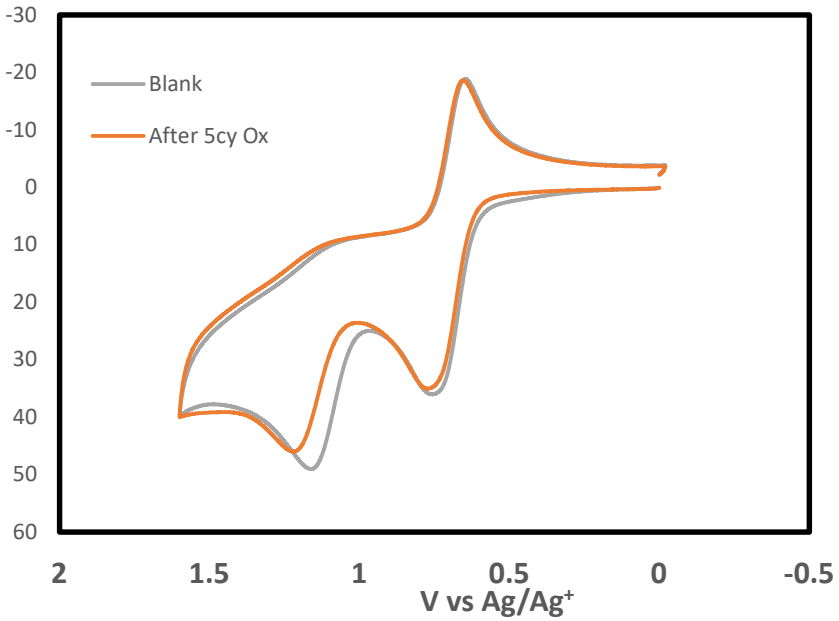

Figure 84. Ferrocene comparison on GC electrode ATSMpy double arm.

vi. C6: Ni-ATSMpy Double Arm

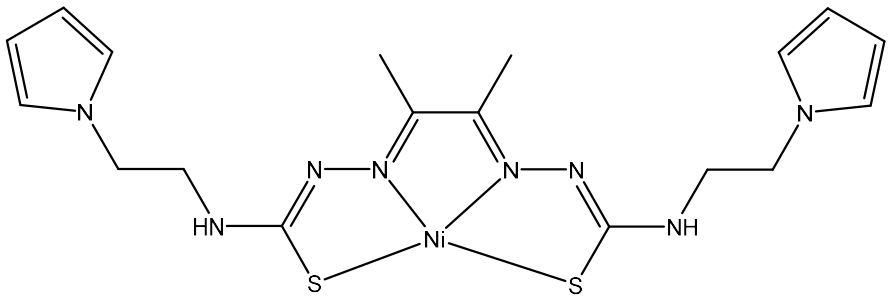

Figure 85. Ni-ATSMpy double arm (0.2mM) 0.1M TBAHFP as electrolyte molecular structure.

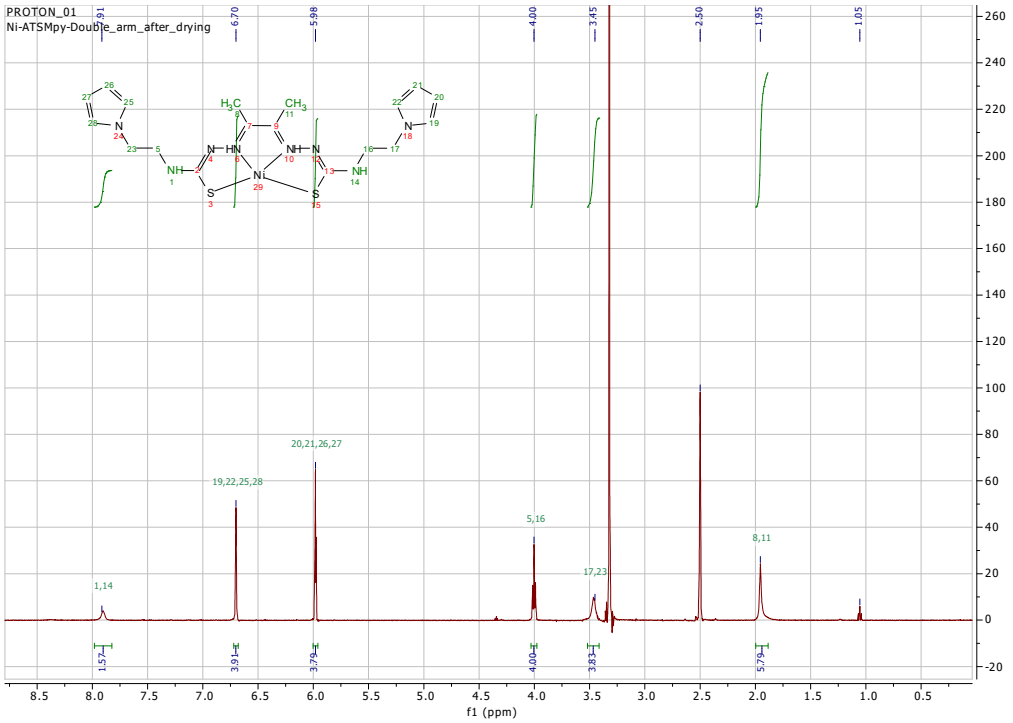

Figure 86. Ni-ATSMpy double arm NMR spectrum.

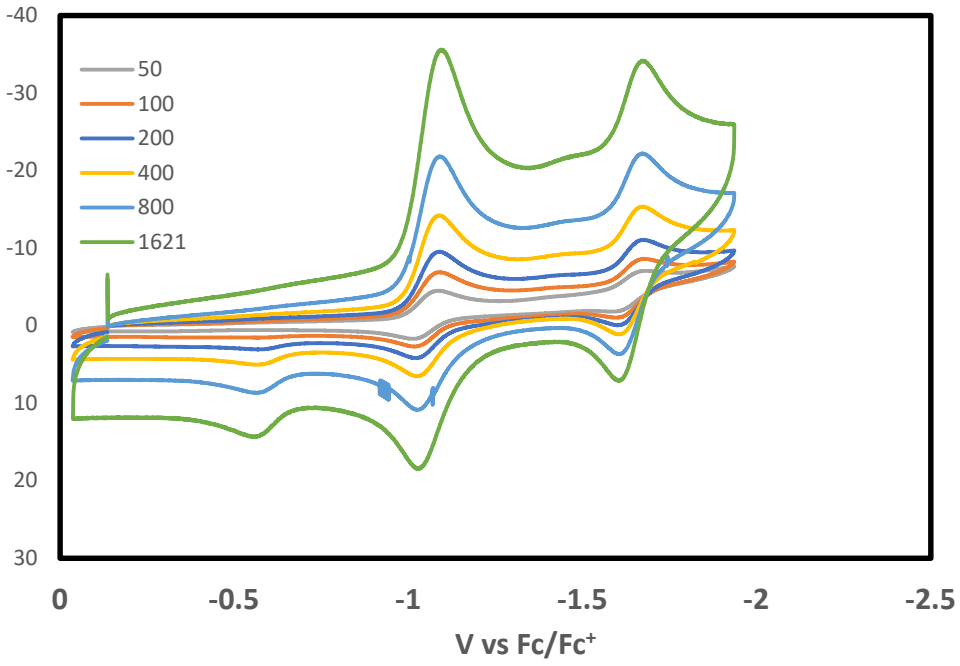

Figure 87. Scan rate dependence of Ni-ATSMpy double arm.

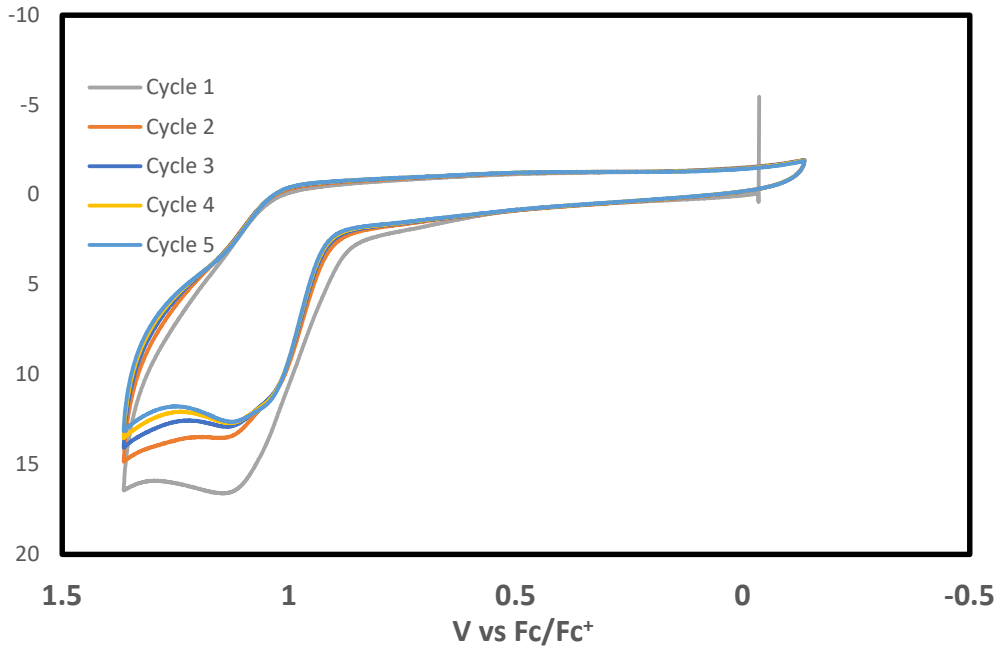

Figure 88. Five cycle oxidation of Ni-ATSMpy double arm.

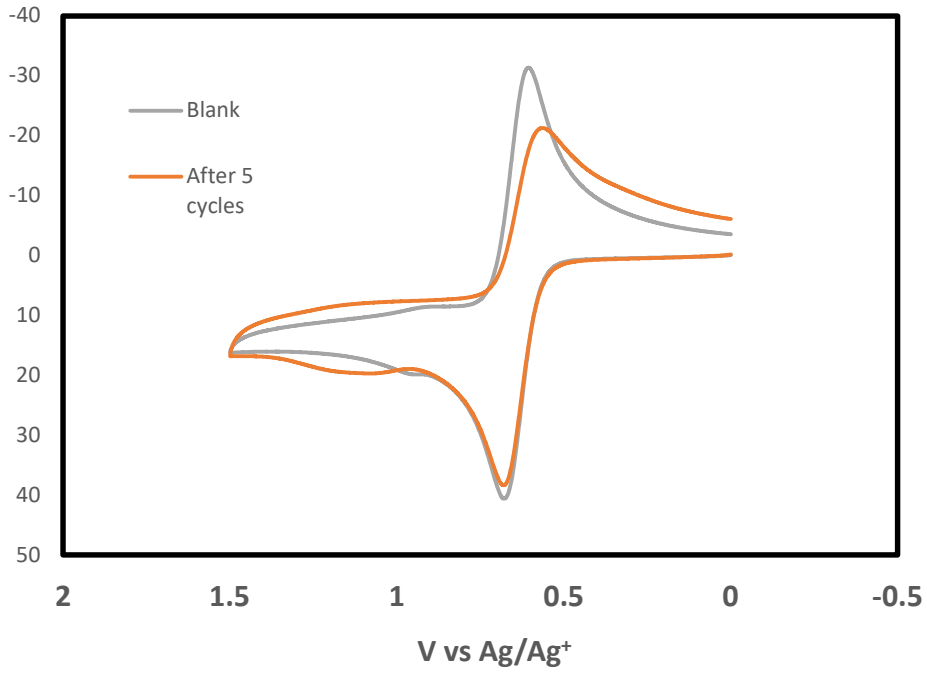

Figure 89. Ferrocene before and after on GC for Ni-ATSMpy double arm on GC.

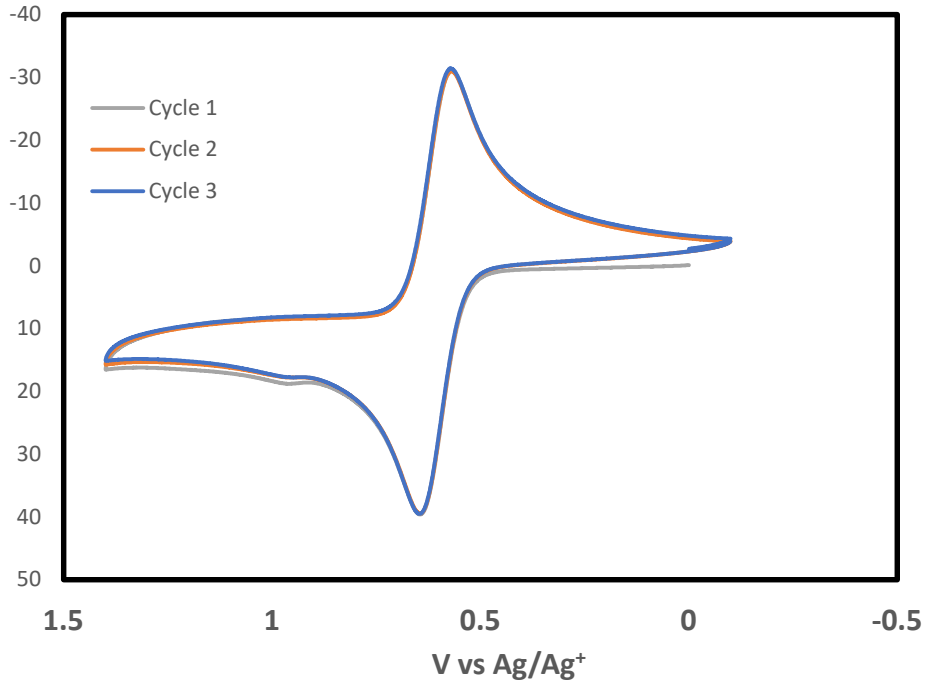

Figure 90. Three cycle oxidation after five cycle oxidation of Ni-ATSMpy double arm on GC.

vii. C7: Zn-ATSMpy Double Arm

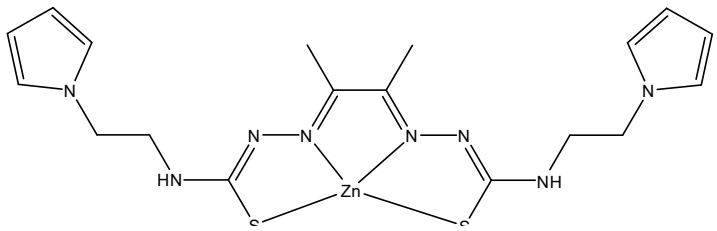

Figure 91. Zn-ATSMpy double arm (0.1mM) 0.1M $NaClO_4/KClO_4$ in acetonitrile molecular structure.

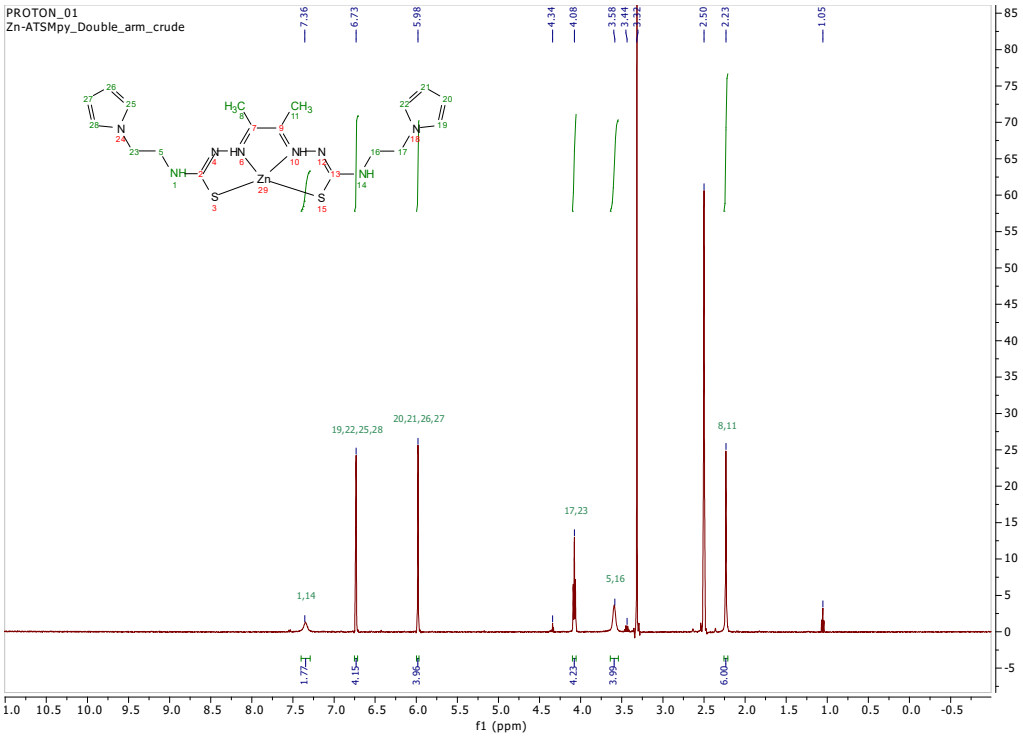

Figure 92. Zn-ATSMpy double arm NMR spectrum.

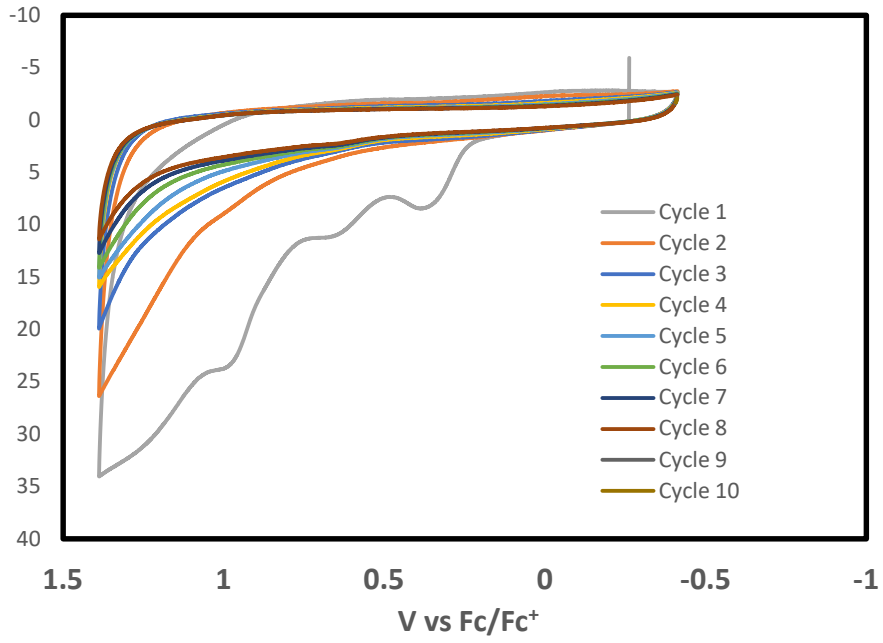

Figure 93. 10 cycle oxidation of Zn-ATSMpy double arm on GC.

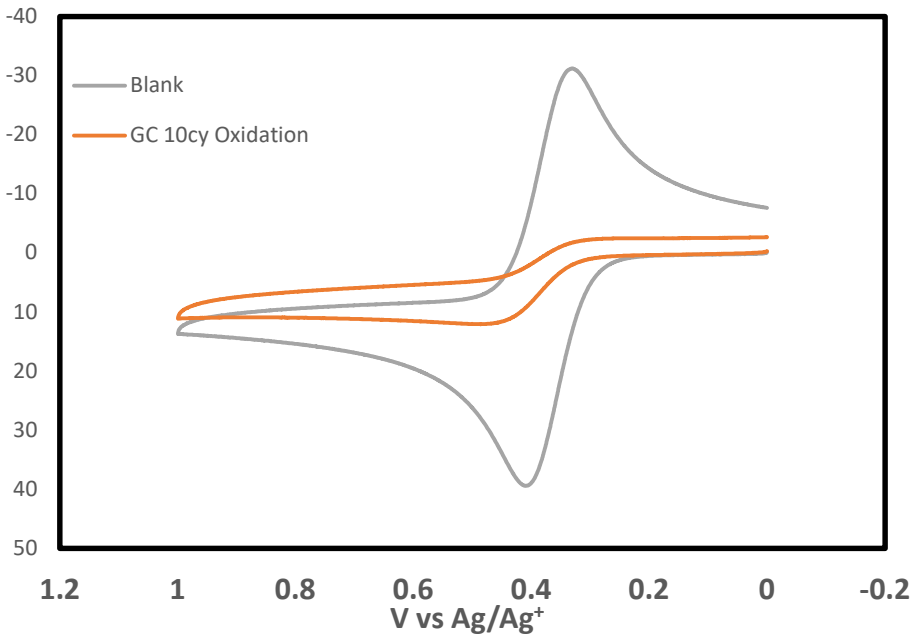

Figure 94. Ferrocene comparison Zn-ATSMpy double arm on GC.

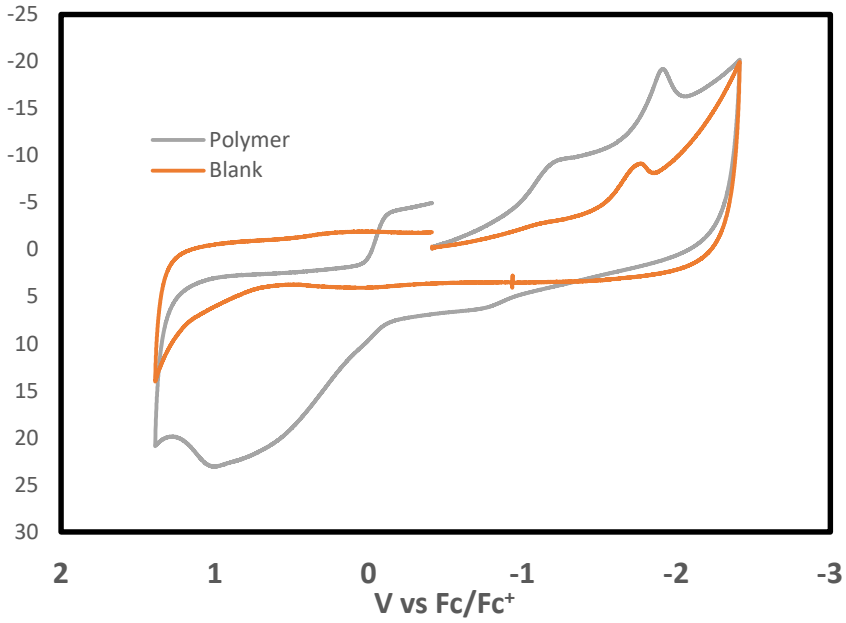

Figure 95. Zn-ATSMpy double arm after polymerization.

viii. C8: ATSM-BTP4A Single Arm

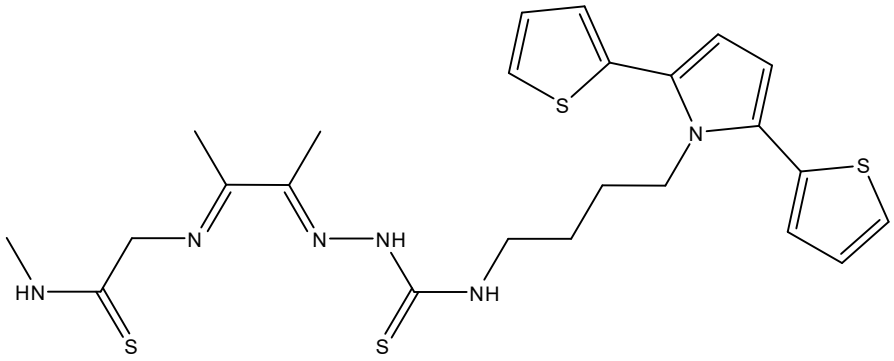

Figure 96. ATSM-BTP4A 0.3mM 0.1M TBAF molecular structure.

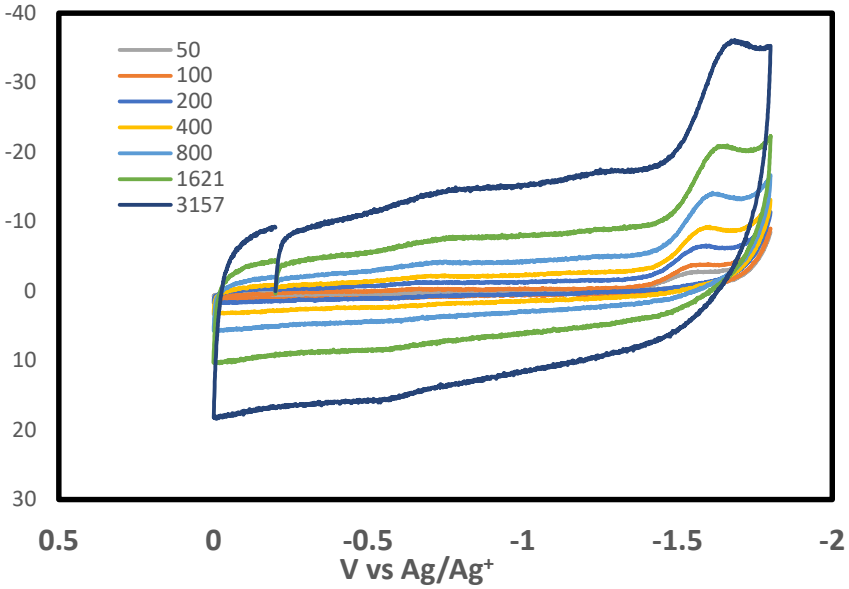

Figure 97. Scan rate dependance of ATSM-BTP4A.

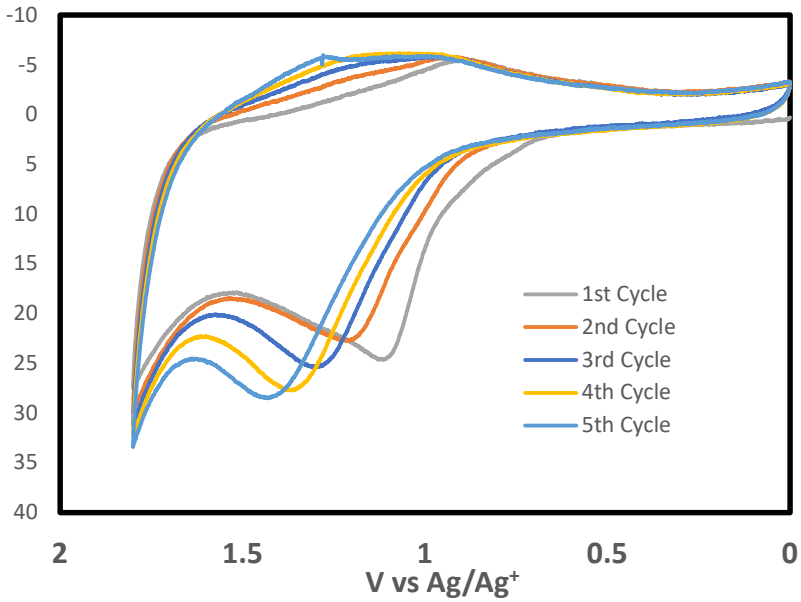

Figure 98. Five cycle polymerization of ATSM-BTP4A on GC.

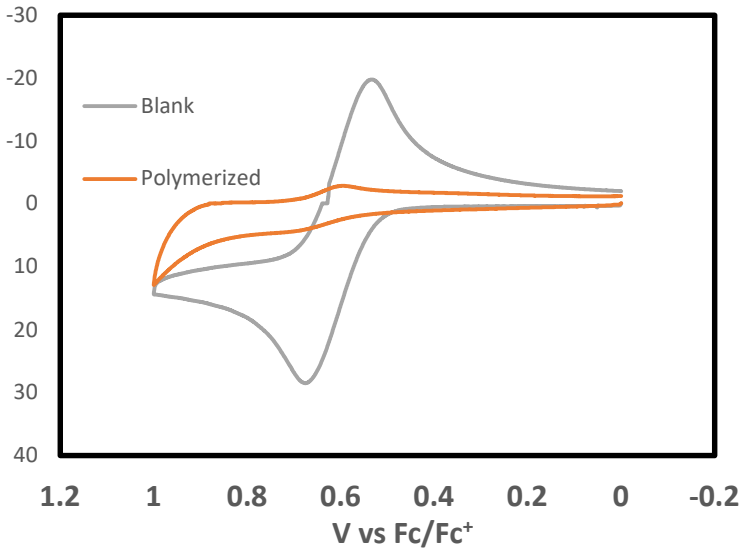

Figure 99. Ferrocene comparison to ATSM-BTP4A on GC.

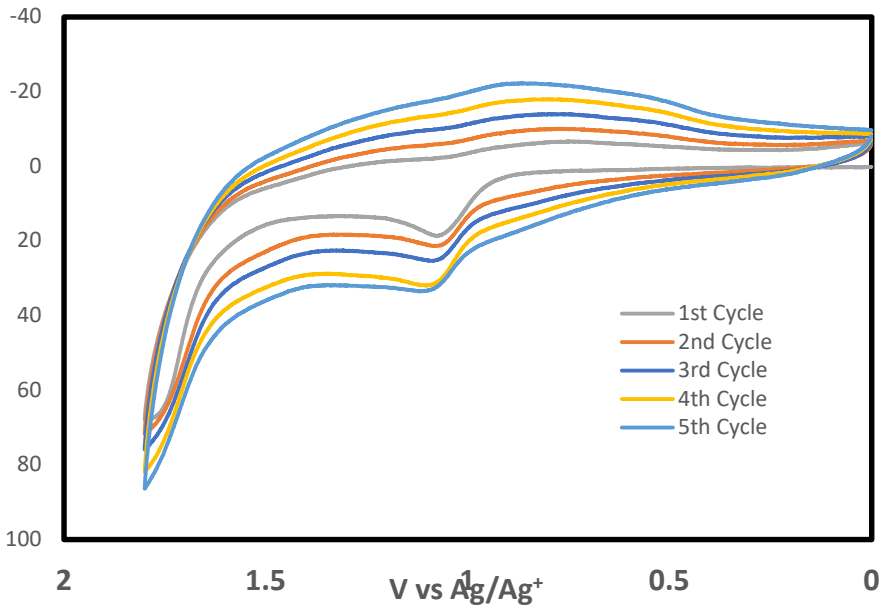

Figure 100. Five cycle co-polymerization with ATSM-BTP4A(0.3mM) and EDOT(0.15mmol) on GC.

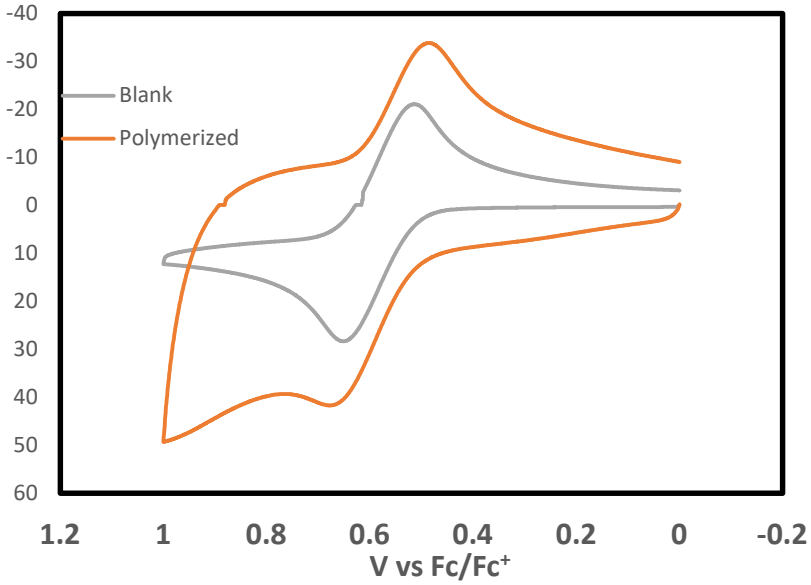

Figure 101. Ferrocene co-polymerization comparison for ATSM-BTP4A+EDOT.

ix. C9: Ni-ATSM-BTP4A Double Arm

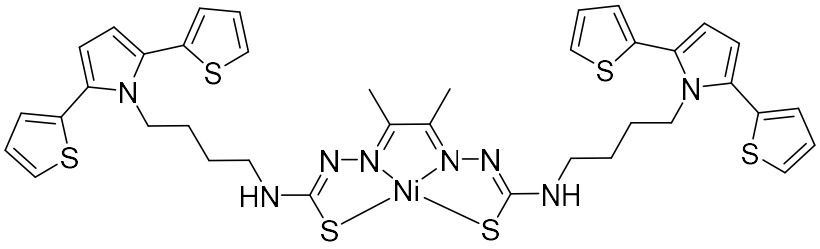

Figure 102. Ni-ATSM BTP4A double arm (0.1mM) 0.1M $NaClO_4/KClO_4$ in acetonitrile molecular structure.

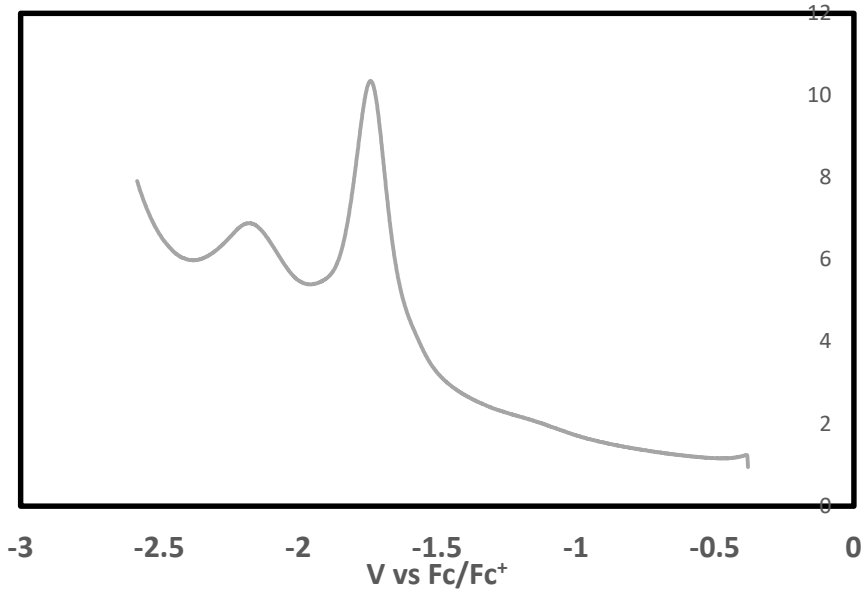

Figure 103. Square wave of Ni-ATSM-BTP4A-double arm.

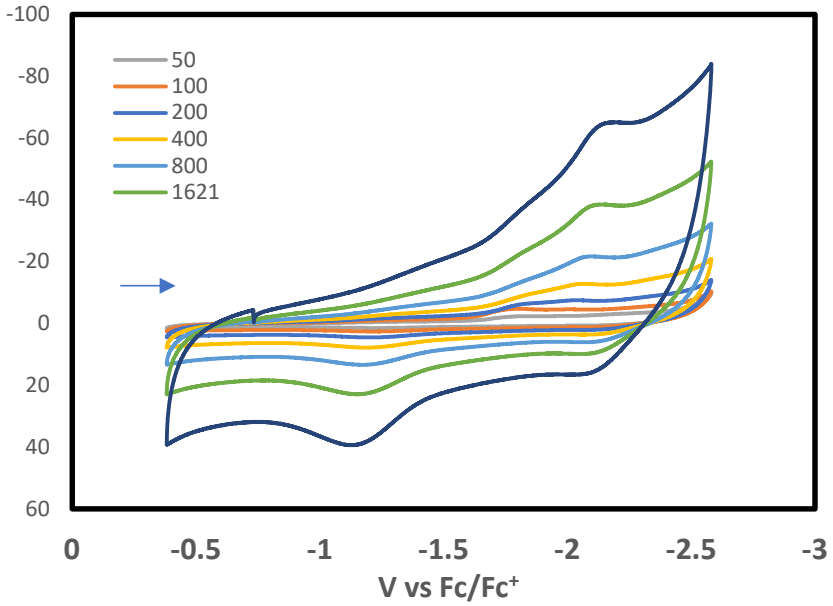

Figure 104. Scan rate dependence of Ni-ATSM-BTP4A double arm.

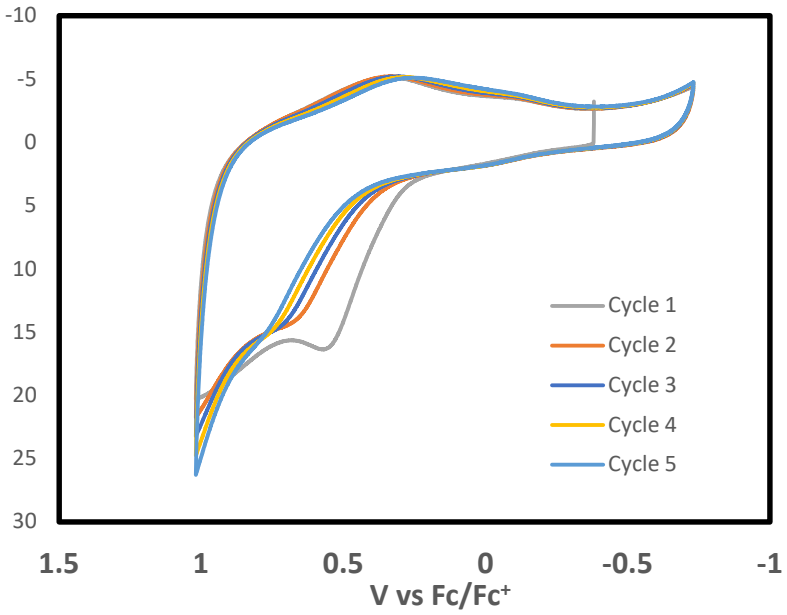

Figure 105. Five cycle oxidation of Ni-ATSM-BTP4A double arm on GC.

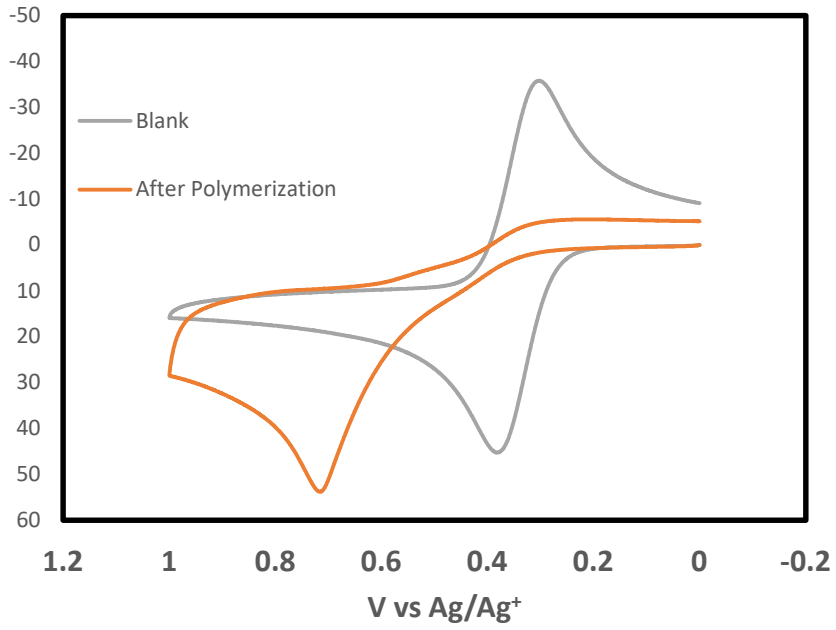

Figure 106. Ferrocene comparison blank and polymer Ni-ATSM-BTP4A double arm on GC.

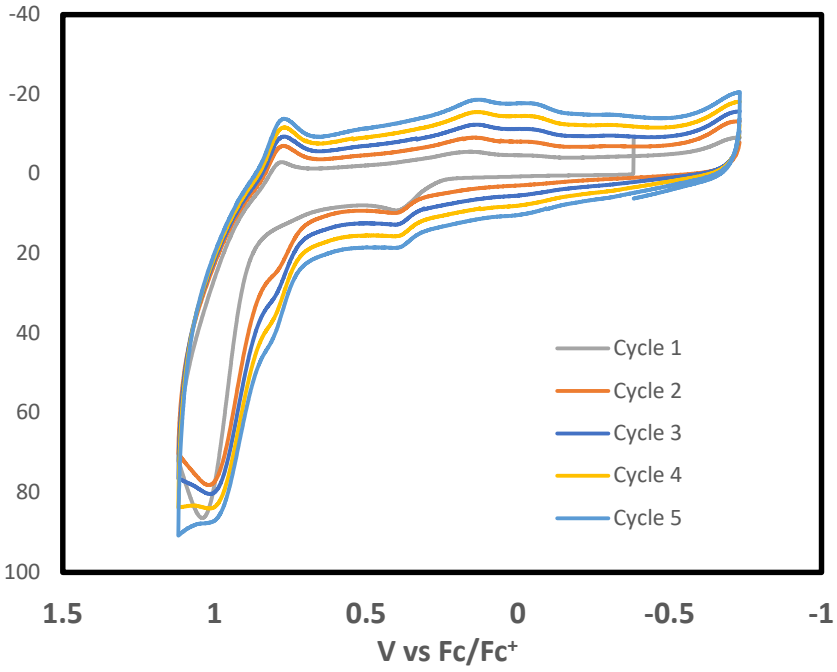

Figure 107. Five cycle polymerization for EDOT+Ni-ATSM-BTP4A double arm on GC.

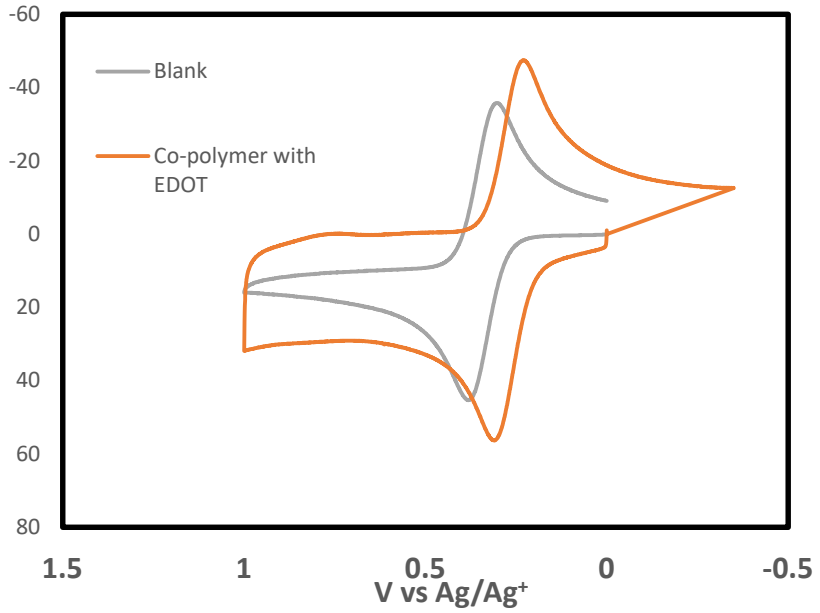

Figure 108. Ferrocene comparison blank and EDOT copolymer on GC.

x. C10: ATSM-BTP4A Double Arm

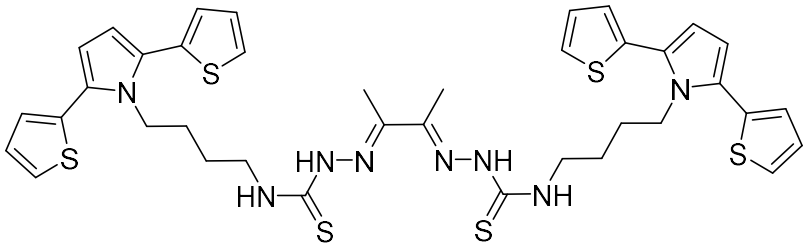

Figure 109. ATSM-BTP4A double arm (0.1mM) solution 0.1M TBAHFP electrolyte molecular structure.

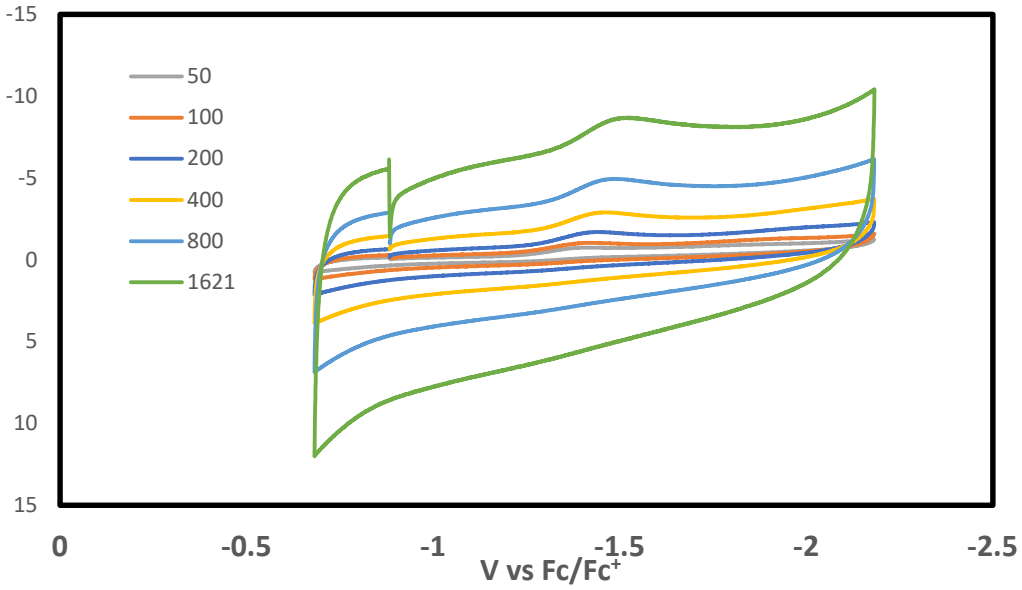

Figure 110. Scan rate dependance of ATSM-BTP4A double arm.

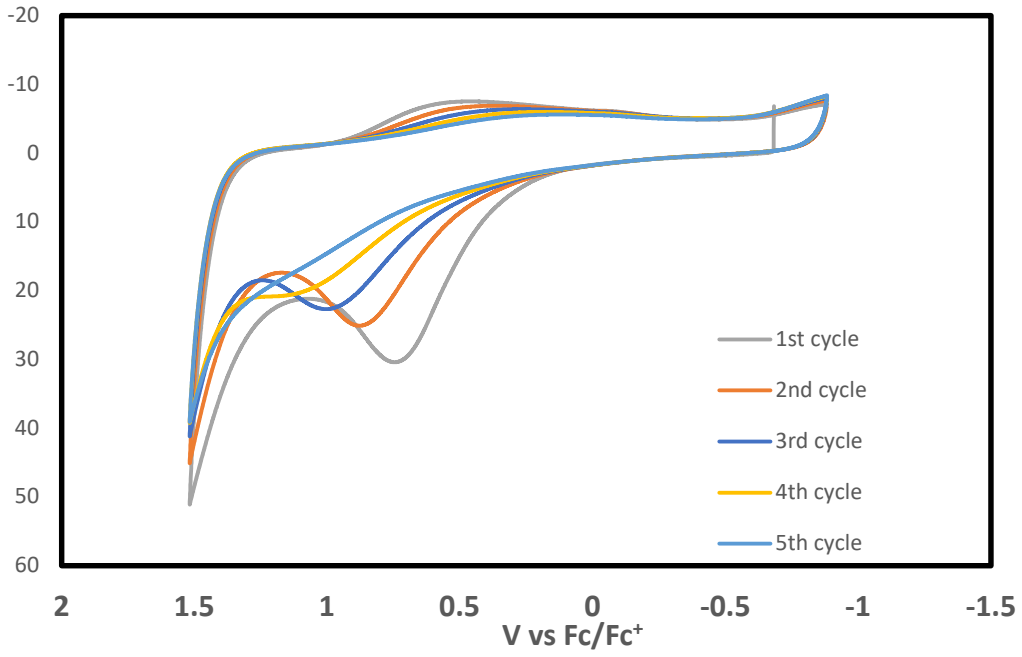

Figure 111. Five cycle polymerization of ATSM-BTP4A double arm in high oxidation potential using GC electrode.

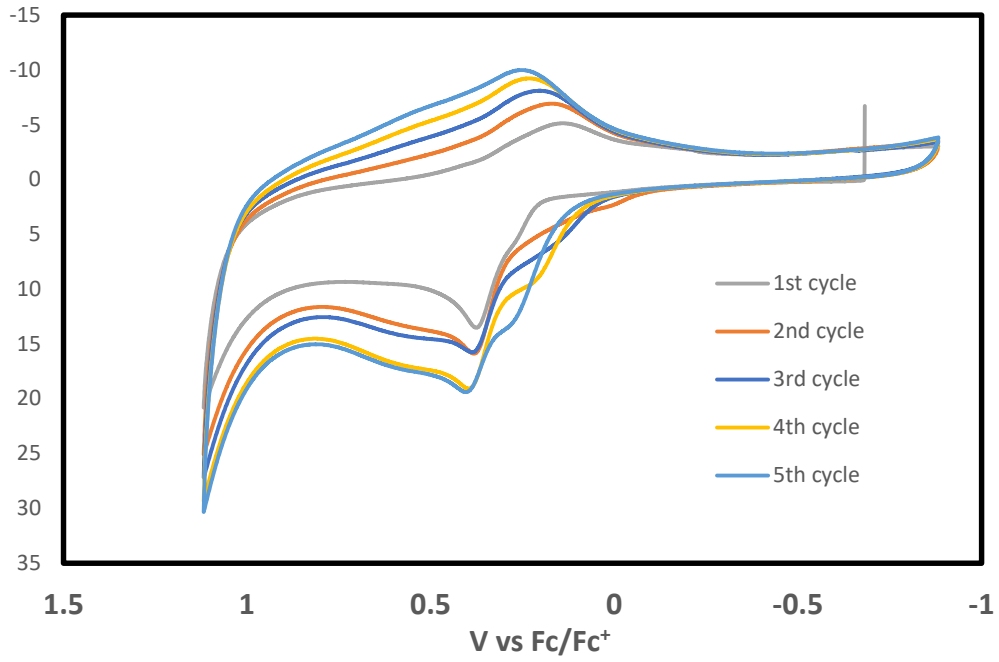

Figure 112. ATSM-BTP4A double arm five cycle OXD low potential on GC.

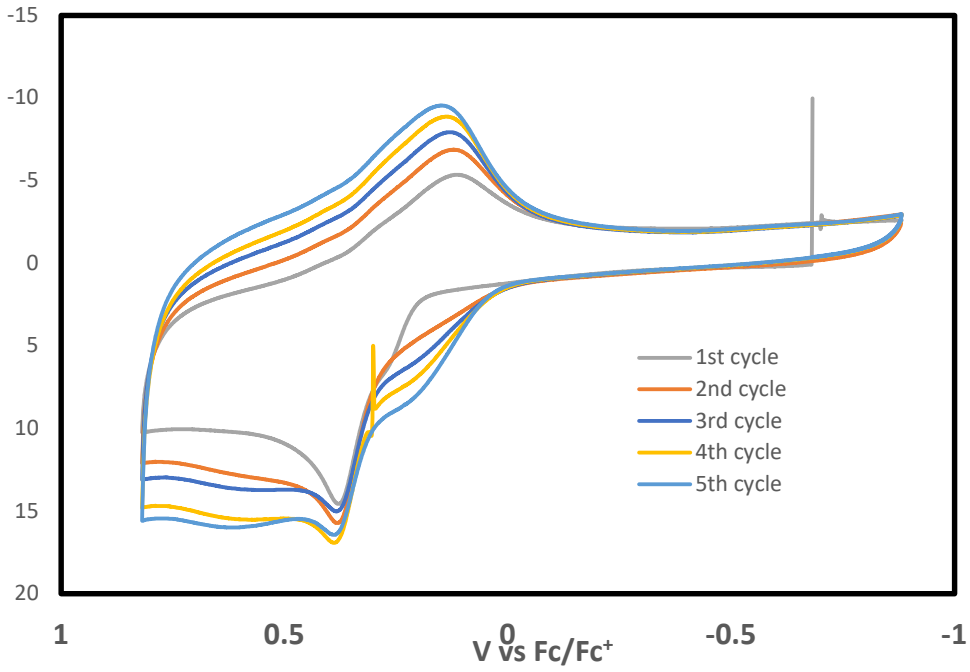

Figure 113. ATSM-BTP4A Double arm five cycle OXD very low potential on GC.

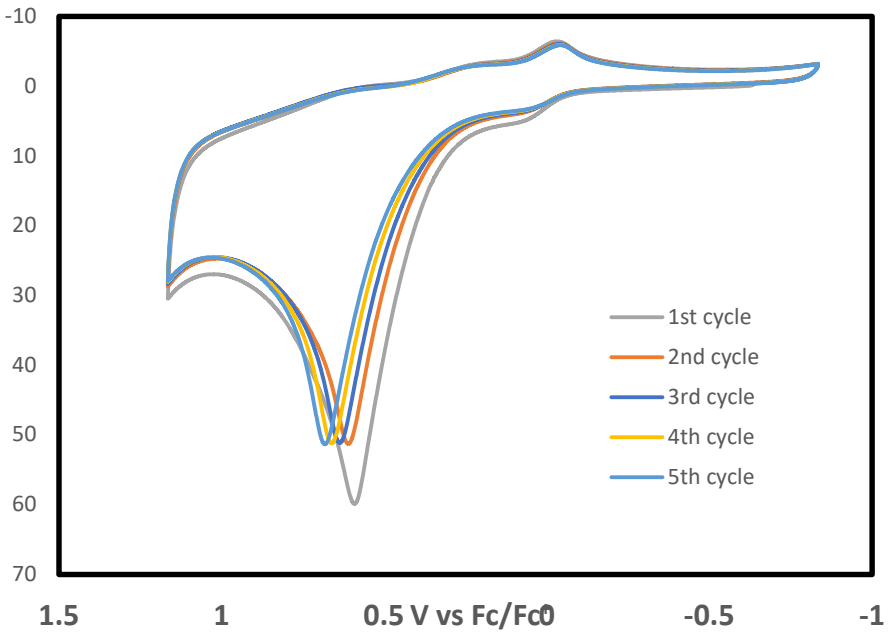

Figure 114. Five cycle oxidation of GC polymer at low potential.

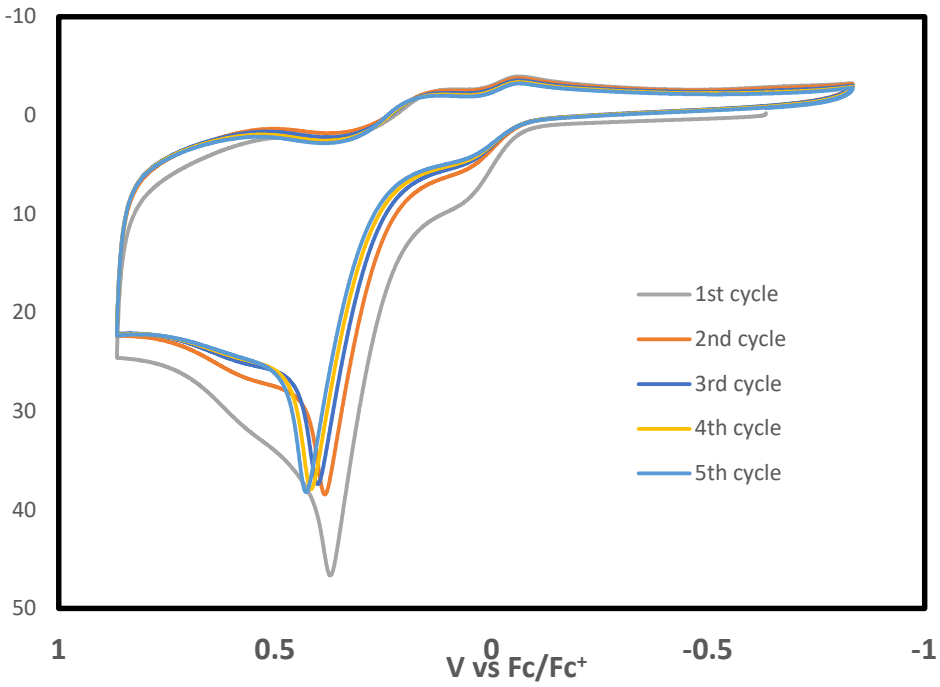

Figure 115. Five cycle oxidation of GC polymer at very low potential.

xi. C11: Ni-ATSM-BTP4A Single Arm

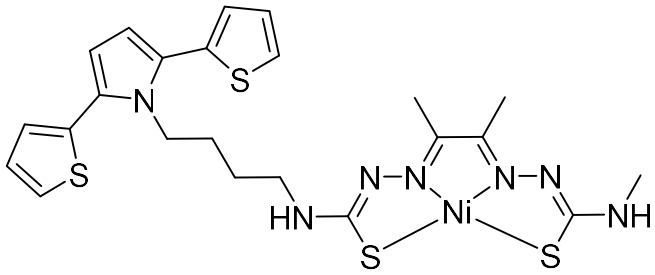

Figure 116. Ni-ATSM-BTPBA (0.3mMol) 0.1M TBAF in acetonitrile molecular structure.

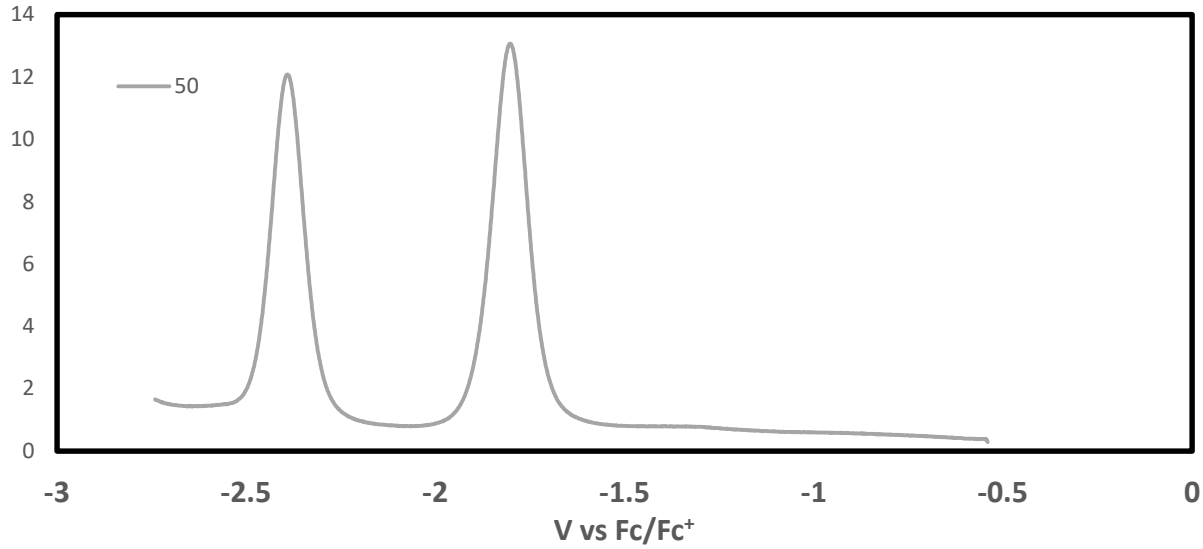

Figure 117. Square wave voltammetry for Ni-ATSM-BTPA.

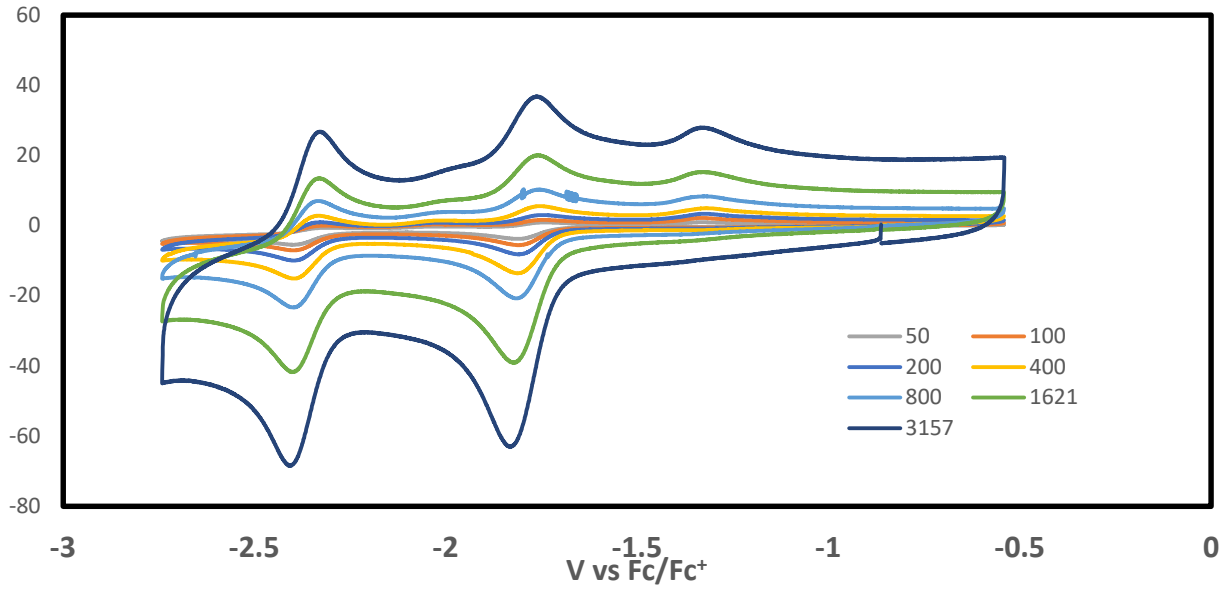

Figure 118. Ni-ATSM-BTPBA full reduction scan rate dependance.

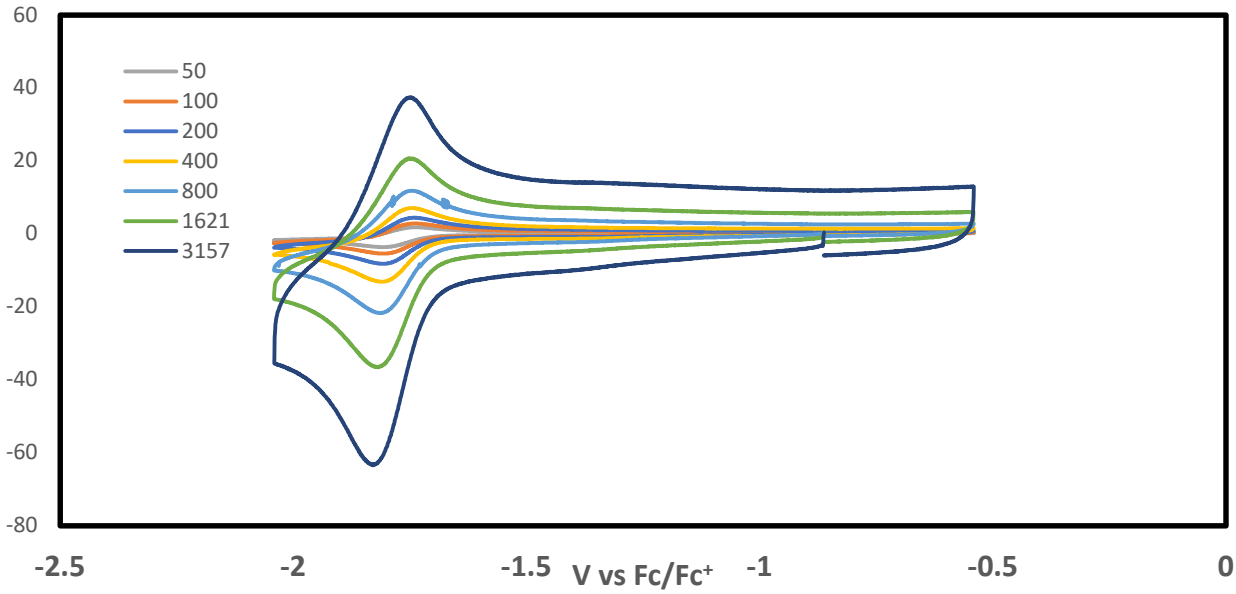

Figure 119. Ni-ATSM-BTPBA single red scan rate dependance.

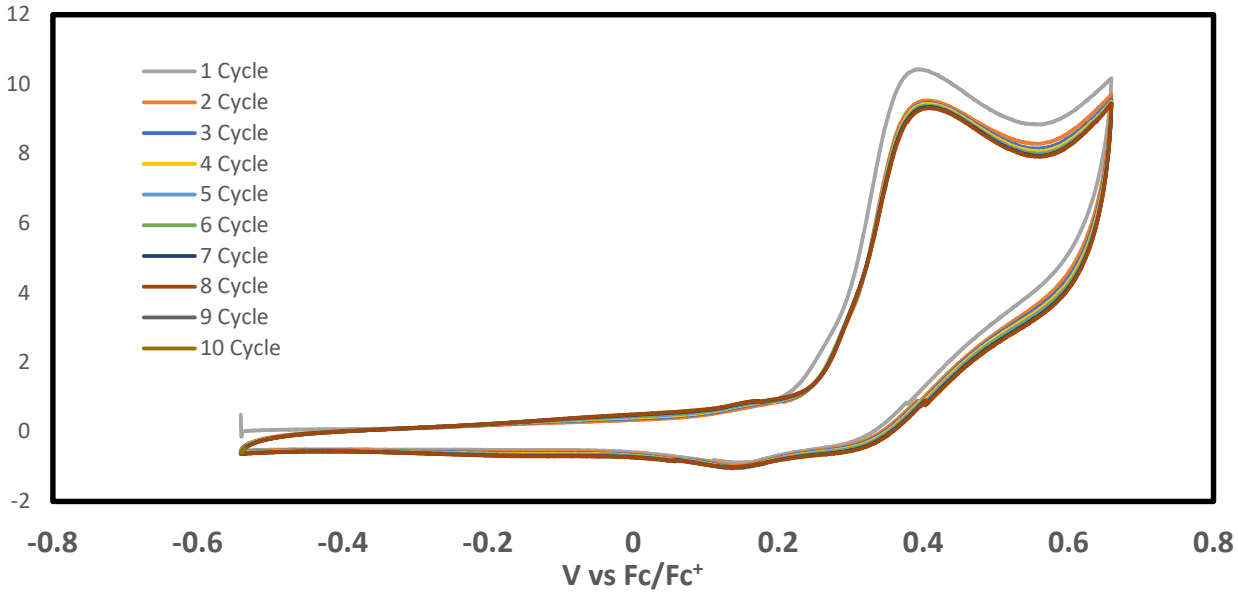

Figure 120. 10 Cycle oxidation of Ni-ATSM-BTPA.

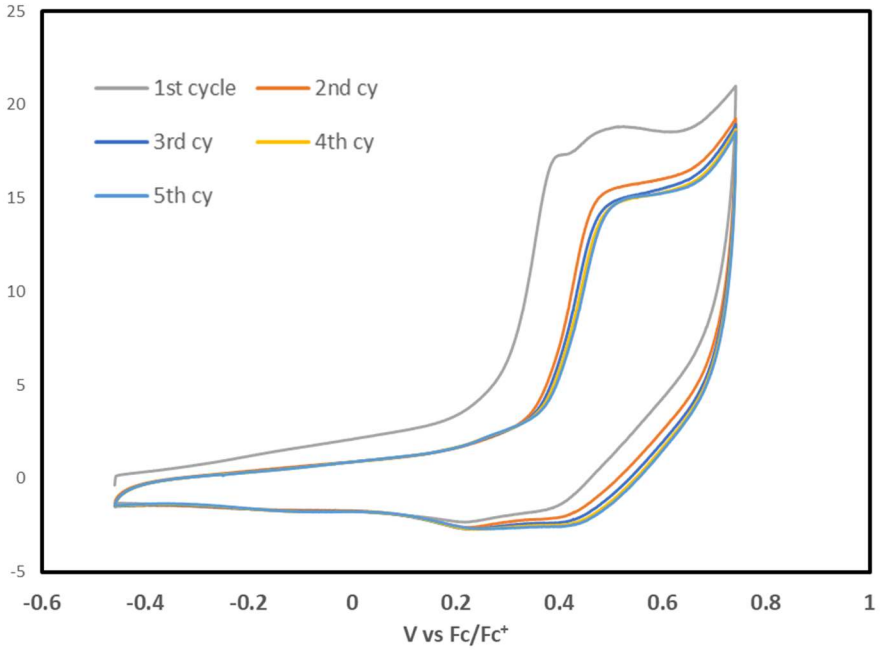

Figure 121. Five cycle oxidation on GC for Ni-ATSM-BTPA.

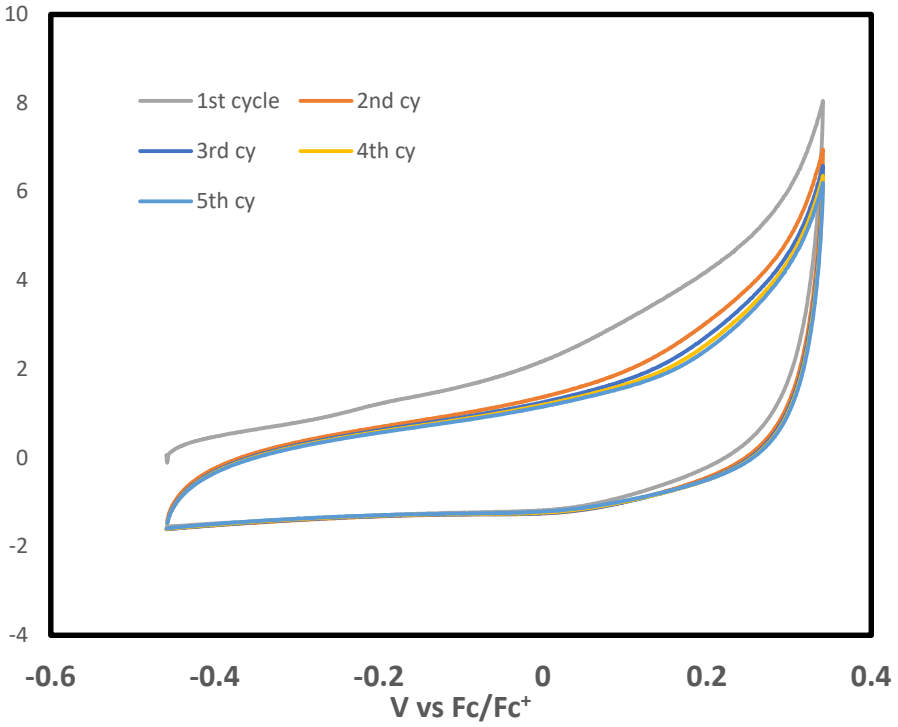

Figure 122. Five cycle oxidation in low range on GC for Ni-ATSM-BTPA.

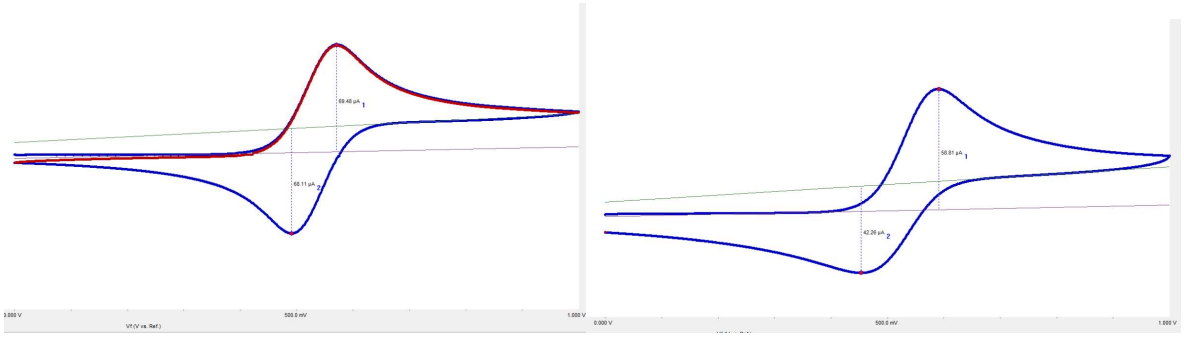

Figure 123. Current decrease in ferrocene(0.1M)=69uA=58uA=11uA.

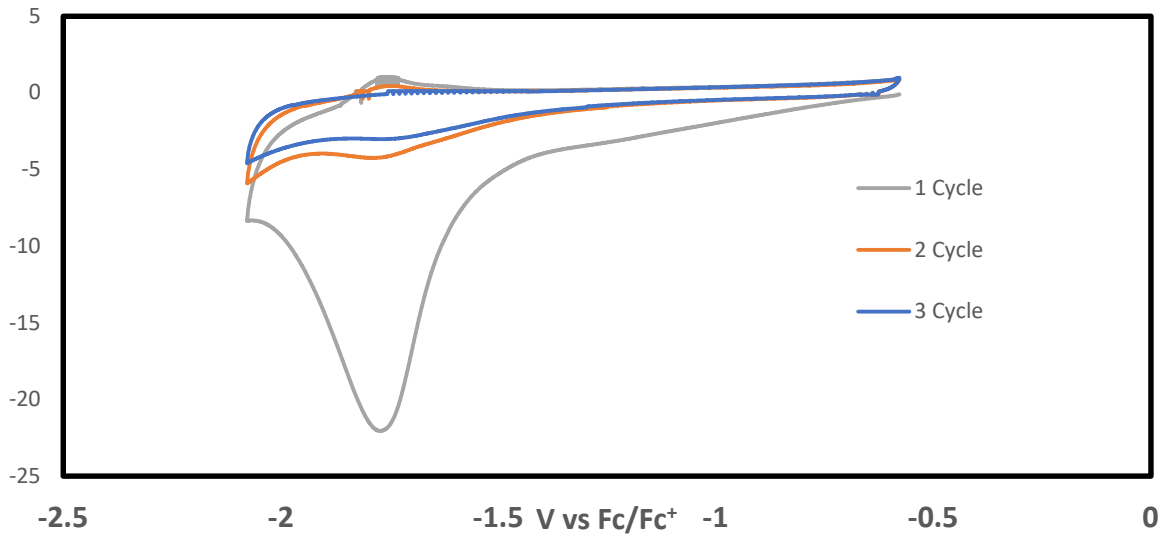

Figure 124. Three cycle reduction of polymer film in blank Ni-ATSM-BTPA.

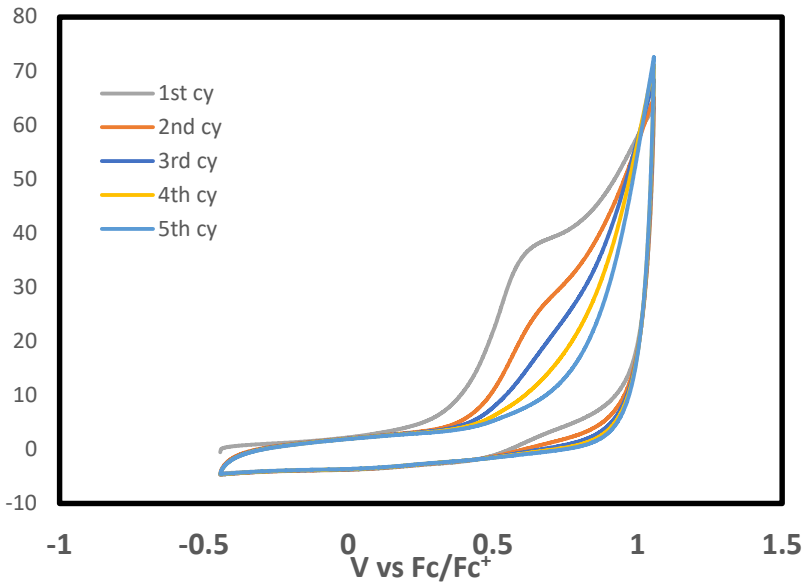

Figure 125. Five cycle oxidation on Pt electrode Ni-ATSM-BTPA.

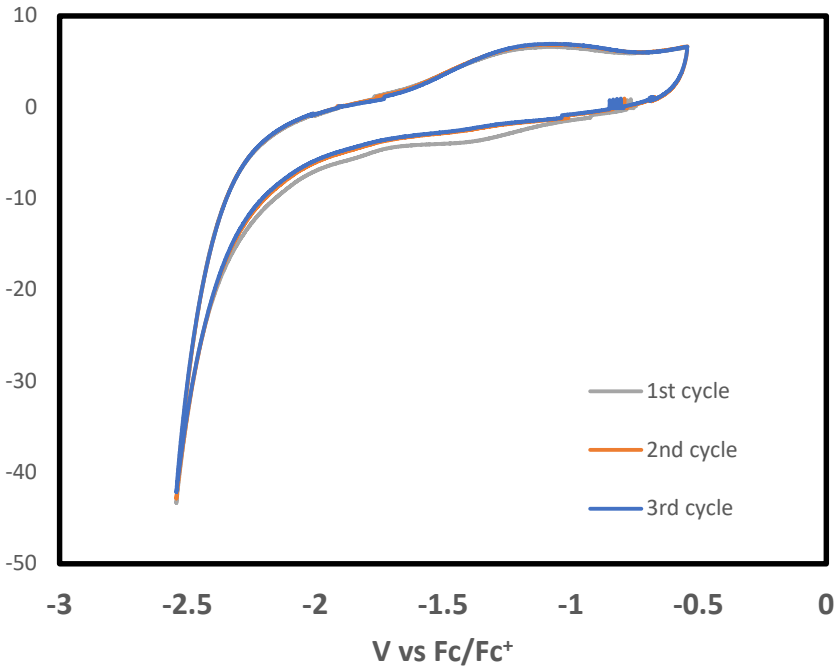

Figure 126. Three cycle reduction of polymer on Pt electrode Ni-ATSM-BTPA.

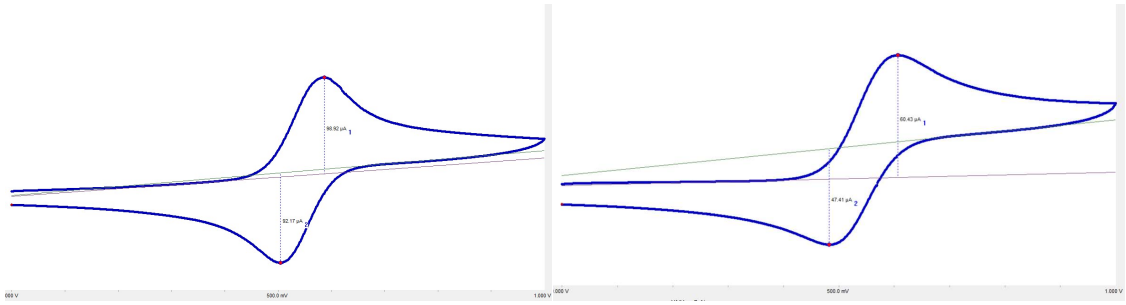

Figure 127. Current decrease in ferrocene(0.1M)=99uA=60uA=39uA.

xii. C12: Ni-ATSM/DMEDA

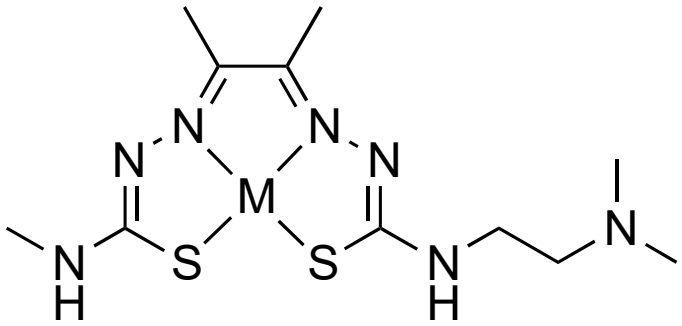

Figure 128. Ni-ATSM/DMEDA molecular structure M=Ni.

Extensive characterization of Ni-ATSM/DMEDA can be found in reference [67].

xiii. C13: Ni-ATSM Pyrene

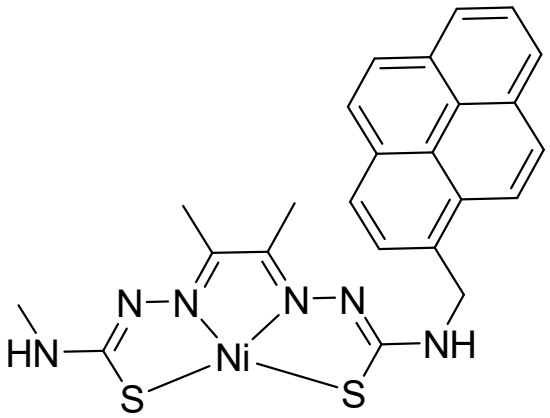

Figure 129. Ni-ATSM pyrene molecular structure.

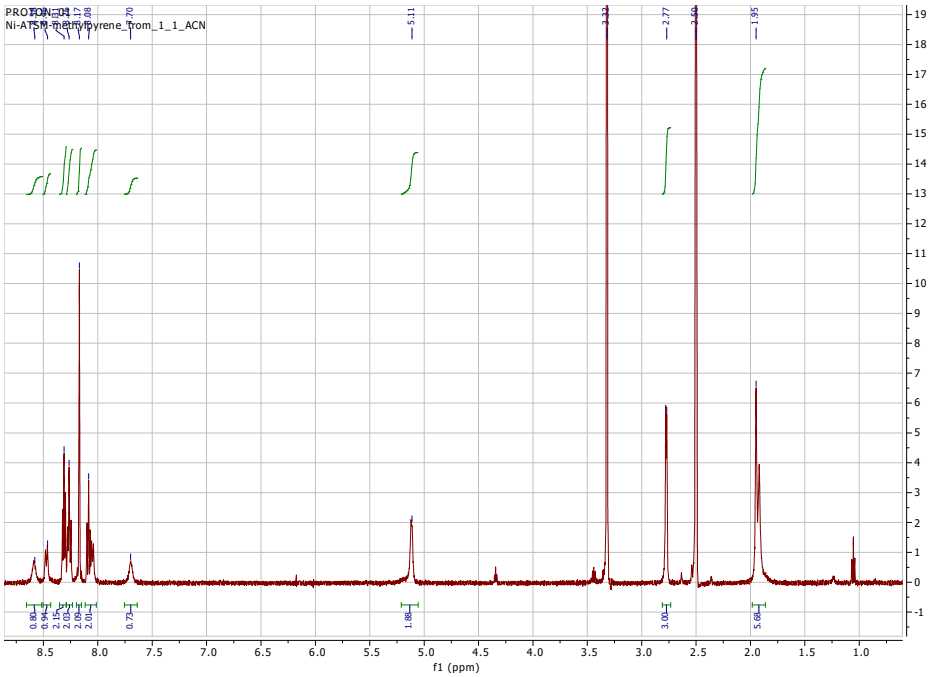

Figure 130. NMR spectrum for Ni-ATSM pyrene.

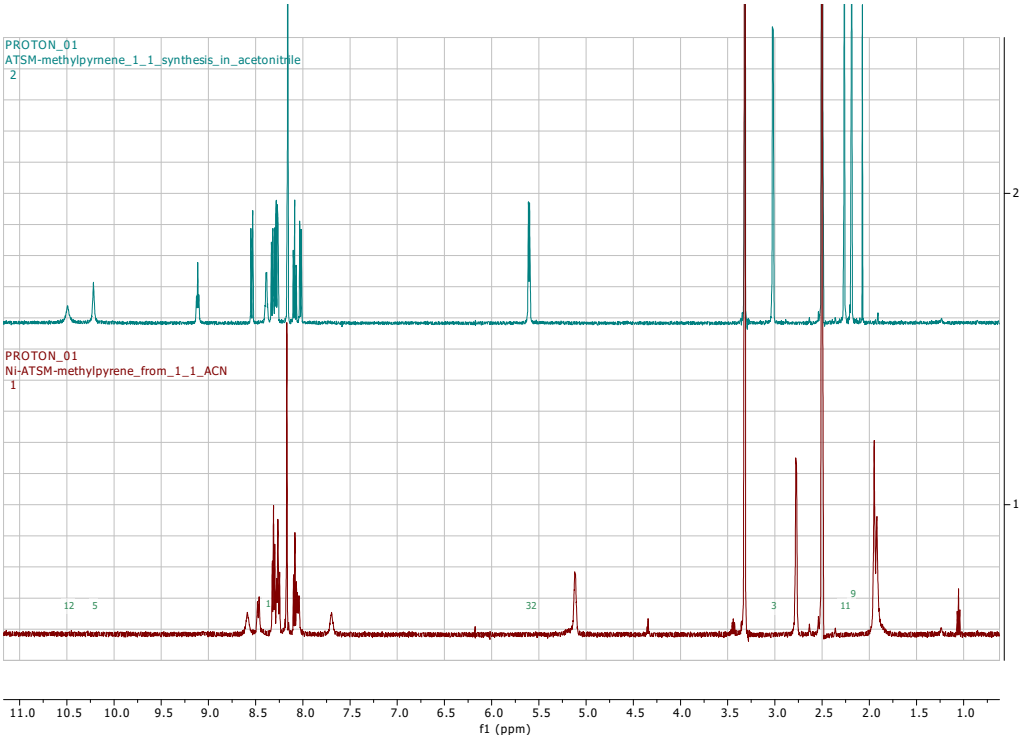

Figure 131. ATSM pyrene (top) and Ni-ATSM pyrene (bottom) NMR spectra.

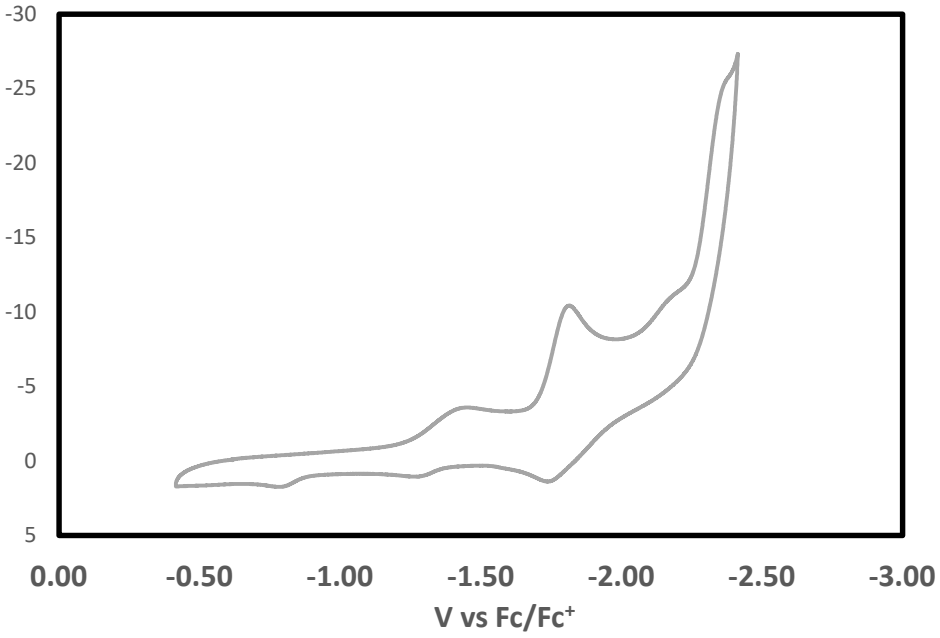

Figure 132. Full reduction of Ni-ATSM pyrene.

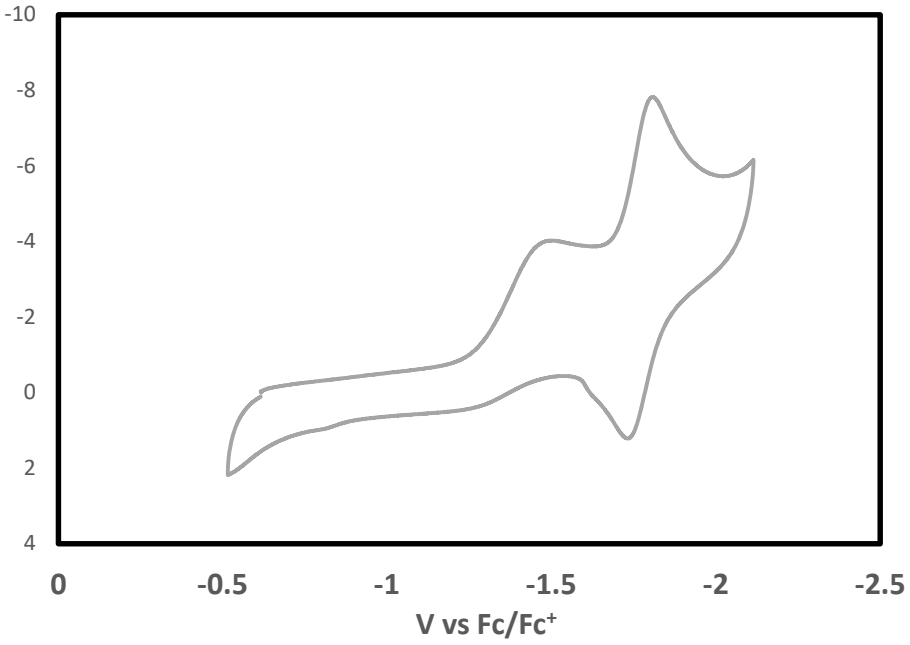

Figure 133. Single reduction of Ni-ATSM pyrene.

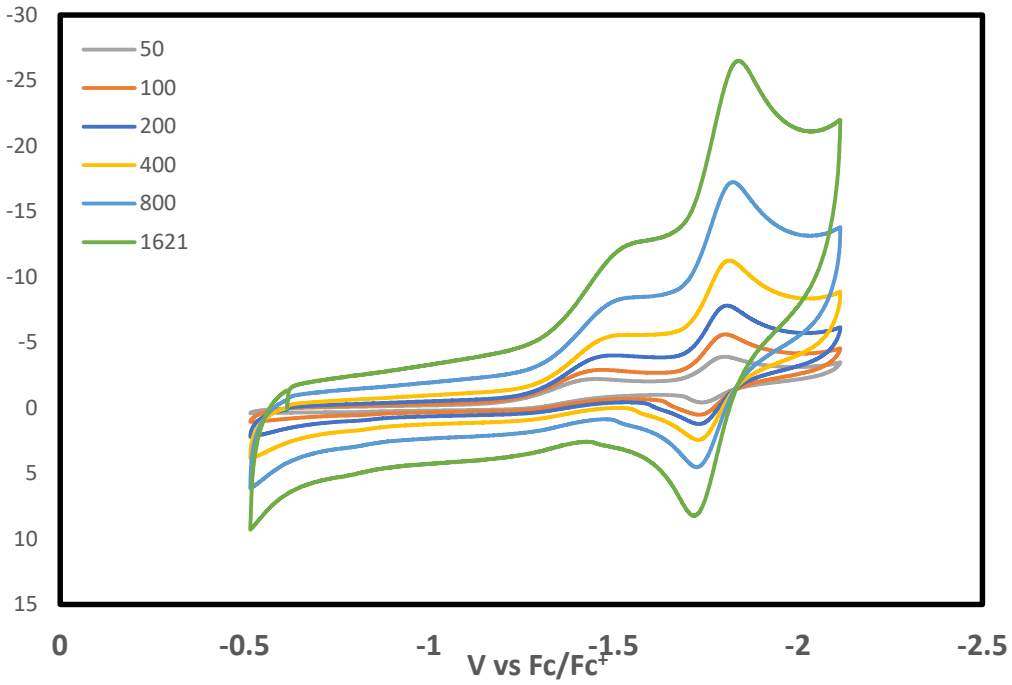

Figure 134. Scan rate dependance of first event for Ni-ATSM pyrene.

xiv. C14: Cu-ATSM/DMEDA

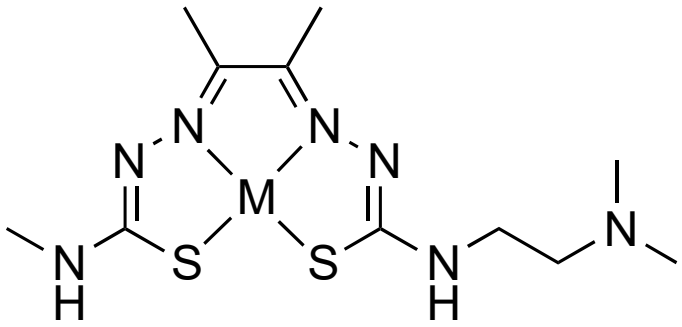

Figure 135. Cu-ATSM/DMEDA molecular structure M=Cu.

Extensive characterization of Cu-ATSM/DMEDA can be found in reference [67].

xv. C15: Ni-ATSM

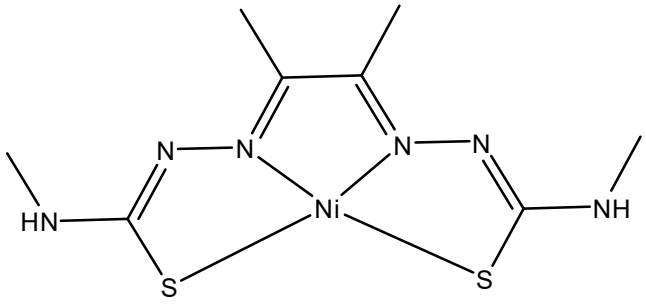

Figure 136. Ni-ATSM molecular structure.

Extensive characterization of Ni-ATSM can be found in reference [22].

B. Appendix B: Pencil Electrode Previous Study

Electrochemical Characterization of various graphite content (or hardness) pencils was carried out in a three-electrode electrochemical cell. Pencils ranging from 4H to 12B on the hardness scale were characterized; however, due to the properties and ease of obtaining each pencil, the HB, 4B and 8B pencils were chosen for discussion. Figure 137a shows the linear sweep voltammetry plots for HB, 4B and 8B pencils compared with that of a standard GCE. The plot reveals that the 8B pencil has an over potential that is similar to that of the GCE. When observing the current density at -0.9V of applied potential, the current densities do differ slightly, with the GCE at -4 mA/cm^2, the 8B pencil at -11mA/cm^2, the 4B pencil at -17 mA/cm^2, and the HB pencil at -28 mA/cm^2. While these differences in current density at higher applied potentials can be seen, most catalysts will work in the 0 to -0.5V range. Within this range, it can be seen that there is little variation in the current densities of any of the pencils when compared with glassy carbon.

From that it was expected that the impedance response of the 8B pencil would be more like that of the GCE. However, the experimental EIS in Figure 137b shows that the 8B pencil has the minimum resistance. Based on the LSV results, there is confidence that any of the pencil grades can be utilized as carbon support. However, the HB pencil was utilized for further studies due to its wide availability and similar electrochemical behavior to that of GCE in 0 to -0.5V. This pencil also had the lowest carbon content of the three pencils tested. Due to its high filler material content, this pencil was chosen as the best candidate for producing a higher surface area carbon support material through simple acetone etching [78].

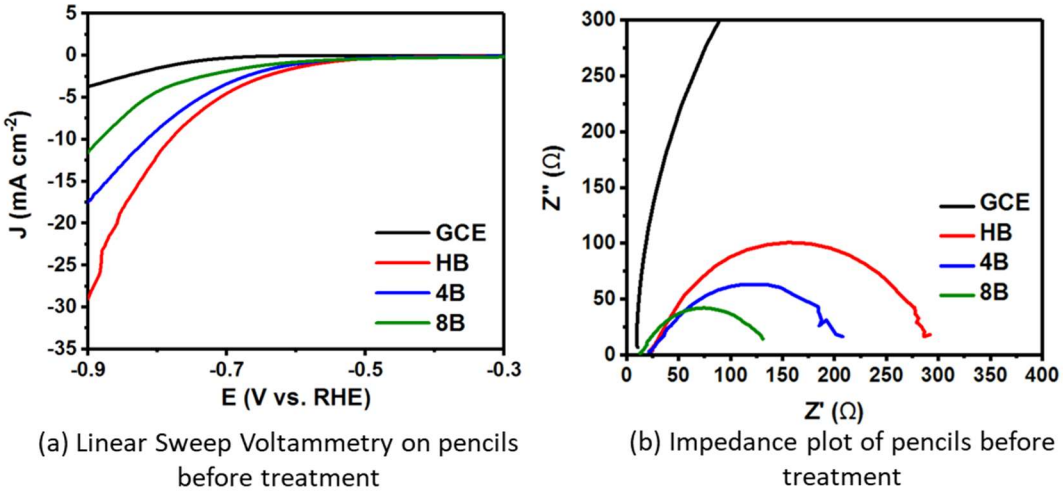

(a) Linear Sweep Voltammetry on pencils before treatment

(b) Impedance plot of pencils before treatment

Figure 137. LSV and Impedance Plots for HB, 4B, and 8B Pencils [78].

C. Appendix C: C15 (Ni-ATSM) Previous Study

In this study, a series of crystalline nickel (II) complexes (1−3) based on inexpensive bis(thiomesicarbazone) ligands diacetylbis(4-methyl-3-thiomesicarbazone) (H_2ATSM aka Ni-ATSM aka C15), diacetylbis(4,4-dimethyl-3-thiomesicarbazone) (H_2ATSDM), and diacetylbis[4-(2,2,2-trifluoroethyl)-3-thiomesicarbazone] (H_2ATSM-F_6) were synthesized and characterized and then films of the complexes were deposited onto glassy carbon (GC) electrodes to modify them. The modified electrodes were evaluated as potential hydrogen evolution reaction (HER) catalysts. HER studies in 0.5 M aqueous H_2SO_4 (10 mA/cm^2) revealed dramatic shifts in the overpotential from 0.740 to 0.450 V after extended cycling. LSV plots are shown in Figure 138 A-C and Tafel plots are shown in Figure 138 D-F for the three GCs [22].

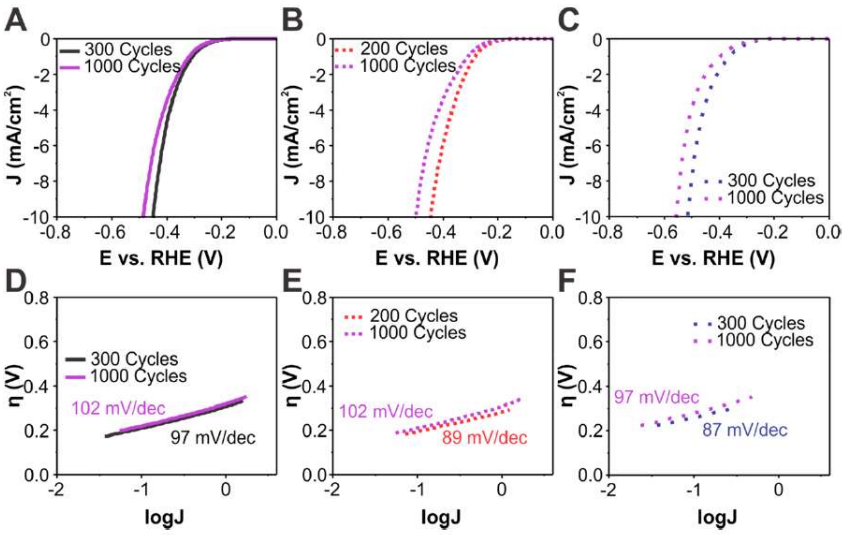

Figure 138. Effects of reductive cycling from 0 to −0.8 V vs RHE at 50 mV s−1 on the performance of the three modified electrodes past peak activity. (A) polarization curves for GC-1 (B) polarization curves for GC-2 (C) polarization curves for GC-3 (D) Tafel slopes for GC-1 at 300 and 1000 cycles. (E) Tafel slopes for GC-2 at 200 and 1000 cycles. (F) Tafel slopes for GC-3 at 300 and 1000 cycles [22].